Cold Atoms in Optical Lattices

by Robin George Scott, MSci
Thesis submitted to the University of Nottingham
for the degree of Doctor of Philosophy
March 2003

Contents

Abstract

This thesis describes the behaviour of cold atoms in optical lattices. In particular, it explores how transport through the energy bands of the optical lattice can be used to study quantum chaos and Bose-Einstein condensation.

Firstly, this study examines the dynamics of ultra-cold sodium atoms in a one-dimensional optical lattice and a three-dimensional harmonic trap, using both semi-classical and quantum-mechanical analyses. The atoms show mixed stable-chaotic classical dynamics, which originate from the intrinsically quantum-mechanical nature of the energy band. The quantised energy levels exhibit Gutzwiller fluctuations, and the wavefunctions are scarred by an unstable periodic orbit. Distinct types of wavefunction are identified and related directly to particular parts of the classical phase space via a Wigner function analysis.

Secondly, this report studies the dynamics of a rubidium Bose-Einstein condensate in a one-dimensional optical lattice and three-dimensional harmonic trap. The condensates are set in motion by displacing the trap and initially follow simple semi-classical paths, shaped by the lowest energy band. Above a critical displacement, the condensate undergoes Bragg reflection, and performs Bloch oscillations. After multiple Bragg reflections, solitons and vortices form which damp the centre-of-mass motion.

Finally, the dynamics of Bose-Einstein condensates in optical lattices are investigated for different parameter regimes, as realised in recent experiments. The results reveal how the experiments can be understood, and identify regimes in which vortices trigger explosive expansion of the condensate.

Acknowledgments

I would like to express my gratitude to the following people:

Dr. T.M. Fromhold for supervising my PhD project, and for his helpful suggestions and insights.

Dr. S. Bujkiewicz for working with me on both the quantum chaos and Bose-Einstein condensation problems.

Dr. P.B. Wilkinson for his advice on quantum chaos and computing.

Dr. M. Leadbeater for introducing me to Bose-Einstein condensation.

Dr. A.M. Martin for discussions about Bose-Einstein condensation.

Dr. O. Morsch and Dr. E. Arimondo for discussions about their experiments on Bose-Einstein condensates.

Chapter 1

Cold atom dynamics and band theory

1.1 Introduction

Optical lattices are standing light waves formed by counter-propagating laser beams [1, 2, 3]. They are used in conjunction with trapped atoms, which experience the standing wave as a spatially periodic potential. The resulting dynamics are analogous to that of an electron moving in the periodic potential of a crystal lattice, and so can be understood using tools borrowed from solid state physics. As a result, optical lattices link atomic physics and quantum optics with the seemingly separate topic of solid state physics.

In many ways, atom dynamics in optical lattices are experimentally more accessible than electron dynamics in crystal lattices. Firstly, the initial momentum of the atoms can be tailored to have a narrow distribution around a chosen value. Secondly, the experimentalist has precise control over the well depth, lattice period, and acceleration of the atoms. Thirdly, the optical lattice is free of defects, and so the atoms undergo no scattering due to imperfections in the crystal. Fourthly, the atoms undergo no scattering due to lattice vibrations. Fifthly, the periodic potential of an optical lattice can be switched off, allowing direct measurement of the momentum of the atoms. Finally, the atom dynamics in optical lattice occur on a time scale which is about ten orders of magnitude longer than that of electron dynamics in crystal lattices. As a result of these points, atom dynamics in optical lattices can demonstrate effects that can be detected only indirectly in crystal lattices.

When conducting an experiment on atoms in an optical lattice, the parameters must be carefully chosen if the dynamics are to faithfully mimic those of electrons in a crystal lattice. For example, the frequencies of the lasers must be detuned far from any atomic resonance. Furthermore, the temperature and the parameters of the optical lattice should be chosen such that the atomic de Broglie wavelengths extend over several lattice periods. This ensures that the atoms must be described as quantum mechanical objects, rather than as classical particles oscillating in individual potential wells.

The experimental advantages of optical lattices outlined above have encouraged physicists to make use them in a great variety of contexts including atom diffraction [4], band theory [5, 6, 7] and interferometry [8]. In this report, optical lattices are employed in the study of quantum chaos and Bose-Einstein condensation.

1.2 Band theory

Band theory describes the quantum-mechanical behaviour of a particle in a periodic potential, ignoring any interactions with other particles [9, 10]. The theory was originally devised to describe the motion of an electron in the periodic potential of a solid lattice of atoms, but it can equally be applied to an atom moving in the periodic potential of an optical lattice. The theory predicts that the particles can propagate *only if* their energies lie within set ranges called *bands.* Between the bands, there are *band gap* regions where no propagating states exist.

Consider a particle of energy E in a three-dimensional periodic potential energy field $V(\mathbf{r})$, in which $\mathbf{r}$ is the position vector. This periodic potential could be produced by either a lattice of atoms, or an optical lattice, formed by counter-propagating laser beams. In either case, the lattice is described by the *primitive lattice vectors* $\mathbf{a}_1$, $\mathbf{a}_2$ and $\mathbf{a}_3$. These vectors are used to describe the positions of every *lattice point*; that is to say the position of atoms in the case of a crystal lattice, or simply the peaks in the periodic potential in the case of an optical lattice. The primitive lattice vectors are combined in the following way to construct the vector $\mathbf{R}$ from any given lattice point to any other given lattice point:

$$\mathbf{R} = n_1\mathbf{a}_1 + n_2\mathbf{a}_2 + n_3\mathbf{a}_3, \tag{1.1}$$

where n_i is an integer. The vector $\mathbf{R}$ is known as a *lattice vector.*

Imagine the particle has energy E, and is in a particular eigenfunction $\psi(\mathbf{r})$. This eigenfunction must satisfy the following Schrödinger equation:

$$\left(-\frac{\hbar^2}{2m}\nabla^2 + V(\mathbf{r})\right)\psi(\mathbf{r}) = E\psi(\mathbf{r}). \tag{1.2}$$

Since the potential is periodic, the probability density of the particle is also expected to be periodic. This is expressed algebraically as follows:

$$|\psi(\mathbf{r}+\mathbf{R})|^2 = |\psi(\mathbf{r})|^2. \tag{1.3}$$

Equation 1.3 implies that the wavefunction ψ has the following property:

$$\psi(\mathbf{r}+\mathbf{R}) = e^{i\alpha(\mathbf{R})}\psi(\mathbf{r}), \tag{1.4}$$

where $\alpha(\mathbf{R})$ is some function of $\mathbf{R}$. Further algebra [10] reveals properties of $\alpha(\mathbf{R})$, which allow equation 1.4 to be rewritten as

$$\psi(\mathbf{r}+\mathbf{R}) = e^{i\mathbf{k}\cdot\mathbf{R}}\psi(\mathbf{r}), \tag{1.5}$$

where $\mathbf{k}$ is a vector in *reciprocal space*, defined as

$$\mathbf{k} = l_1\mathbf{b}_1 + l_2\mathbf{b}_2 + l_3\mathbf{b}_3, \tag{1.6}$$

where $\mathbf{b}_i$ are the *primitive reciprocal lattice vectors*, which satisfy

$$\mathbf{b}_i \cdot \mathbf{a}_j = 2\pi\delta_{ij}. \tag{1.7}$$

Equation 1.5 is known as *Bloch's theorem*, and a wavefunction ψ which satisfies it is known as a *Bloch function.* It can also be stated in the alternative form:

$$\psi(\mathbf{r}) = u(\mathbf{k},\mathbf{r})\, e^{i\mathbf{k}\cdot\mathbf{r}}, \tag{1.8}$$

where $u(\mathbf{k},\mathbf{r})$ has the periodicity of the lattice. Equation 1.8 shows that Bloch's theorem predicts the nature of a particle wavefunction in a periodic potential. Despite its simple form and derivation [10], Bloch's theorem has dramatic repercussions for the particle states and dynamics. Some of these repercussions shall be explored in the remainder of this section.

The wavefunction ψ in equation 1.8 is characterised by the quantum number $\mathbf{k}$, which is known as the *wavevector*. The vector $\mathbf{k}$ has the important property that it can always be expressed within a range of values known as the *first Brillouin zone*. The first Brillouin zone is defined to be the region of reciprocal space which is closer to $\mathbf{k} = 0$ than to any other reciprocal lattice point.

In order to prove that the wavevector of a Bloch function can always be expressed by a value within the first Brillouin zone, imagine a wavefunction $\psi_{\mathbf{k}}$ that satisfies Bloch's theorem (equation 1.5) for a wavevector $\mathbf{k}$, which has a value outside the first Brillouin zone:

$$\psi_{\mathbf{k}}\left(\mathbf{r}+\mathbf{R}\right) = e^{i\mathbf{k}\cdot\mathbf{R}}\psi_{\mathbf{k}}\left(\mathbf{r}\right). \tag{1.9}$$

The equivalent wavevector inside the first Brillouin zone is $\mathbf{k}'$, which is related to $\mathbf{k}$ by

$$\mathbf{k} = \mathbf{k}' + \mathbf{K}. \tag{1.10}$$

The wavevector $\mathbf{K}$ is a reciprocal lattice vector, defined by

$$\mathbf{K} = n_1\mathbf{b}_1 + n_2\mathbf{b}_2 + n_3\mathbf{b}_3, \tag{1.11}$$

where n_i is an integer. If equation 1.10 is substituted into equation 1.9, it follows that:

$$\psi_{\mathbf{k}}\left(\mathbf{r}+\mathbf{R}\right) = e^{i(\mathbf{k}'+\mathbf{K})\cdot\mathbf{R}}\psi_{\mathbf{k}}\left(\mathbf{r}\right) = e^{i\mathbf{k}'\cdot\mathbf{R}}e^{i\mathbf{K}\cdot\mathbf{R}}\psi_{\mathbf{k}}\left(\mathbf{r}\right). \tag{1.12}$$

By definition of $\mathbf{K}$ and $\mathbf{R}$, $\mathbf{K}\cdot\mathbf{R} = 2n\pi$, where n is an integer. Consequently,

$$\psi_{\mathbf{k}}\left(\mathbf{r}+\mathbf{R}\right) = e^{i\mathbf{k}'\cdot\mathbf{R}}\psi_{\mathbf{k}}\left(\mathbf{r}\right). \tag{1.13}$$

Equation 1.13 shows that the wavefunction $\psi_{\mathbf{k}}$ satisfies Bloch's theorem for the wavevector $\mathbf{k}'$, as well as for the wavevector $\mathbf{k}$. This proves that any Bloch functions can be characterised by a wavevector within the first Brillouin zone, and that any wavevectors beyond the first Brillouin zone have an equivalent within the first Brillouin zone.

In general, the first Brillouin zone can be an awkward shape in reciprocal space, particularly for a crystal lattice with a complicated geometry. So, it is helpful to consider a specific and simple example. Let us imagine a periodic potential in which the first Brillouin zone is centred at the origin in reciprocal space. Suppose that $\mathbf{k} = \frac{\mathbf{b}_1}{2}$, which corresponds to the extreme edge of the first Brillouin zone. The opposite extreme edge of the first Brillouin zone is at $\mathbf{k}' = -\frac{\mathbf{b}_1}{2}$. Note that $\mathbf{k}$ and $\mathbf{k}'$ are related by $\mathbf{k} = \mathbf{k}' + \mathbf{K}$, where $\mathbf{K} = \mathbf{b}_1$. Hence, from the result in equation 1.13, it follows that $\mathbf{k}$ and $\mathbf{k}'$ are equivalent. The possible values of the component of $\mathbf{k}$ in the $\mathbf{b}_1$ direction is therefore given by:

$$-\frac{\pi}{d} = -\frac{|\mathbf{b}_1|}{2} \leq k \leq \frac{|\mathbf{b}_1|}{2} = \frac{\pi}{d}, \tag{1.14}$$

where d is the periodicity of the lattice in the direction $\mathbf{a}_1$.

When the Bloch functions are substituted into the Schrödinger equation (equation 1.2), it transpires that there are an infinite number of solutions for a given value of $\mathbf{k}$. Hence, each wavefunction is assigned an additional quantum number n. The energy E of the Bloch functions is a function of n and $\mathbf{k}$. This function is known as the *dispersion relation.* A typical relationship between E, n and k is shown in figure 1.1, where k is the component of the wavevector $\mathbf{k}$ in the direction $\mathbf{b}_i$. The diagram shows values of k in the first Brillouin zone only, since values outside this range have an equivalent value within this range. If k is increased beyond the edge of the first Brillouin zone, the pattern of the dispersion relation simply repeats. The representation of the dispersion relation shown in figure 1.1 is known as the *reduced zone scheme.*

The reader will notice that the energy is constrained within set ranges, and that there are forbidden regions outside these ranges where no propagating states exist. The allowed ranges of energy are called *bands*, and the forbidden regions are called *band gaps.* Each band is labelled by the quantum number n, which is known as the *band index.*

The possible values of k can be determined by applying a periodic boundary condition known as the *Born-Von Karman boundary condition.* This boundary condition requires that:

$$\psi\left(\mathbf{r}+N_i\mathbf{a}_i\right)=\psi\left(\mathbf{r}\right), \tag{1.15}$$

where N_i are integers of order $N^{\frac{1}{3}}$, such that

$$N=N_1N_2N_3, \tag{1.16}$$

where N is the total number of lattice points in the lattice. By applying this condition to Bloch's theorem (equation 1.5), it can be shown that k has the following possible values:

$$k=0,\pm\frac{\left|\mathbf{b}_i\right|}{N_i},\pm\frac{2\left|\mathbf{b}_i\right|}{N_i},\pm\frac{3\left|\mathbf{b}_i\right|}{N_i}\ldots\pm\frac{\left|\mathbf{b}_i\right|}{2}. \tag{1.17}$$

Hence, there are N_i possible values of k, and N possible values of $\mathbf{k}$ in each band.

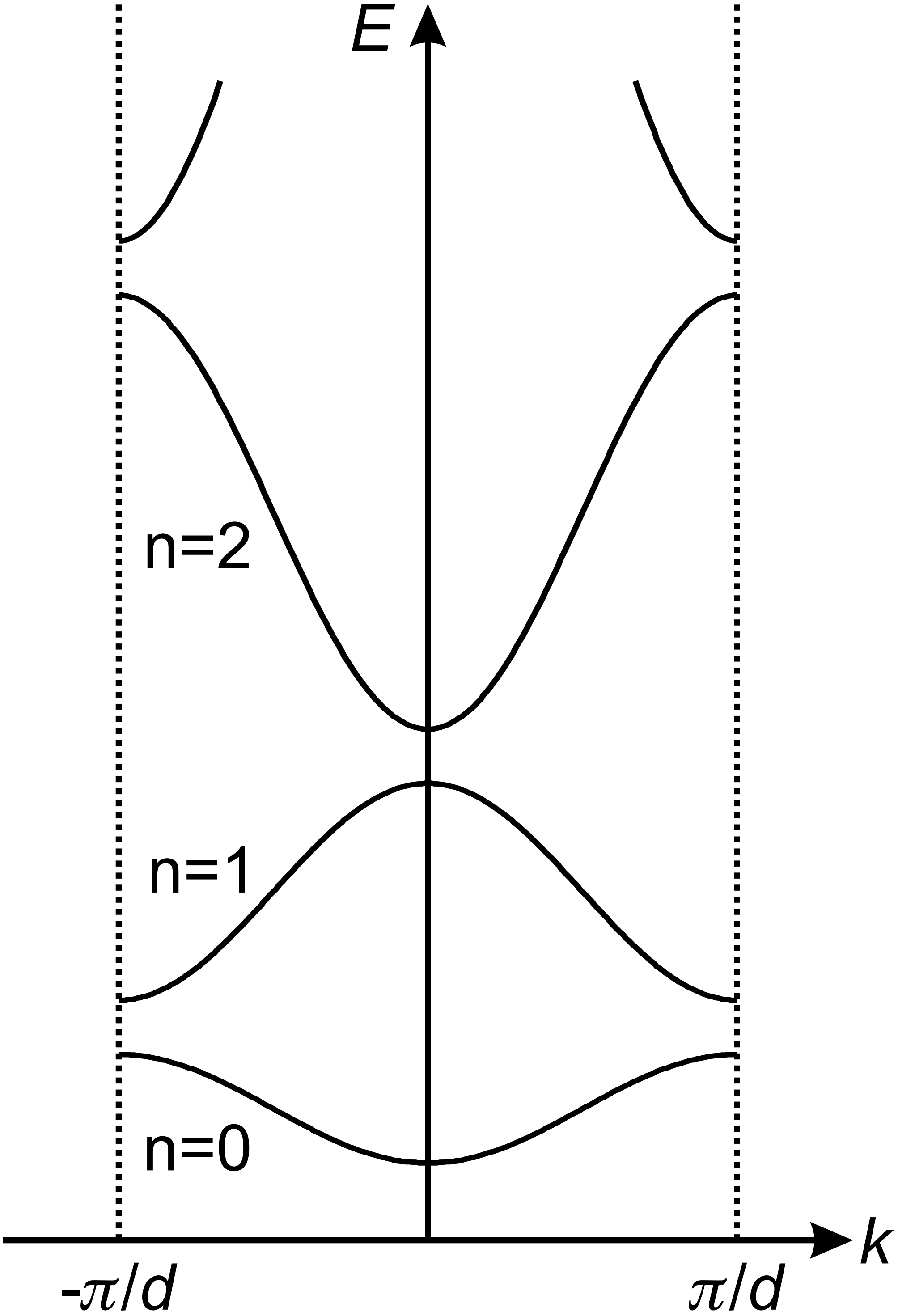

Figure 1.1: Typical dispersion relation/band structure in a periodic potential, shown in the reduced zone scheme.

1.2.1 Bragg reflection and Bloch oscillations

Imagine a wave packet of Bloch states in a given band that has a spread of wavevector components which is small compared to the width of the Brillouin zone. This infers that the wavepacket is spread in real space over many lattice points. If this wavepacket is subject to another field, called field G, which varies slowly over the dimensions of the wavepacket, the dynamics can be modelled by a *semi-classical model* [10]. The model is called semi-classical as field G is treated classically, but the periodic potential is treated quantum mechanically.

The model accepts the dispersion relation $E_n(\mathbf{k})$ as a given function, without saying anything about how it is calculated. It ignores the possibility of transitions between bands, and asserts that field G only effects the value of $\mathbf{k}$, *not* n. The force due to field G is equal to the rate of change of $\hbar\mathbf{k}$. The equations of motion are formally identical to those of a free particle in field G alone:

$$\hbar\dot{\mathbf{k}} = \text{Force due to field G} = -\nabla V_G, \tag{1.18}$$

where V_G is the potential energy due to field G. However, since the value of $\hbar\dot{\mathbf{k}}$ is not equal to the *total* force, which would include the force due to the periodic potential, $\hbar\mathbf{k}$ is *not* the momentum of the wavepacket. The quantity $\hbar\mathbf{k}$ is known as the *crystal momentum*, and is not generally conserved.

However, equation 1.18 alone is not sufficient to calculate the dynamics of the wavepacket. It describes the evolution of $\mathbf{k}$, but does not relate this to the velocity of the wavepacket. Hence, the semi-classical model uses another result, derived from perturbation theory [10], which is applied in conjunction with equation 1.18:

$$\mathbf{v}_n(\mathbf{k}) = \frac{1}{\hbar}\frac{\partial E_n(\mathbf{k})}{\partial \mathbf{k}}\,, \tag{1.19}$$

where $\mathbf{v}_n(\mathbf{k})$ is the velocity of the wavepacket.

The reader is now asked to consider a simple application of this model. Imagine a wave packet of Bloch states in the lowest band of a periodic potential. The wavevector of the wavepacket is initially tightly peaked around $\mathbf{k} = 0$. In addition to the periodic potential, the wavepacket is subject to a constant accelerating force, F, which is applied in the $\mathbf{a}_1$ direction. Under these conditions, equation 1.18 becomes:

$$\hbar \frac{dk_1}{dt} = F, \tag{1.20}$$

$$\hbar \frac{dk_2}{dt} = 0, \tag{1.21}$$

and

$$\hbar \frac{dk_3}{dt} = 0. \tag{1.22}$$

Equations 1.20 to 1.22 predict that, as t increases from zero, k_2 and k_3 will remain zero, and k_1 will increase linearly from zero.

Let us assume that the relationship between E and k_1 looks something like the dispersion relation shown in figure 1.1. Remember that the wavepacket is in the $n = 0$ band. As k_1 increases from zero the gradient of the dispersion relation becomes positive, and the kinetic energy of the wavepacket increases. Since the velocity of the wavepacket is proportional to the gradient of the dispersion curve (equation 1.19), this corresponds in real space to an acceleration from zero velocity to a positive velocity in the $\mathbf{a}_1$ direction. As k_1 increases further, the gradient of the curve reaches a maximum, and then begins to decrease. Hence, the velocity of the wavepacket reaches a maximum, and then begins to decrease. Eventually, k_1 reaches the Brillouin zone boundary, at which point the gradient of the dispersion curve is zero. Consequently, the wavepacket comes to a halt.

When k_1 reaches the edge of the first Brillouin zone, it can be equivalently expressed by the wavevector at the opposite edge of the first Brillouin zone (see previous section). So, when k_1 passes beyond the edge of the first Brillouin zone ($k = \frac{\pi}{d}$ in figure 1.1), it may be imagined to reappear at the opposite edge of the first Brillouin zone ($k = -\frac{\pi}{d}$ in figure 1.1). The wavevector k_1 then continues to increase linearly as a function of t. As the wavevector moves through the Brillouin zone boundary, the gradient of the dispersion relation decreases from a positive value, passes through zero, and continues to decrease to negative values. This means that the wavepacket is slowing to a halt, and then turning back. This process of turning around at the Brillouin zone boundary is known as *Bragg reflection* [9, 10].

The gradient of the dispersion relation is negative for negative k_1, so the wavepacket will be travelling in the $-\mathbf{a}_1$ direction. Since the dispersion relation is symmetric, the wavepacket will retrace its path exactly. When k_1 reaches zero, the wavepacket will have completed a single oscillation in real space, which is known as a *Bloch oscillation* [10].

This is a surprising result, since it suggests that electrons in a metal would oscillate when a voltage is applied, rather than produce a DC current. In fact, metals conduct because the electron scattering time is far shorter than the period of a Bloch oscillation. Consequently, the electrons scatter before completing a Bloch oscillation.

An elementary integration of equation 1.20 with respect to time yields an expression for the period of the Bloch oscillations:

$$T = \frac{h}{Fd}, \tag{1.23}$$

A similar integration of equation 1.19 yields the amplitude of the Bloch oscillations, A_{BO}:

$$A_{\mathrm{BO}} = \frac{\Delta_{\mathrm{BW}}}{F}, \tag{1.24}$$

where Δ_{BW} is the width of the band.

1.3 Atom dynamics and experimental techniques

This section discusses the behaviour of atoms in magnetic fields, electric fields and laser fields, and explains the techniques involved in cold atom experiments. In section 1.3.5, the dynamics of atoms in optical lattices are related to the band theory developed in section 1.2.

1.3.1 Response to Magnetic Fields: The Zeeman effect

This section discusses the *Zeeman effect* [1, 11, 12], which is the response of an atom to an applied magnetic field. Before this discussion begins in earnest, the reader is presented with a brief review of the relevant quantum numbers.

The quantum numbers I, S and L refer to nuclear spin, electronic spin and electronic orbital angular momentum respectively. Their corresponding operators are $\hat{\mathbf{I}}$, $\hat{\mathbf{S}}$ and $\hat{\mathbf{L}}$.

These quantum numbers are combined in the following ways to determine J and F, which are the quantum numbers of electronic angular momentum and total angular momentum respectively.

$$|L - S| \leq J \leq L + S \quad \text{(where J is an integer).} \tag{1.25}$$

$$|I - J| \leq F \leq I + J \quad \text{(where F is an integer).} \tag{1.26}$$

The corresponding operators of J and F are $\hat{\mathbf{J}}$ and $\hat{\mathbf{F}}$ respectively.

Alkali atoms are commonly used in the context of optical lattices and Bose-Einstein condensation, so this group of elements shall serve as an example for illustrating the Zeeman effect. Alkali atoms all have a common pattern to their electronic structure which enables the theorist to make some generalisations about the values of the quantum numbers discussed above. All the electrons occupy closed shells, apart from the outer electron, which is in an s-orbital. Hence, $S = \frac{1}{2}$ and $L = 0$. Consequently $J = \frac{1}{2}$ and $F = I \pm \frac{1}{2}$.

The coupling between the nuclear spin I and the total angular momentum of the electron J causes a splitting of the energy levels. Consequently, states which have different values of F for the same values of I and J are *not* degenerate. This is called the hyperfine splitting, and is described by the following Hamiltonian:

$$H_{\mathrm{hf}} = A_{\mathrm{hf}} \hat{\mathbf{I}} \cdot \hat{\mathbf{J}}, \tag{1.27}$$

where A_{hf} is a constant. If an external magnetic field is applied, the hyperfine levels are further split into Zeeman sublevels. In order to describe this effect, extra terms must be added to the hyperfine Hamiltonian. This has been done below for a magnetic field $\mathbf{B}$ which is defined to be in the z-direction [11].

$$H_{\mathrm{spin}} = A_{\mathrm{hf}} \hat{\mathbf{I}} \cdot \hat{\mathbf{J}} + C\hat{J}_z + D\hat{I}_z, \tag{1.28}$$

where

$$D = -\frac{\mu}{I}B, \tag{1.29}$$

and

$$C = g_J \mu_B B. \tag{1.30}$$

The ratio $\left|\frac{C}{D}\right| \approx \frac{m_p}{m_e} \approx 2000$ (where m_p and m_e are the proton and electron mass respectively), so for most purposes D may be neglected. This assumption is made when deriving equation 1.33. The quantity μ is the nuclear magnetic moment, and μ_B is the Bohr magneton, defined as

$$\mu_B = \frac{e\hbar}{2m_e}\,. \tag{1.31}$$

The quantity g_J is a constant which shall be referred to as the g-factor of the electron. It is defined as [1]

$$g_J = 1 + \frac{J\left(J+1\right) + S\left(S+1\right) - L\left(L+1\right)}{2J\left(J+1\right)}\,. \tag{1.32}$$

For the quantum numbers $L = 0$ and $S = \frac{1}{2}$ (appropriate for alkali atoms), $g_J = 2$.

When the eigenvalues of the Hamiltonian in equation 1.28 are determined, it transpires that in general the Zeeman energies are complicated functions which depend on the atomic state and the magnetic field. However, under certain conditions the energy of the atom varies linearly with magnetic field. For example, for magnetic fields that are small enough to ensure that the Zeeman splitting is small compared to the hyperfine splitting, the following relation holds:

$$E\left(F, m_F\right) = E\left(F\right) + m_F g_F \mu_B B, \tag{1.33}$$

where $E\left(F, m_F\right)$ is the energy of the atom, $E\left(F\right)$ is the energy of the atom in the absence of an applied magnetic field, and m_F is the quantum number for the z component of the total angular momentum F. The quantity g_F is a constant known as the *Landé g-factor*, defined as [1]

$$g_F = g_J \frac{F(F+1) + J(J+1) - I(I+1)}{2F(F+1)} \, . \tag{1.34}$$

N.B. In deriving equation 1.33 it is assumed that $|C| >> |D|$ (see equation 1.28).

As explained above, for alkali atoms $S = \frac{1}{2}$ and $L = 0$, and consequently $J = \frac{1}{2}$ and $F = I \pm \frac{1}{2}$. Typical atoms considered in the context of optical lattices and Bose-Einstein condensation are ^{87}Rb, ^{23}Na and ^{7}Li, which all have a nuclear spin quantum number $I = \frac{3}{2}$. As a result, $F = 2$ or 1, which infers Landé g-factors of $g_F = 1$ and -1 respectively.

In section 1.3.3, the effect of Zeeman splitting shall be applied to the experimental problem of trapping neutral atoms. The reader may find it useful to note that the response of an atom to a magnetic field depends not only on the component of total angular momentum in the direction of the field, but also on the corresponding Landé g-factor. Special note should be made of the states $F = 2$ $m_F = 2$ and $F = 1$ $m_F = -1$, which are known as the *doubly polarized state* and the *maximally stretched state* respectively. An inspection of equation 1.33 reveals that the energy of these states increases linearly with applied magnetic field (for small magnetic fields). This relationship between the energy of the state and the applied magnetic field provides the mechanism for the trapping techniques described in section 1.3.3

1.3.2 Response to Electric fields and Laser fields

Electric and laser fields have been used extensively to realise cold atom experiments. They play a vital role in trapping and cooling techniques, and have enabled experimentalists to create novel tools like optical lattices. An understanding of the behaviour of atoms in electric and lasers fields is crucial for the study of cold atoms [1, 11].

Consider an atom in a static electric field $\boldsymbol{\mathcal{E}}$. The atom's energy levels are shifted, and it acquires an electric dipole moment due to distortion of the electron cloud. The expectation value $< \mathbf{d} >$ of the electric dipole moment is related to the electric field via a quantity α, known as the *polarizability* of the atom [11]:

$$< \mathbf{d} >= \alpha \boldsymbol{\mathcal{E}}. \tag{1.35}$$

The energy of the atom can be determined from the following expression for the change in energy produced by a change in the electric field:

$$dE = - < \mathbf{d} > \cdot d\boldsymbol{\mathcal{E}}. \tag{1.36}$$

Upon integration of equation 1.36, the following expression for the energy of the atom is obtained:

$$\Delta E = -\frac{1}{2} \alpha \mathcal{E}^2. \tag{1.37}$$

This equation can be generalised for the case of an oscillating electric field $\mathcal{E}(t) = \mathcal{E}_0 \cos \omega t$:

$$\Delta E = -\frac{1}{2} \alpha' (\omega) < \mathcal{E} (\mathbf{r}, t)^2 >_t, \tag{1.38}$$

where $< \ldots >_t$ denotes the time average over one oscillation period of the electric field. The quantity $< \mathcal{E} (\mathbf{r}, t)^2 >_t$ is given by the relation:

$$< \mathcal{E} (\mathbf{r}, t)^2 >_t = \frac{\mathcal{E}_0^2}{2}. \tag{1.39}$$

The energy shift of the atom may be regarded as an effective potential, through which the atom travels. The associated force on the atom is known as the *dipole force*:

$$F_{\text{dipole}} = -\nabla V(\mathbf{r}) = \frac{1}{2}\alpha'(\omega)\nabla < \mathcal{E}(\mathbf{r},t)^2 >_t . \tag{1.40}$$

The result in equation 1.38 is now applied to the specific case of an atom travelling in an one-dimensional optical lattice [3, 11]. The optical lattice is formed by two counter-propagating laser beams, whose electric fields are given by:

$$\mathcal{E}_1(z,t) = \frac{\mathcal{E}_0}{2} e^{i\{kz-\omega t\}}, \tag{1.41}$$

and

$$\mathcal{E}_2(z,t) = \frac{\mathcal{E}_0}{2} e^{i\{-kz-\omega t\}}. \tag{1.42}$$

Addition of these two fields produces the following standing wave:

$$\mathcal{E}(z,t) = \mathcal{E}_1(z) + \mathcal{E}_2(z) = \mathcal{E}_0 \cos(kz)\, e^{-i\omega t}, \tag{1.43}$$

of which the real part is

$$\mathrm{Re}\{\mathcal{E}(z,t)\} = \mathcal{E}_{\text{real}}(z,t) = \mathcal{E}_0 \cos(kz)\cos(\omega t). \tag{1.44}$$

Application of equation 1.38 yields an expression for the energy shift of the atom, and an effective periodic potential through which the atom may travel.

$$\Delta E = -\frac{1}{2}\alpha'(\omega) < \mathcal{E}_{\text{real}}(z,t)^2 >_t = V_0 \cos^2(kz), \tag{1.45}$$

where V_0 is a constant, given by

$$V_0 = -\frac{\alpha'(\omega)\,\mathcal{E}_0^2}{4}. \tag{1.46}$$

Equation 1.45 shows that the period of the optical lattice is equal to half the wavelength of the counter-propagating laser beams.

In addition to the dipole force, laser fields can also exert a force on atoms via the momentum exchange on absorption of photons. Classically, this is the *radiation pressure* of the laser. Imagine a laser beam of wavevector $\mathbf{k}_p$, which illuminates a particular atom. The atom absorbs a photon, and is promoted from its ground state to an excited state. The atom acquires the photon's momentum, which is $\hbar\mathbf{k}_p$. The atom returns to the ground state by emitting a photon in a random direction, assuming that the decay occurs via spontaneous emission. Since the photon emission is in a random direction, the emission process has no net effect on the atom's momentum over a large number of absorption/emission events. Hence, the total force on the atom due to the absorption processes is given by:

$$\mathbf{F}_{\mathrm{rad}} = \hbar\mathbf{k}_p\Gamma_g, \tag{1.47}$$

where Γ_g is the rate of excitation of the ground state.

Both this force and the dipole force are exploited in laser cooling techniques, as shall be discussed in section 1.3.4.

1.3.3 Magnetic trapping

Neutral atoms can be trapped magnetically by means of the Zeeman effect, which was described in section 1.3.1. Since the energy of an atomic state is a function of magnetic field, an atom travelling in an inhomogeneous magnetic field experiences a spatially-varying potential. If the spatially-varying potential is engineered to have a minimum, the atom may be caught in a trap [1, 11]. As the atom approaches the extremity of the trap, its kinetic energy is converted to potential energy, which is stored as a shift in the atomic energy levels.

In general, the Zeeman energies are complicated functions which depend on the atomic state and the magnetic field. Consequently, in order to ensure that the atoms behave in a similar manner, the atoms are all stored in one particular atomic state. There are two states which are generally favoured for trapping alkali atoms: the *doubly polarized state* and the *maximally stretched state.* The doubly polarized state has the largest possible values of nuclear and electronic spin components in the direction of the magnetic field, i.e. $F = I + \frac{1}{2}$ and $m_F = I + \frac{1}{2}$ (see section 1.3.1 for an explanation of these quantum numbers). The maximally stretched state is characterised by the quantum numbers $F = I - \frac{1}{2}$ and $m_F = -\left(I - \frac{1}{2}\right)$. The reasons why these two atomic states are important will be revealed later in this section.

As was discussed in section 1.3.1, the energy of a state is in general a complicated function of magnetic field. However, when trapping neutral atoms, the parameters are usually chosen such that the energy of the state is linear in magnetic field. As a result, the energy of an atom in the state i can be written as

$$E_i = C_i - \mu_i B, \tag{1.48}$$

where C_i is a constant, μ_i is the magnetic moment of the state and B is the magnetic field. Equation 1.48 holds for the doubly polarised states, and is a good approximation for the other states if the Zeeman splitting is either very large or very small compared to the hyperfine splitting.

The magnetic moment μ_i can be either positive or negative. If μ_i is positive, the atom is attracted towards regions of higher magnetic field where its energy is lower (see equation 1.48), and so it is known as a *high field seeker.* If μ_i is negative, the atom is attracted towards regions of lower magnetic field, and so it is known as a *low field seeker.* The theorist might now imagine that a local maximum in the magnetic field would trap high field seekers, and a local minimum of magnetic field would trap low field seekers. Unfortunately, it is impossible to create a maximum in a magnetic field in a region where there are no electric currents. Hence, neutral atoms can be trapped magnetically *only if* they have a negative magnetic moment. The doubly polarized state and the maximally stretched state are good candidates for magnetic trapping, as both these states have a negative magnetic moment[1].

It is important that the atoms contained in a magnetic trap remain in the same atomic state. In particular, a transition from a low-field seeker state into a high field-seeker state would result in the atom being ejected from the trap. As an atom moves through a magnetic trap, it experiences a time-dependent magnetic field, which can induce transitions between Zeeman sublevels. These transitions become more probable as the frequency of the time-dependent magnetic field approaches or exceeds the frequencies of the transitions. The energies of transitions between different magnetic sublevels are of order $\mu_B B$, and vanish if $B = 0$. Consequently, transitions between atomic states may become significant if the magnetic field minimum in a magnetic trap is zero. In other words, a magnetic trap may have an effective “hole” near a node in the magnetic field.

Various solutions to this problem have been explored. One possibility is to continually shift the position of the node in the magnetic field. This is the principle of the *time-averaged orbiting potential trap*, or TOP trap. The TOP trap is characterised by a static magnetic field minimum, supplemented by a rotating, spatially-uniform, magnetic field. The frequency of

---

[1] In the case of the maximally stretched state, this is only true if the Zeeman splitting is very small compared to the hyperfine splitting (see equation 1.33).

the rotating magnetic field is chosen to be much less than the frequencies of transitions between magnetic substates, which ensures that the atoms remain in the same quantum state relative to the instantaneous magnetic field. The frequency of the rotating magnetic field is also chosen to be much greater than the frequencies of atomic motions, which ensures that the atoms feel an effective potential given by the time-average of the instantaneous potential over one period of the rotating field. These conditions typically require that the frequency of the rotating magnetic field is in the kilohertz range.

The problem of transitions between atomic states can also be overcome by creating a non-zero magnetic field minimum. A method of creating such a field profile was proposed by Ioffe [13], and so the associated trap is usually known as a *Ioffe trap.* Ioffe's method was applied to the problem of trapping neutral atoms by Pritchard [14], so the trap is alternatively known as a *Ioffe-Pritchard trap.*

Finally, the reader should also be familiar with the *magneto-optical trap*, or MOT. The MOT both traps and cools the atoms, and so is a ubiquitous feature of experiments on cold atoms. Experimentalists often find it convenient to initially trap and cool atoms in a MOT, and then transfer them to a second trap for the latter stages of the experiment. The MOT works on the principle that the radiation pressure of laser light depends on the energy levels, which are a function of the magnetic field. If the magnetic field is a function of position, then so is the radiation pressure of the laser light. By applying a counter-propagating pair of laser beams along each axis, it is possible to create a three-dimensional trap. This trap cools the atoms by the *Doppler* and the *Sisyphus* processes, which shall be described in section 1.3.4.

Generally, and for the systems considered in this thesis, the confining potential of a magnetic trap is parabolic. The potential energy of an atom in the trap can be written

$$V_{\mathrm{trap}}(x, y, z) = \frac{m}{2}\left(\omega_x^2 x^2 + \omega_y^2 y^2 + \omega_z^2 z^2\right), \qquad (1.49)$$

where m is the mass of the atom, and x, y and z are the Cartesian position coordinates. The quantities ω_x, ω_y and ω_z are constants, known as the trap frequencies. The trap frequencies are in units of rad s^{-1} in equation 1.49, but are often quoted in Hz in the literature.

1.3.4 Cooling techniques

The initial cooling of atoms is usually performed by a *Zeeman slower* [1, 11]. This device illuminates the atoms with a laser beam, which propagates in the opposite direction to the atoms. The atoms are slowed by the radiation force due to absorption of photons. The situation is complicated by the Doppler effect, since the frequency of the laser varies in the rest frame of the atoms as they slow down. This effect is counteracted by applying an inhomogeneous magnetic field. If the Zeeman shifts of the ground and excited state are different, the magnetic field can be tailored such that the Doppler and Zeeman effects cancel. As a result, a laser beam of fixed frequency in the laboratory frame resonantly excites the atoms, irrespective of their position and local velocity. Alternatively, the frequency of the laser can be varied in time, which is a process known as "chirping".

After the initial cooling in the Zeeman slower, the atoms usually undergo further cooling via a technique known as the *Doppler process* [1, 11], which works in a similar way to the Zeeman slower. Imagine two counter-propagating laser beams whose frequencies lie just below a transition between the atomic ground state and an excited state. The frequency of the laser beams in the rest frame of a particular atom depends on the velocity of the atom, according to the Doppler effect [1, 11]. Consequently, in the rest frame of a leftward-moving atom, the rightward-moving photons are Doppler shifted closer to the transition frequency, while the leftward-moving photons are Doppler shifted away from resonance. Conversely, in the rest frame of a rightward-moving atom, the leftward-moving photons are Doppler shifted closer to the transition frequency, while the rightward-moving photons are Doppler shifted away from resonance. Hence, a leftward-moving atom is more likely to absorb a rightward-moving photon, and a rightward-moving atom is more likely to absorb a leftward-moving photon. As a result, the atoms will lose kinetic energy, since they preferentially absorb photons which have momentum in an opposing direction.

The excited atoms decay back into the ground state by spontaneous emission. The photons are emitted in a random direction, so the emission process has no nett effect on the atoms' momentum over a large number of absorption/emission events.

The lowest temperature attainable through Doppler cooling is limited by the discrete size of the momentum change that the atoms undergo at each emission or absorption event. An atom at rest is equally likely to absorb a photon from either laser, and hence it performs a "random walk". Although its average momentum is zero, its root-mean-square momentum is not, and consequently the atom has a finite energy and temperature. This temperature is known as the Doppler limit, and is typically several hundred microkelvin.

More sophisticated laser cooling techniques have enabled experimentalists to cool atoms to temperatures orders of magnitude smaller than the Doppler limit. Some of these methods are known collectively as *Sisyphus cooling* [1, 11]. The atoms are illuminated by two counter-propagating laser beams, which propagate along, say, the z and negative z-direction. The electric field vectors of the laser beams are polarised in the x and y-directions respectively. The laser field produces periodic shifts in the energies of ground state magnetic substates, and pumps transitions between them. The atoms are continually forced to climb potential hills caused by the shifts in the substate energy, thus losing kinetic energy, before being pumped into a substate of lower energy. The energy lost by the atoms is radiated away. This method is called Sisyphus cooling because it is analogous to the punishment of Sisyphus, who, according to Greek myth, was condemned to push a rock up a hill for eternity in Tartarus.

Sisyphus cooling can cool atoms to a temperature T_R corresponding to a single photon recoil. This is known as the recoil energy E_R, defined as

$$E_R \equiv k_B T_R \equiv \frac{\hbar^2 k^2}{2m} \, . \tag{1.50}$$

The recoil energy typically corresponds to a temperature of a few microkelvin. It is generally regarded as the limit of laser cooling schemes, although there are some ingenious cooling methods which cool below it.

Laser cooling techniques have enabled experimentalists to reach impressively low temperatures; but even these temperatures are not low enough for some applications, such as Bose-Einstein condensation. This problem was overcome using *evaporative cooling* techniques [1, 11]. Evaporative cooling involves removing atoms which have energies higher than the average energy, and then letting the remaining gas rethermalise by elastic collisions.

This process lowers the average energy of the gas.

The theorist might imagine that high energy atoms could be removed from the gas cloud by creating a "hole" high up one side of the trap. Only atoms of energy greater than or equal to the trap potential energy at the hole would be able to escape. In practice a "hole" is created by using radio-frequency radiation to flip the spin state of the atoms from a *low-field seeking state* to a *high-field seeking state* (see section 1.3.3 for an explanation of these terms). The technique works as follows.

The energy level shifts due to the Zeeman effect are a function of the position of the atom in the magnetic trap. Consequently, the resonant frequency of a transition to a particular high-field seeking state is also a function of position. It is hence possible to tune the frequency of the rf radiation in order to control where atoms are flipped into a high-field seeking state. Thus the experimentalist controls the position of the "hole" in the trap. Gas clouds are progressively cooled by adjusting the frequency of the radiation to expel atoms of lower and lower energy from the trap.

1.3.5 Atom dynamics in a band structure

As explained in section 1.3.2, atoms experience an optical lattice as a periodic potential (see equation 1.45). Similarly, electrons experience a crystal lattice as a periodic potential. Hence, the physics of both systems is described by band theory (see section 1.2), and their dynamics are qualitatively similar. However, due to the differences in the physical nature of the two systems, the atom dynamics are far more experimentally accessible than the electron dynamics (the reasons for this were explained in section 1.1). As a result, atoms in optical lattices represent an experimental opportunity to investigate some of the predictions of solid state physics.

Atoms in optical lattices can demonstrate both semi-classical and full quantum-mechanical band transport. The semi-classical approach to band theory predicts that particles in a band undergo oscillations when subject to a linear accelerating force. These oscillations are known as Bloch oscillations (see section 1.2). They are not observed in normal crystal lattices because the electron scattering time is far shorter than the period of the Bloch oscillations. Consequently, the electrons scatter before completing a Bloch oscillation. Electrons can perform Bloch oscillations in semiconductor superlattices, since these structures have far greater lattice constants, and hence far shorter Bloch periods (see equation 1.23). Bloch oscillations in superlattices have been observed indirectly by detecting THz radiation emitted by the oscillating electrons [15].

Bloch oscillations with far longer periods can occur in optical lattices since the atoms undergo virtually no scattering. This is because the optical lattice has no defects and no lattice vibrations. In contrast to the superlattice experiments, the Bloch oscillations of atoms in optical lattices can be observed directly. After a given evolution time, the optical potential is switched off abruptly and the momentum of the atoms is measured. This technique allows the experimentalist to plot the velocity-time curves of the atoms. Bloch oscillations of atoms in optical lattices were first observed in this way by Ben Dahan et al. in 1995 [5].

In the full quantum-mechanical picture, a periodic potential with a linear accelerating force produces equally-spaced energy levels, known as a Wannier-Stark ladder. These energy levels are the quantised states corresponding to the semi-classical Bloch oscillations. Wannier-Stark ladders in optical lattices were first observed by S.R. Wilkinson et. al. in 1996 [7].

Chapter 2

Chaos theory

2.1 Introduction

The term chaos was coined to describe complex motion observed in seemingly simple experiments and theoretical simulations [16]. Chaotic systems are characterised by erratic, apparently random motion. Chaotic trajectories are aperiodic, and show extreme sensitivity to the initial conditions. The motion is typically reminiscent of random "noise".

Despite this complexity, chaos is found in systems which are *deterministic* [17, 18]. This means that given a set of initial conditions, the parameters of the system, and the equations of motion, it is hypothetically possible to calculate the dynamics for all times. If the equations of motion are known, then the theorist is, in principle, able to predict future behaviour for particular parameters, and the system is called a *dynamical system* [17, 18]. The theorist may then wonder how to reconcile the ideas of determinism with chaos. The future behaviour of the system is completely described by known, and often very simple equations of motion; and yet, the dynamics show no obvious pattern or order.

A detailed study of chaos reveals that beyond the initial discovery of the apparently random dynamics there are common features of chaos. Many, often very different, chaotic systems show similar behaviour which can be categorised and treated in the same way. This chapter examines the threads which link chaotic systems, and hence shows how chaos can be understood.

2.2 Classical chaos

Chaos was originally conceived in terms of classical mechanics, and was subsequently investigated in the quantum mechanical regime. A study of quantum chaos requires a prior understanding of classical chaos. This section examines the ideas of classical chaos, and section 2.3 explains how those ideas are embodied in the quantum mechanics.

2.2.1 Hamiltonian systems

Chaos is studied in two types of system: *dissipative* systems and *Hamiltonian* systems (also known as *conservative* systems) [17, 18, 19]. In dissipative systems, the trajectories approach a limiting set, known as an *attractor*, as time or the number of iterations goes to infinity. This process is known as *dissipation*. In contrast, Hamiltonian systems are dynamical systems which have no dissipation, and so the trajectories do not converge onto a limiting set, no matter how long the experiment or simulation runs. This study of chaos is limited to Hamiltonian systems. This section describes the properties of Hamiltonian systems, and the equations which govern them.

The dynamics of a Hamiltonian system are described in terms of the position and momentum of the particle or particles. Conventionally, each component of position and momentum is denoted by the symbols q_i and p_i respectively. If the system involves the motion of just one particle, the subscript i denotes a particular coordinate axis. If the system consists of more than one moving particle, the subscript i denotes a particular coordinate axis and a particular particle. Each pair q_i, p_i is known as a *degree of freedom* of the system.

For each Hamiltonian system there is a corresponding function $H(\mathbf{p}, \mathbf{q}, t)$, known as the *Hamiltonian*, which completely specifies the dynamics [17, 18, 19]. The Hamiltonian is related to the q_i and p_i variables via Hamilton's equations [17, 18, 19], given by

$$\frac{dq_i}{dt} = \frac{\partial H(\mathbf{q}, \mathbf{p}, t)}{\partial p_i} \tag{2.1}$$

and

$$\frac{dp_i}{dt} = -\frac{\partial H(\mathbf{q}, \mathbf{p}, t)}{\partial q_i} . \tag{2.2}$$

If a Hamiltonian system has N degrees-of-freedom, the corresponding Hamilton's equations are a set of $2N$ coupled differential equations.

Now consider the temporal derivative of the Hamiltonian. This is determined via the chain rule of differentiation:

$$\frac{dH(\mathbf{p}, \mathbf{q}, t)}{dt} = \sum_i \left\{ \frac{\partial H}{\partial p_i} \frac{dp_i}{dt} + \frac{\partial H}{\partial q_i} \frac{dq_i}{dt} \right\} + \frac{\partial H}{\partial t} . \tag{2.3}$$

The temporal derivative is composed of contributions from two sources: the explicit and implicit time-dependence of the Hamiltonian. Explicit time-dependence of the Hamiltonian refers to terms in the Hamiltonian which directly (or *explicitly*) contain t. Differentiation of such terms make up the final term on the right-hand side of equation 2.3. Implicit time-dependence of the Hamiltonian refers to terms in the Hamiltonian which have an indirect (or *implicit*) dependence on t. Specifically, the Hamiltonian contains terms in p_i and q_i which (in general) depend on t. This implicit time-dependence is responsible for the terms within the summation on the right-hand side of equation 2.3.

Equation 2.3 can be simplified by using Hamilton's equations to make appropriate substitutions:

$$\frac{dH(\mathbf{p},\mathbf{q},t)}{dt} = \sum_i \left\{ \frac{\partial H}{\partial p_i}\left(-\frac{\partial H}{\partial q_i}\right) + \frac{\partial H}{\partial q_i}\left(\frac{\partial H}{\partial p_i}\right) \right\} + \frac{\partial H}{\partial t}\,, \tag{2.4}$$

which reduces to

$$\frac{dH(\mathbf{p},\mathbf{q},t)}{dt} = \frac{\partial H}{\partial t}\,. \tag{2.5}$$

In the special case of Hamiltonians with no explicit time-dependence, $H(\mathbf{p},\mathbf{q})$ is a constant. If H represents the total energy of the system, (as is usually the case), then it follows that the energy is conserved. We now see why Hamiltonian systems are sometimes called *conservative* systems: they often have one or more physical properties which remain constant in time, which are usually referred to as *conserved quantities*. Sometimes these properties are quantities which are commonly known to be conserved, such as energy or momentum. Sometimes the conserved properties are more obscure, and difficult to discover.

The reader should note the implication that by defining Hamiltonian systems as "dynamical systems with no dissipation", it does not follow that energy is necessarily conserved. The Hamiltonian could be periodic in time, due to, say, an externally-applied time-dependent force. However, the Hamiltonian studied in this report (chapter 4) has no explicit time-dependence, so the energy of the system in this particular case *is* conserved.

It is possible to test whether a particular function f is conserved by calculating a quantity known as the Poisson bracket of f and H. Consider the temporal derivative of f:

$$\frac{df}{dt} = \frac{\partial f}{\partial t} + \frac{\partial f}{\partial \mathbf{q}}\frac{d\mathbf{q}}{dt} + \frac{\partial f}{\partial \mathbf{p}}\frac{d\mathbf{p}}{dt}\,. \tag{2.6}$$

By using Hamilton's equations to make substitutions, equation 2.6 becomes:

$$\frac{df}{dt} = \frac{\partial f}{\partial t} + \frac{\partial f}{\partial \mathbf{q}}\frac{\partial H}{\partial \mathbf{p}} - \frac{\partial f}{\partial \mathbf{p}}\frac{\partial H}{\partial \mathbf{q}} = \frac{\partial f}{\partial t} + [f, H]\,, \tag{2.7}$$

where

$$[f, H] = \frac{\partial f}{\partial \mathbf{q}}\frac{\partial H}{\partial \mathbf{p}} - \frac{\partial f}{\partial \mathbf{p}}\frac{\partial H}{\partial \mathbf{q}}\,. \tag{2.8}$$

The quantity $[f, H]$ is known as the Poisson bracket of f and H. It follows from equation 2.7 that if the function f is conserved then it must have the property

$$[H, f] = \frac{\partial f}{\partial t}\,. \tag{2.9}$$

If f has no explicit time-dependence, then equation 2.9 simplifies to:

$$[H, f] = 0. \tag{2.10}$$

N.B. If H is not time-independent then the Poisson Bracket $[H, f]$ may also not be time-independent. Consequently, to be sure that f is a conserved quantity equation 2.10 must hold, f must have no explicit time-dependence, *and* H must be time-independent.

At this point, it is appropriate to introduce the concept of *phase space* [18, 19]. This is a useful tool to aid understanding of the dynamics of Hamiltonian systems. When considering the motion of an object, it is natural to imagine the trajectory being traced out in *real space*. *Real space* is simply a region with the dimensionality of the problem, in which the axes give position values (q_i values). In short, *real space* corresponds to what is normally considered as *space*. However, it is also possible to trace out trajectories in *phase space*, in which the axes give both position (q_i) and momentum (p_i) values. As there is both a p_i and a q_i associated with each degree-of-freedom, the phase space for a Hamiltonian system with N degrees-of-freedom is $2N$-dimensional. Plotting trajectories in this way provides the theorist with a more comprehensive description of the system's behaviour, since the combination of all the p_i and q_i values completely specifies the dynamics at that instant.

As the complexity of the system increases, it rapidly becomes difficult to visualise the corresponding multi-dimensional phase space. Hence, it is often more convenient to consider a particular plane in the phase space, rather than the phase space in its entirety. This idea is explored in section 2.2.4.

It was established earlier in this section that in the special case of Hamiltonians with no explicit time-dependence, the value $H(\mathbf{p}, \mathbf{q})$ is a constant (see equation 2.5). If this is the case, every point on a particular trajectory in phase space must have the same value of $H(\mathbf{p}, \mathbf{q})$. This restricts the number of dimensions through which the trajectory can travel. Specifically, if such a system has N degrees-of-freedom, the trajectory is restricted to a $(2N-1)$-dimensional surface in a $2N$-dimensional phase space.

It was also established earlier in this section that a particular Hamiltonian system may have more than one conserved quantity (a physical property which remains constant in time). If this is the case, there will be further restrictions on the dimensionality of the phase space trajectories. Generally, if a particular system has N degrees-of-freedom and k conserved quantities, the trajectory is restricted to a $(2N-k)$-dimensional surface in a $2N$-dimensional phase space. If k is equal to N, there are profound implications for the behaviour of the system, which shall be discussed in the following section.

2.2.2 Integrable systems, non-integrable systems and chaos

Hamiltonian systems can be divided into two classes: *integrable* systems and *non-integrable* systems [17, 18, 19, 20]. This classification is important in the study of chaos, since chaotic behaviour can only occur in non-integrable systems. The transition to chaos takes place when a small change in the conditions results in a formerly integrable system becoming non-integrable.

An integrable system is defined as a Hamiltonian system which has as many *independent* conserved quantities as degrees-of-freedom. A set of N conserved quantities $J_i, i = 1, 2, \ldots, N$ are said to be independent if no one of them can be expressed as a function of the $(N - 1)$ other quantities. Strictly, any pair of the N conserved quantities must have a Poisson bracket equal to zero, i.e. $[J_i, J_k] = 0$ for all i and k. If this condition is fulfilled, the conserved quantities are said to be *in involution*. A non-integrable system is defined as a Hamiltonian system which has fewer conserved quantities than degrees-of-freedom.[1]

Consider the trajectories of an integrable system in phase space. An integrable system with N degrees-of-freedom must have N conserved quantities, and so the trajectory is restricted to an N-dimensional surface in a $2N$-dimensional phase space. This surface is known as a *torus*, and is represented schematically in figure 2.1(a). The trajectory is free to move anywhere on the surface of the torus, but it is forbidden to leave the surface of the torus. This representation of the motion enables the theorist to define

---

[1] It is a simplification to imagine that there is a clear distinction between integrable and non-integrable systems. Some systems have both integrable and non-integrable regions in their phase space.

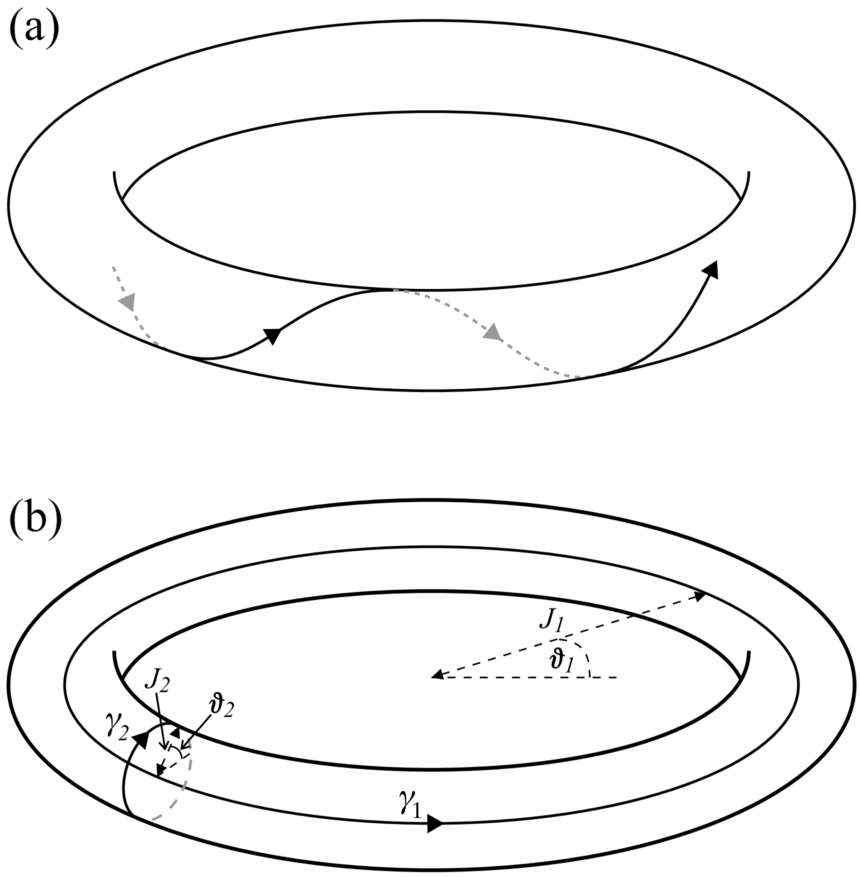

Figure 2.1: (a) Schematic representation of a phase space trajectory which lies on the surface of a torus. (b) The irreducible paths γ_i defined by action-angle variables J_i and ϑ_i.

a quantity known as the *winding number*. The winding number is the number of times a trajectory winds around the small cross-section of the torus in one complete circuit of the large cross-section of the torus.

The reader should be aware that figure 2.1(a) is just a representation to aid understanding, and is not strictly correct. As was explained in the previous section, the phase space for a Hamiltonian system with N degrees-of-freedom is $2N$-dimensional. Consequently, the phase space of any Hamiltonian system must have an even number of dimensions. However, the torus in figure 2.1(a) resides in a three-dimensional space. To correctly

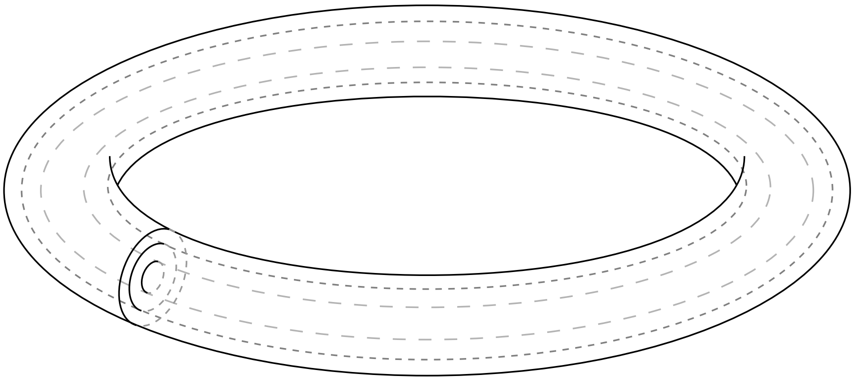

Figure 2.2: Schematic representation of nested tori in phase space.

represent the phase space of an integrable system with, say, two degrees-of-freedom, it is required to draw the two-dimensional surface of a torus in a four-dimensional space. This is obviously impossible, so figure 2.1(a) must suffice as a representation of the phase space for an integrable system.

The surface of each torus in phase space represents a particular set of values of the N conserved quantities. Hence, two tori corresponding to different sets of values of the conserved quantities cannot meet or cross each other. Consequently, the phase space of an integrable system is filled with nested tori (see figure 2.2).

Hitherto, the dynamics of Hamiltonian systems have been described in terms of position and momentum variables, q_i and p_i. For a Hamiltonian system with N degrees-of-freedom there have been N q variables and N corresponding p variables. Given an integrable system, it is possible to perform a change of variables such that the system is described by N J variables which are conserved quantities, and N corresponding ϑ variables. This approach considerably simplifies the problem, and consequently the dynamics become easier to solve.

The J_i and ϑ_i values (where $i = 1, 2, 3, \ldots N$) are called *action variables* and *angle variables* respectively. They are chosen such that Hamilton's equations can be re-written in terms of J_i and ϑ_i, without altering their original mathematical forms:

$$\frac{d\vartheta_i}{dt} = \frac{\partial H}{\partial J_i} , \tag{2.11}$$

$$\frac{dJ_i}{dt} = -\frac{\partial H}{\partial \vartheta_i} . \tag{2.12}$$

Changes of variables such as this which preserve the original form of the equations are known as *canonical changes of variables.*

Consider the trajectories of an integrable system in the new phase space, in which the axes denote J_i values and ϑ_i values. As before, the trajectories are constrained to move on the surface of a torus, as represented in figure 2.1(b). Position on the torus is denoted by the sum of two vectors, whose lengths are J_1 and J_2, and whose orientations are described by the angles ϑ_1 and ϑ_2. The trajectory around the torus can be described in terms of the irreducible paths γ_1 and γ_2. These irreducible paths are traced out by holding one value of ϑ_i constant, while the other is varied. (As before, the reader should be aware that figure 2.1(b) is merely a schematic representation of phase space.)

Several conditions have already been set on the values of J_i and ϑ_i, but these do not provide an *exclusive* definition of the action-angle variables. Usually, J_i is defined precisely as follows:

$$J_i = \frac{1}{2\pi} \oint_{\gamma_i} \mathbf{p} \cdot d\mathbf{q}, \tag{2.13}$$

where the symbol $\oint_{\gamma_i}$ represents an integral around the i^{th} irreducible path. The integral $\int \mathbf{p} \cdot d\mathbf{q}$ is referred to as the *action integral*, or the *classical* *action*, or simply the *action*, and is usually denoted by the symbol S:

$$S = \int \mathbf{p} \cdot d\mathbf{q}. \tag{2.14}$$

The action of a closed orbit is a measure of the phase space area enclosed by the trajectory. The action is a ubiquitous quantity in mechanics, and several important results are derived from it. A lengthy proof [20] shows that the derivative of the action of a particular closed orbit with respect to energy is equal to the period of the orbit T:

$$\frac{\partial S}{\partial E} = T. \tag{2.15}$$

Since the action variables J_i are chosen to be constants of the motion, $\frac{dJ_i}{dt} = 0$. Consequently, equation 2.12 shows that the Hamiltonian function depends on the J_i's only, and *not* on the ϑ_i's. These considerations enable us to re-write equation 2.11 with the following amendments:

$$\frac{d\vartheta_i}{dt} = \frac{\partial H\left(\mathbf{J}\right)}{\partial J_i} \equiv \omega_i\left(\mathbf{J}\right). \tag{2.16}$$

The variable ω_i is a number which depends on all the J_i's. Since the J_i's are all constants of the motion, ω_i must also be a constant of the motion. Hence, equation 2.16 can be immediately integrated:

$$\vartheta_i = \omega_i t + \vartheta_i\left(0\right). \tag{2.17}$$

Amazingly, equation 2.17 represents a complete solution of the dynamics for an integrable system.

Equation 2.17 states that $\vartheta_i \to \infty$ as $t \to \infty$. This suggests that some measurable parameter might tend to infinity, which is impossible to understand if the system is spatially bounded. In fact, it transpires that ϑ_i increases by 2π upon one circuit around the irreducible path γ_i on the torus in phase space. Hence, increasing ϑ_i by 2π results in no net change of position in phase space. This is why the ϑ_i's are called *angle variables.* This result can be proved as follows.

Canonical changes of variables can be specified by means of a generating function G, which is a function of one 'old' variable and one 'new' variable (and possibly time t). G can be defined as follows:

$$\boldsymbol{\vartheta} = \frac{\partial G\left(\mathbf{J}, \mathbf{q}, t\right)}{\partial \mathbf{J}}\,, \tag{2.18}$$

$$\mathbf{p} = \frac{\partial G\left(\mathbf{J}, \mathbf{q}, t\right)}{\partial \mathbf{q}}\,. \tag{2.19}$$

So, a change of variables from $\{\mathbf{p}, \mathbf{q}\}$ to $\{\mathbf{J}, \boldsymbol{\vartheta}\}$ could be performed by solving equation 2.19 for $\mathbf{J}$ in terms of $\mathbf{p}$ and $\mathbf{q}$, and then substituting the solution into equation 2.18 to obtain $\boldsymbol{\vartheta}$ in terms of $\mathbf{p}$ and $\mathbf{q}$.

The proof proceeds by integrating both sides of equation 2.19 with respect to $\mathbf{q}$ around one circuit of the irreducible path γ_i:

$$\Delta_i G = \oint_{\gamma_i} \mathbf{p} \cdot d\mathbf{q}, \tag{2.20}$$

where $\Delta_i G$ is the change in the generating function upon one circuit around the irreducible path γ_i. By the definition of J_i given in equation 2.13,

$$\Delta_i G = 2\pi J_i. \tag{2.21}$$

From equation 2.18 it follows that:

$$\Delta_i \boldsymbol{\vartheta} = \frac{\partial}{\partial \mathbf{J}} \Delta_i G, \tag{2.22}$$

where $\Delta_i \boldsymbol{\vartheta}$ is the change in $\boldsymbol{\vartheta}$ upon one circuit around the irreducible path γ_i. By substituting for $\Delta_i G$ using equation 2.21,

$$\Delta_i \boldsymbol{\vartheta} = 2\pi \frac{\partial}{\partial \mathbf{J}} J_i. \tag{2.23}$$

Hence,

$$\Delta_i \vartheta_j = 2\pi \delta_{ij}, \tag{2.24}$$

which is the desired result ($\delta_{ij} \equiv 1$ if $i = j$ and $\delta_{ij} \equiv 0$ if $i \neq j$).

From these considerations the reader will conclude that the winding number for the torus in the action-angle phase space is simply the ratio of the angular frequencies ω_i in equation 2.17. For the torus in figure 2.1(b), the winding number is $\frac{\omega_2}{\omega_1}$.

As a consequence of the result obtained in equation 2.24, equation 2.17 for a particular i is now recognised as oscillatory motion. The *overall* dynamics depend on the relative values of the ω_i's. If the ω_i's are commensurate (i.e. have a rational ratio), then the trajectories are periodic in phase space. (Equivalently, if the winding number is rational, then the trajectories are periodic in phase space.) This means that the trajectories return to their starting conditions after a time t. If the trajectories return to the same point in phase space after a time t, they must also return to the same point in real space after a time t. Consequently, periodic motion in phase space corresponds to periodic motion in real space. If the ω_i's are not commensurate (i.e. have an irrational ratio), then the trajectories are quasi-periodic in phase space. (Equivalently, if the winding number is irrational, then the trajectories are quasi-periodic in phase space.) This means that they eventually explore the entire surface of the torus in phase space, and return arbitrarily close to their starting conditions after a time t. If the trajectories return arbitrarily close to the same point in phase space after a time t, they must also return arbitrarily close to the same point in real space after a time t. Consequently, quasi-periodic motion in phase space corresponds to quasi-periodic motion in real space. By means of this reasoning, the reader will conclude that integrable systems must produce either periodic or quasi-periodic motion.

Although chaos has not yet been strictly defined, it will be obvious to the reader that the periodic or quasi-periodic motion of integrable systems cannot produce its distinctive apparently random motion. Chaotic systems *must* be non-integrable. However, non-integrability is not the definition of chaos, although the vast majority of non-integrable systems *are* chaotic[2]. Chaos is defined in terms of the divergence of the trajectories, which shall be discussed in the following section.

2.2.3 The definition of chaos and the Lyapunov exponent

Chaotic motion is defined by its exponential sensitivity to the initial conditions [17, 18, 19]. Imagine two trajectories which initially have an arbitrarily small separation, Δ_0, in phase space. If the motion is chaotic, the separation of these two trajectories in phase space $\Delta_r(t)$ must increase exponentially in time, as follows:

$$\Delta_r(t) = \Delta_0 e^{\iota t}. \tag{2.25}$$

(If the system is not chaotic, the divergence of the two trajectories is, at worst, polynomial in time.) The quantity ι determines the rate of divergence. It is known as the *Lyaponuv exponent* [17, 18, 19]. If the motion is chaotic then it must have a real positive value.

---

[2] There is a class of "pseudo-integrable" systems which are non-integrable but not chaotic. However, such systems are unusual and are not considered in this thesis.

Given the equations which govern a chaotic system, and the initial conditions, a theorist might naively suppose that he could determine the future motion for all time. A system which has this property is known as a *deterministic system*. However, in any real experiment, or for that matter any real numerical simulation, the initial conditions are specified to a finite accuracy. Since chaotic systems are so sensitive to initial conditions, for a sufficiently large elapsed time the theorist's predictions will be incorrect. Consequently, chaotic systems are *unpredictable*, despite being *deterministic.*

Since integrable systems only exhibit periodic and quasi-periodic motion, their phase spaces cannot have real positive Lyaponuv exponents. If the Lyaponuv exponents are not real positive, the motion is said to be *stable.* The transition to chaos in Hamiltonian systems occurs when a perturbation results in a formerly integrable system becoming non-integrable, allowing the Lyaponuv exponent in particular regions of phase space to become real positive. In the regions of phase space where the Lyaponuv exponent becomes real positive, the trajectories move off their respective tori, and explore the phase space more freely. In the regions of phase space where the Lyaponuv exponent does not become real positive, the tori remain, but are distorted by the perturbation. If the phase space shows a mix of stable and chaotic behaviour, it is said to exhibit *weak chaos.* If the system continues to be perturbed such that all of the tori break up and the entire phase space has a positive Lyaponuv exponent, the system is said to exhibit *strong chaos.*

2.2.4 Poincaré sections

As the complexity of the system increases, it rapidly becomes difficult to visualise the corresponding multi-dimensional phase space. Hence, it is often more convenient to consider a particular plane, rather than the phase space in its entirety. Such a plane is known as a *Poincaré section* [18, 19, 20].

For example, consider a Hamiltonian system that has two degrees of freedom, and obeys conservation of energy. The corresponding phase space is four-dimensional, but is effectively reduced to three dimensions due to the constraint imposed by conservation of energy. A plane in phase space is now selected, defined by, say, $p_1 = 0$. This plane cuts through any tori or chaotic regions that reside in the phase space. For example, figure 2.3(a) shows a set of nested tori intersecting a suitable plane in phase space. In general, the pattern on the chosen plane will resemble one of the diagrams in figure 2.3.

First, imagine the trajectory under consideration is periodic, and it strikes the Poincaré section at a point (x, y) at time $t = 0$. It will return to this point exactly after the period of the orbit, T, has elapsed. Between the times $t = 0$ and $t = T$, the trajectory may have struck the Poincaré section many times, or it may not have struck it at all. However, it must have struck the Poincaré section a *finite* number of times. Hence, the Poincaré section will consist of a finite number of dots, as is illustrated in figure 2.3(b).

Now imagine a similar quasi-periodic orbit. If the system is allowed to evolve for a sufficiently long time, the trajectory will explore the entire surface of its torus. Hence, the trajectory will eventually strike the Poincaré section at every point where its torus intersects the Poincaré section. Consequently, the points on the Poincaré section will lie on a closed loop, which corresponds to the cross-section of the torus in the chosen plane of phase space, as shown in figure 2.3(c).

If the motion is chaotic, the trajectories will not be constrained to lie on tori. Consequently, they may strike the chosen plane in phase space at any point, their only constraint being conservation of energy. The re-

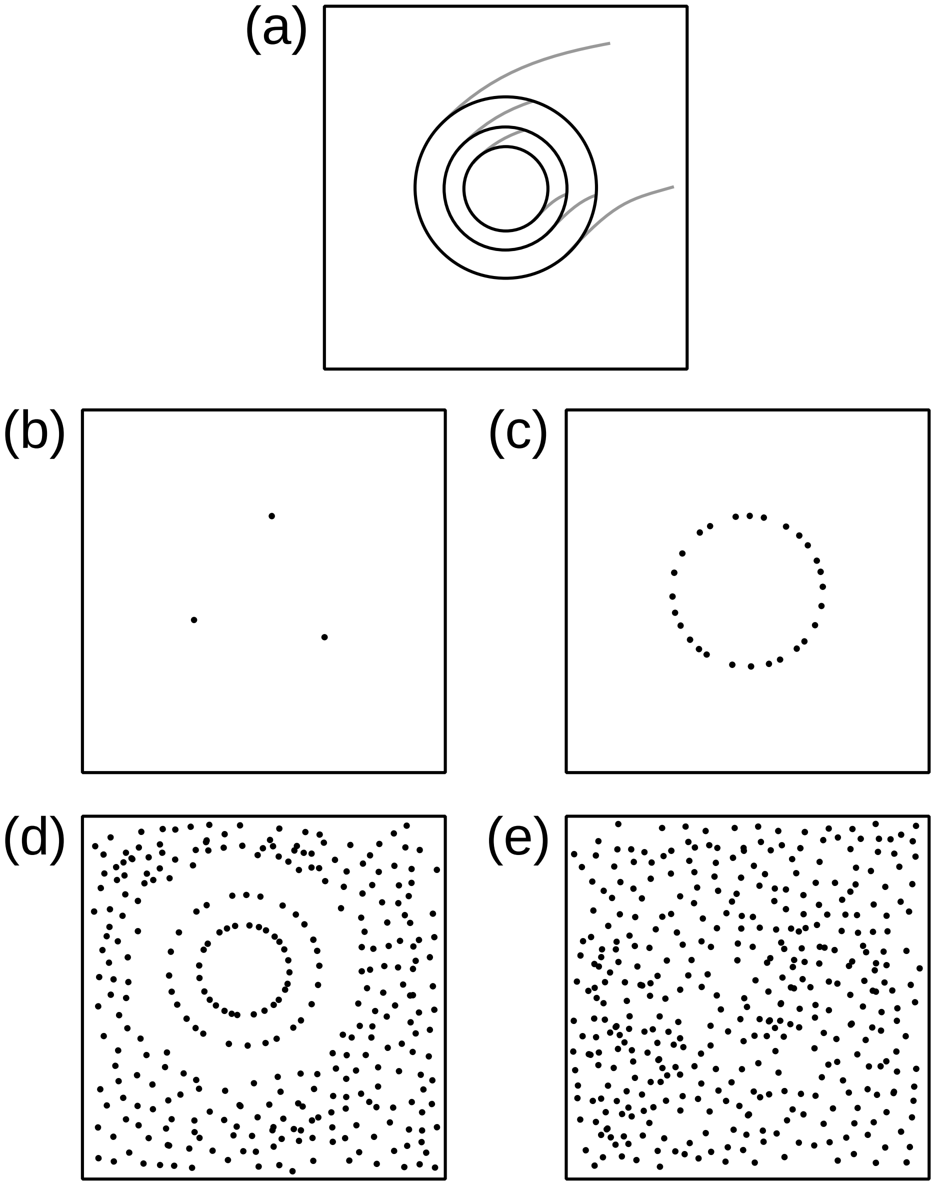

Figure 2.3: Schematic representation of (a) nested tori intersecting a plane in phase space (b) Poincaré section of a periodic orbit (c) Poincaré section of a quasi-periodic orbit (d) Poincaré section of mixed stable/chaotic phase space (e) Poincaré section of a strongly chaotic phase space

sulting Poincaré section is an apparently random distribution of points (see figure 2.3(e)), which is often referred to as a *chaotic sea.* If the system exhibits a mix of stable and chaotic motion, the Poincaré section will show a combination of closed loops, corresponding to stable tori, and chaotic seas, indicating the chaotic regions of phase space (figure 2.3(d)).

The choice of plane is generally not crucial, as long as the trajectories cut it approximately transversely. In other words, they do not run parallel or approximately parallel to the plane.

N.B. Poincaré sections are only easy to understand and interpret if the phase space is effectively three-dimensional. If the phase space has more than three dimensions, a two-dimensional Poincaré section could in principle be defined by constraining more than one variable. However, it is likely that many trajectories would not strike a plane defined in this way, and so the Poincaré section would be unlikely to contain enough information to be an adequate representation of the phase space as a whole.

2.3 Quantum chaos

Hitherto, the entire discussion of chaos and its definition have relied on the concept of the trajectory. It is therefore difficult to envisage how these ideas will translate into quantum mechanics since the concept of the trajectory is meaningless on a quantum level. This problem can be expressed more fundamentally by considering the classical phase space, and the quantum equivalent. The continuous nature of a trajectory infers that it is possible to precisely define a point in phase space. Furthermore, chaotic trajectories are aperiodic, and can pass arbitrarily close to any given point in phase space (subject to the constraints of the system), which suggests that the description of chaos requires an infinitely detailed phase space. The very definition of chaos is in terms of trajectories which are initially arbitrarily close in phase space. However, in quantum mechanics, the detail of the phase space is limited by Heisenberg's position-momentum uncertainty principle:

$$\Delta x \Delta p \geq \frac{\hbar}{2} \, . \tag{2.26}$$

Hence, the classical description and definition of chaos breaks down in a quantum-mechanical picture.

The reader may then ask what the term "quantum chaos" actually means. In fact, the term is misleading, because chaos as defined classically cannot exist on a quantum level. A more precise, but less concise name of this topic might be "the study of quantum systems which have a chaotic classical analogue." However, despite its unfortunate connotations, the name "quantum chaos" has now become the accepted name of this topic.

The reader may now ask whether quantum chaos is an interesting topic if quantum mechanics cannot display the intriguing behaviour which has been demonstrated in the classical regime. In response to this question, the reader is asked to recall that the Correspondence Principle dictates that the classical and quantum descriptions of any given system should converge in the limit of high quantum numbers, when the spacing between energy levels is much less than the energy. Equivalently, the condition is met as $h \to 0$, whilst holding all other system parameters constant. Hence, the theorist would expect there to be some links between the classical and quantum analysis, at least in the limit of high quantum numbers. The topic of quantum chaos is largely concerned with discovering these links.

2.3.1 Energy level statistics

In any quantum mechanical system the number of energy levels below a particular energy E is given by the following 'staircase' function:

$$N(E) = \sum_{n} \Theta(E - E_n), \tag{2.27}$$

where Θ is the step function of unit height ($\Theta(x) \equiv 1$ if $x > 0$ and $\Theta(x) \equiv 0$ if $x \leq 0$). Due to energy quantisation, $N(E)$ is necessarily a series of abrupt jumps of unit height. However, over large ranges of energy this series of discontinuities approximately follows a smooth curve. Hence $N(E)$ can be expressed as the sum of a slowly-varying component $N_{AV}(E)$, and a rapidly-oscillating component $N_{OS}(E)$:

$$N(E) = N_{AV}(E) + N_{OS}(E). \tag{2.28}$$

Equivalently, this can be expressed in terms of the density of states of the system, defined as follows [19, 20, 21]:

$$D(E) = \frac{dN(E)}{dE} = D_{AV}(E) + D_{OS}(E), \tag{2.29}$$

where $D_{AV}(E) = \frac{dN_{AV}(E)}{dE}$ and $D_{OS}(E) = \frac{dN_{OS}(E)}{dE}$.

This section examines N_{AV} and N_{OS} (or equivalently D_{AV} and D_{OS}) for quantum systems which have chaotic classical analogues. It discusses the meanings of N_{AV} and N_{OS}, and how they can be approximated from the corresponding classical mechanics.

The Weyl formula

As explained in the previous section, the number of levels below an energy E is composed of a slowly-varying component $N_{AV}(E)$ and a rapidly-oscillating component $N_{OS}(E)$. The Weyl formula [17, 20, 22] enables the theorist to calculate $N_{AV}(E)$ from the classical mechanics. The formula is based on the idea that a state in a system with N degrees of freedom occupies, on average, a volume of h^N in phase space. Hence, it is possible to determine the number of states below an energy E by calculating the available volume in phase space below energy E, and dividing the result by h^N. This is expressed mathematically as follows:

$$N_{AV}(E) = \frac{1}{h^N} \int \Theta\left(E - H\left(\mathbf{p}, \mathbf{q}\right)\right)\ d^N\mathbf{p}\ d^N\mathbf{q}, \tag{2.30}$$

where Θ is the step function, as defined for equation 2.27.

The Weyl formula can be equivalently stated in terms of $D_{AV}(E)$, the average density of states at an energy E.

$$D_{AV}(E) = \frac{1}{h^N} \int \delta\left(E - H\left(\mathbf{p}, \mathbf{q}\right)\right)\ d^N\mathbf{p}\ d^N\mathbf{q}, \tag{2.31}$$

where $\delta(x)$ is the Dirac delta function (the Dirac delta function is defined such that $\int_{-\infty}^{\infty} \kappa(x)\, \delta(x - x_0)\, dx = \kappa(x_0)$, where $\kappa(x)$ is some function of x.).

The reader is reminded that the Weyl formula describes the slow variation of $N(E)$ and $D(E)$ over large ranges of E. $N(E)$ and $D(E)$ also contain fluctuations over short ranges of E, which shall be discussed in the following section.

The Gutzwiller trace formula

As explained in the introduction to section 2.3.1, the density of states $D(E)$ can be expressed as rapid fluctuations superimposed on a slowly-varying background. The Gutzwiller trace formula [17, 19, 21, 22] relates the rapid fluctuations in the density of states to the classical dynamics. In short, it relates $D_{OS}(E)$ (see equation 2.29) to the classical dynamics.

The derivation of the Gutzwiller trace formula is very involved [17, 21] and shall not be reproduced here. It proceeds by relating the density of states to a quantity called the *Green's function*, which is useful tool in quantum and classical mechanics. The Green's function is then approximated via a summation of trajectories. The result is:

$$D_{OS}(E) = \frac{1}{\pi\hbar}\sum_j A_j e^{i(S_j(E)/\hbar+\phi_j)}. \qquad (2.32)$$

Equation 2.32 is a summation over periodic orbits, both stable and unstable. The index j labels each orbit. $S_j(E)$ is the action of the j^{th} orbit, A_j is a numerical coefficient which depends on the orbital period and stability, and ϕ_j is a phase factor which depends on the topology of the orbit.

The Gutzwiller trace formula can be interpreted as follows. Consider a Taylor expansion of the term in equation 2.32 for the j^{th} orbit about some energy E_0:

$$\frac{A_j}{\pi\hbar}e^{iS_j(E)/\hbar} \approx \frac{A_j}{\pi\hbar}e^{iS_j(E_0)/\hbar+i\frac{\partial S_j}{\partial E}(E-E_0)/\hbar}. \qquad (2.33)$$

Hence, using the result $\frac{\partial S}{\partial E} = T$ (see equation 2.15)

$$\frac{A_j}{\pi\hbar}e^{iS_j(E)/\hbar} \approx \frac{A_j}{\pi\hbar}e^{iS_j(E_0)/\hbar+iT_j(E-E_0)/\hbar}, \qquad (2.34)$$

where T_j is the period of the j^{th} orbit. Equation 2.34 shows that orbit j

produces periodic fluctuations in the density of levels. These fluctuations have a period δE_j given by:

$$\delta E_j \approx \frac{h}{T_j}\,. \tag{2.35}$$

These fluctuations are known as *Gutzwiller fluctuations.*

A more thorough examination of the Gutzwiller Trace formula reveals that the coefficients A_j are large for stable, or not very unstable, orbits. These tend to be the shortest, simplest orbits. Calculations for particular systems have demonstrated that the Gutzwiller fluctuations are indeed dominated by the shortest, simplest periodic orbits [19, 23].

It should also be noted that Gutzwiller fluctuations can be produced by so-called 'ghost' trajectories. Ghost trajectories [21, 24] are orbits that exist in a slightly different system. Imagine, for example, two very similar systems: system S and system S'. A particular classical orbit O may exist in S', but not in S. As the system parameters of S' approach those of S, the classical path O disappears abruptly, but the quantum mechanics changes smoothly. To be precise, the action of O acquires an imaginary component, so that the path contributes an exponentially decaying term to the Trace formula. Consequently, the effect of the path O can persist in the quantum mechanics even if it has disappeared from the classical analogue. Hence, it is known as a 'ghost' orbit.

2.3.2 Wavefunction scarring

This effect was first observed by Heller [23], when studying chaos in a billiard stadium. He observed that certain wavefunctions showed enhanced regions of probability density along an unstable classical path, and little probability density elsewhere. He named this effect *wavefunction scarring.* Scarred wavefunctions occur periodically in the energy level spectrum, with a separation of $\Delta E = \frac{h}{T}$, where T is the period of the unstable orbit. The reader will note that this energy level spacing is the same as the period of the fluctuations in the density of levels predicted by the Gutzwiller trace formula. In fact, wavefunction scarring and Gutzwiller fluctuations are closely related. They are both a consequence of the quantisation of periodic orbits. They are not found independently of each other.

The Correspondence Principle states that the predictions of quantum mechanics should converge towards the predictions of classical mechanics in the limit of high quantum numbers, when the spacing between energy levels is much less than the energy. This might lead the theorist to expect that, for large quantum numbers, the wavefunctions of systems with chaotic classical analogues should not be localised in one part of phase space, since a chaotic classical trajectory explores all of the available phase space. The theorist might imagine that the wavefunctions would have a smooth appearance, filling all available phase space and showing little structure. Berry [25] had proposed this idea before Heller's discovery, so scarring came as a surprise to the world of quantum chaos. However, scarring does not contradict the Correspondence Principle. Classical mechanics dictates that although an infinite number of unstable periodic orbits exist, they occupy an infinitesimally small volume of phase space. They are said to be *of zero measure.* In the same way, in the limit of high quantum numbers the enhancement of probability density along the scarring path (the *scar strength*) must tend to zero.

Generally, scarring is most prevalent for intermediate values of quantum number. If the quantum numbers are low, there may be insufficient numbers of antinodes in the wavefunction to effectively trace out a classical orbit. In the limit of high quantum numbers, the scar strength tends to zero, and the wavefunctions conform to Berry's conjecture. However, scarring has been shown to survive up to quantum numbers of over a million [26].

Heller supported his results by considering the propagation of a Gaussian wavepacket along a periodic orbit [23, 27]. This allowed him to estimate the modulations in the energy spectrum, and the scarring strength as a function of the stability of the orbit. Other theorists have also attempted calculations to substantiate the phenomenon of scarring. Bogomolny [28] considered the squared modulus of the wavefunction, averaged over a short range of energy and position. He then derived an expression for this "smoothed" wavefunction via a classical expression for the Green's function. His work confirmed that the scarring effect fluctuates in strength with the same periodicity predicted by the Gutzwiller formula. Berry [29] improved on this work by performing a similar calculation without averaging the wavefunction spatially.

2.3.3 Wigner functions

In classical mechanics, it is possible to define a distribution $f(\mathbf{p},\mathbf{q})$, such that $f(\mathbf{p},\mathbf{q})\; d\mathbf{p}\, d\mathbf{q}$ is the probability of the system having $\mathbf{p}$ and $\mathbf{q}$ values in the small phase space volume $d\mathbf{p}\, d\mathbf{q}$ around the phase space coordinates $(\mathbf{p},\mathbf{q})$. It would be useful to have a quantum mechanical equivalent for this function, so that the classical and quantum mechanical phase spaces could be compared. Unfortunately, it is impossible to define a true phase space probability distribution function for a quantum mechanical particle, because the Heisenberg uncertainty principle limits the detail in phase space to an area $\sim \frac{\hbar}{2}$. However, it is possible to define a phase space "quasiprobability" distribution function for a quantum-mechanical particle, which would resemble a phase space distribution function. Wigner attempted to find such a function, and derived the following result, which is known as the Wigner function [22, 30, 31].

$$W(\mathbf{p},\mathbf{q}) = \frac{1}{h^N}\int_{-\infty}^{\infty} \Psi^*\left(\mathbf{q}+\frac{\boldsymbol{\lambda}}{2}\right)\Psi\left(\mathbf{q}-\frac{\boldsymbol{\lambda}}{2}\right)e^{\frac{-i\mathbf{p}\cdot\boldsymbol{\lambda}}{\hbar}}\,d^N\lambda, \tag{2.36}$$

where N is the number of degrees-of-freedom, and $\boldsymbol{\lambda}$ is a position vector.

In short, the Wigner function is a quantum mechanical equivalent of a classical phase space plot. As for its classical equivalent, the Wigner function generally has too many dimensions to be easily represented or envisaged. So, theorists usually examine a particular plane of the Wigner function, and compare it to a corresponding Poincaré section.

Wigner faced several problems when he derived this function. The most fundamental is the limitations on the detail in phase space set by the Heisenberg uncertainty principle, as has been discussed already. Secondly, since he wanted to derive a phase space function from a wavefunction, he was forced to derive a function of $2N$ variables from a function of N variables. Consequently, he knew he would have some freedom to choose the form of his result. The Wigner function also has an additional problem which is not shared by quantum-mechanical distribution functions in general: it can be negative. How can the Wigner function be interpreted as a probability if it can have negative values?

In response to these objections, Wigner examined the properties of his function, and possible alternatives. He showed that integration of the Wigner function over all momentum space yields the square modulus of the wavefunction. In addition, he showed that the integration of the Wigner function over all real space yields the square modulus of the wavefunction in momentum space (i.e. the Fourier transform of the wavefunction). In fact, the integration of the Wigner function with any function of position or momentum over all momentum space and real space yields the correct quantum-mechanical expectation value of that function. He then proved that there is no function that satisfies these conditions *and* is always positive, which does not include more terms in Ψ. Hence, he chose the Wigner function as his phase space quasiprobability distribution function, as, in his words, *"it seems to be the simplest"*.

It is also worth noting Berry's work [32] on the form of the Wigner function in the classical limit (i.e. as $h \rightarrow 0$). He showed that for an integrable system, the Wigner function converges to a delta function on the corresponding classical torus in phase space. For the non-integrable case, he found that it was far more difficult to derive an *analytic* theory to describe the Wigner function in the classical limit. He proposed the use of numerical methods to investigate the Wigner functions for non-integrable systems.

Numerical studies to support the use of Wigner functions in the study of quantum chaos were first carried out by Hutchinson and Wyatt [33]. They studied the behaviour of the Wigner function, compared to the Poincaré section, during the transition to chaos. The Wigner functions and Poincaré sections showed close correlation. Dando and Monteiro [34] studied the Wigner functions of a quantum chaotic system in more depth. They compared the Wigner functions with the corresponding Poincaré section, and also with the corresponding Husimi function, which is a possible alternative quasiprobability function. They concluded that the Wigner functions reproduce the Poincaré sections with greater sharpness than the corresponding Husimi functions, and so are able to resolve more detail from the classical phase space.

Chapter 3

Bose-Einstein Condensation

3.1 Introduction

Imagine a collection of bosons (particles with integral spin) trapped in some kind of box or potential field. As the temperature is lowered, the bosons move into lower and lower quantum states of the container. Eventually, a macroscopic fraction of the bosons will enter the lowest quantum state of the system (the ground state). This phenomenon is called *Bose-Einstein condensation* [11, 35]. Bose-Einstein condensation is only possible for bosons, since the Pauli exclusion principle forbids fermions (particles with half-integral spin) to enter the same quantum state.

Bose-Einstein condensation occurs abruptly when the temperature drops below a certain value, known as the critical temperature. At this point there are discontinuities in thermodynamic quantities of the system (or their derivatives). Hence, Bose-Einstein condensation is considered to be a phase transition, and Bose-Einstein condensates (BECs) are regarded as a new state of matter. Bose-Einstein condensation in dilute gases was first achieved in 1995, using rubidium [36], lithium [37] and sodium [38].

Since Bose-Einstein condensation is essentially a relatively simple quantum mechanical concept, it may not surprise the reader that the basic theory was established many years ago. Nonetheless, it is remarkable to reflect that the theory began a full 70 years before the realisation of dilute gas BECs in 1995! In 1924, Bose wrote a paper [39] which discussed the statistics of photons, and sent it to Einstein for comments. Einstein recognised the significance of the paper, and extended the work to describe non-interacting massive bosons. He predicted that below a certain temperature, a finite fraction of the total number of particles would reside in the lowest energy single-particle state.

In 1938, Fritz London suggested that superfluid ^{4}He could be a manifestation of Bose-Einstein condensation [40]. His hypothesis was correct, and superfluid ^{4}He became the prototype BEC. However, superfluid ^{4}He differs from dilute gas BECs in the respect that there are strong interactions between helium atoms, with the result that the number of atoms in the zero-momentum state is reduced, even at absolute zero. Superconductors have been qualitatively modelled as Bose-Einstein condensates of electron pairs, which are known as Cooper pairs. However, the correspondence is not perfect, since the Cooper pairs break up above the critical temperature, whilst the atoms in a dilute gas BEC do not. Consequently, the properties of a superconductor are quantitatively very different to those of a corresponding dilute gas BEC.

When Bose-Einstein condensation occurs, the wavefunctions of the particles overlap. For this to occur, the de Broglie wavelengths of the particles must exceed the mean particle spacing. This condition can be satisfied by increasing the de Broglie wavelength and/or decreasing the inter-particle spacing. Both of the above criteria are, in principle, easily achievable experimentally by lowering the temperature and increasing the density respectively.

These ideas led experimentalists to attempt to realise a BEC from a gas of bosonic atoms. Unfortunately, a gas will normally liquefy or solidify at a far higher temperature than it Bose-Einstein condenses. Consequently, the experimentalists were forced to use gases of very low density (typically 10^{13}-10^{15} cm^{-3}). At low densities, three-body collisions are rare, and so the rate at which atoms clump together into clusters is slow. As a result, the gases can exist in a metastable state for a period of seconds or even minutes.

Since the experimentalists are forced to use gases of low density, the atomic de Broglie wavelengths have to be large to exceed the inter-atomic spacing. This means that the temperature has to be very low indeed. In fact, the required temperatures are less than a microkelvin. The technical challenges associated with achieving these extreme conditions are monumental, and it took 15 years of work to overcome them. The work culminated with the award of the 1997 Nobel prize in physics for the cooling and trapping techniques which made dilute gas BECs possible.

Bose-Einstein condensation of dilute gases was first achieved in June 1995 by a group at JILA in Boulder, Colorado, led by Eric Cornell and Carl Wieman [36]. They attempted to create a BEC from Rubidium-87 atoms. Alkali atoms are a popular choice since they have suitable spectra for laser cooling. Wieman and Cornell optically cooled the Rb gas in a magneto-optical trap (MOT), and then transferred the atoms into a magnetic time orbiting potential (TOP) trap for further evaporative cooling (see chapter 1 for a discussion of these techniques). In this way, they successfully created a BEC of a few thousand atoms, at densities of order 10^{12} cm^{-3} and temperatures of order 100nK.

This experiment was quickly followed by the work of Hulet's group at Rice university in Texas [37], and Ketterle's group at MIT in Massachusetts [38]. Hulet created a BEC of Lithium-7 atoms, while Ketterle chose sodium. Ketterle improved on the work of his predecessors by creating a BEC of 5×10^5 sodium atoms at densities in excess of 10^{14} cm^{-3}. Currently, dilute gas BECs typically contain a few thousand to several million atoms, at densities of 10^{13}-10^{15} cm^{-3}.

BECs are a manifestation of quantum mechanics on a large scale. They represent a unique experimental opportunity, since their remarkable dynamics can be imaged directly by optical means. Furthermore, they link many branches of physics, such as atomic physics, statistical physics and quantum optics.

This chapter discusses the statistical mechanics of BECs (section 3.2), the effect of interactions between the bosons (section 3.3), and how a condensate can be modelled theoretically (section 3.4). The author also includes an examination of the characteristic topological excitations of BECs, which shall be described in sections 3.5 and 3.6.

3.2 The transition temperature and condensate fraction

As was explained in the previous section, when Bose-Einstein condensation occurs the atomic wavepackets overlap. Hence, it is possible to derive an approximate expression for the transition temperature by equating the atomic wavelength λ with the mean atom spacing:

$$\lambda = n^{-\frac{1}{3}}, \tag{3.1}$$

where n is the atom density. (N.B. It is emphasised that this criterion is not a *definition* of Bose-Einstein condensation; it is a *consequence* of Bose-Einstein condensation.)

The quantity λ is equated to the thermal de Broglie wavelength, which is the thermal average wavelength of a free particle in a three-dimensional system. The thermal de Broglie wavelength is conventionally defined as

$$\lambda = \sqrt{\frac{2\pi\hbar^2}{mk_BT}}\,, \tag{3.2}$$

where m is the mass of each atom in the condensate. By substituting equation 3.2 into the condition 3.1, the following expression for the transition temperature T_c is obtained:

$$T_c = \frac{2\pi\hbar^2 n^{\frac{2}{3}}}{mk_B}\,. \tag{3.3}$$

In fact, a more rigorous calculation shows that equation 3.3 gives a value of T_c which is approximately double that of a uniform Bose gas in a box. The exact value of T_c is generally difficult to derive, since it depends on the shape of the box or confining potential, the number of atoms in the condensate and the strength of the interactions between the atoms. Nonetheless, equation 3.3 offers the theorist a “rough-and-ready” estimate of the transition temperature, which is accurate to within an order of magnitude, and also a qualitative understanding of the physics involved.

In order to derive a more accurate expression for the transition temperature, the theorist must consider the statistical mechanics of the problem. The following calculations concentrate on the case of a BEC in a harmonic-oscillator potential, since this form of atom trap is commonly used in experiment, and shall be the focus of this study. The potential energy of a three-dimensional anisotropic harmonic-oscillator has the following form:

$$V(x,y,z) = \frac{m}{2}\left(\omega_x^2 x^2 + \omega_y^2 y^2 + \omega_z^2 z^2\right). \tag{3.4}$$

The energy levels of such a potential are

$$E(n_x,n_y,n_z) = \left(n_x + \frac{1}{2}\right)\hbar\omega_x + \left(n_y + \frac{1}{2}\right)\hbar\omega_y + \left(n_z + \frac{1}{2}\right)\hbar\omega_z, \tag{3.5}$$

where the quantum numbers n_i have integer values greater than or equal to zero.

For energies that are large compared to $\hbar\omega_i$, the zero-point energy $\frac{\hbar\omega_i}{2}$ can be neglected, and n_i can be treated as a continuous variable. As a result of these approximations, it is useful to introduce a three-dimensional coordinate system with energy axes E_x, E_y and E_z, which are equal to $n_x\hbar\omega_x$, $n_y\hbar\omega_y$ and $n_z\hbar\omega_z$ respectively. Since n_i must be greater than or equal to zero, the theorist only considers the octant of this coordinate system for which $n_i \geq 0$.

The total energy of the oscillator E is equal to $E_x + E_y + E_z$, so a state with energy E must lie somewhere on the plane $E = E_x + E_y + E_z$. Each quantum state occupies a volume of $\hbar^3\omega_x\omega_y\omega_z$ in this coordinate space.

Now consider the volume $v(E)$ of E_x, E_y, E_z space containing states whose energy is less than the value E. This may be approximated by calculating the volume in the octant $n_i \geq 0$, enclosed by the plane $E = E_x + E_y + E_z$:

$$v(E) = \int_0^E \left[\int_0^{E-E_x}\left\{\int_0^{E-E_x-E_y} dE_z\right\} dE_y\right] dE_x. \tag{3.6}$$

The reader will now appreciate the reason for choosing this coordinate system. The value of $v\left(E\right)$ divided by the known volume occupied by each state yields the function $N\left(E\right)$, the approximate number of states below energy E. (This derivation is very similar to that used to obtain the Weyl formula in section 2.3.1.)

$$N\left(E\right)=\frac{1}{\hbar^{3}\omega_{x}\omega_{y}\omega_{z}}\int_{0}^{E}\left[\int_{0}^{E-E_{x}}\left\{\int_{0}^{E-E_{x}-E_{y}}dE_{z}\right\}dE_{y}\right]dE_{x}. \qquad (3.7)$$

The integrals in equation 3.7 can be easily evaluated, which leads to the result

$$N\left(E\right)=\frac{E^{3}}{6\hbar^{3}\omega_{x}\omega_{y}\omega_{z}}\,. \qquad (3.8)$$

The density of states at energy E, $D\left(E\right)$, is related to the function $N\left(E\right)$ by the general expression (see also equation 2.29):

$$D\left(E\right)=\frac{dN\left(E\right)}{dE}\,. \qquad (3.9)$$

Hence, the approximate density of states for a three dimensional harmonic-oscillator is determined by differentiating equation 3.8 with respect to energy:

$$D\left(E\right)=\frac{dN\left(E\right)}{dE}=\frac{E^{2}}{2\hbar^{3}\omega_{x}\omega_{y}\omega_{z}}\,. \qquad (3.10)$$

This example illustrates that, more generally, for a confining potential of arbitrary shape and dimension, the density of states is usually of the form:

$$D\left(E\right)=C_{\chi}E^{\chi-1}, \qquad (3.11)$$

where χ and C_{χ} are constants. In the example of a three-dimensional harmonic oscillator, $\chi=3$ and $C_{\chi}=\frac{1}{2\hbar^{3}\omega_{x}\omega_{y}\omega_{z}}$. This general form for the density of states will be used in the following calculations in order to derive a universal expression for T_c, and to illustrate how T_c depends on the form of the confining potential.

As was explained in the previous section, Bose-Einstein condensation can only occur for bosonic particles, since the Pauli exclusion principle forbids fermions to enter the same quantum state. The statistical mechanics of bosons are described by Bose-Einstein statistics. According to Bose-Einstein statistics, the average number of particles occupying a state n at an energy E_n is given by

$$N_n\left(E_n\right)=\frac{1}{e^{(E_n-\mu)/k_BT}-1}, \qquad (3.12)$$

where μ is the chemical potential [41]. It follows that the total number of particles in the system, N, is

$$N=\sum_n N_n\left(E_n\right)=\sum_n \frac{1}{e^{(E_n-\mu)/k_BT}-1}. \qquad (3.13)$$

As explained in the previous section, Bose-Einstein condensation occurs when a macroscopic fraction of the bosons enter the ground state (i.e. when the number of bosons in the ground state is of order N). However, at this stage of the discussion, it is more convenient to consider the number of particles in *excited* states N_{ex}, and use this to infer the number of particles in the ground state N_0. From equation 3.13, it follows that the number of bosons in excited states is given by:

$$N_{ex}=N-N_0=\sum_{n\neq 0} \frac{1}{e^{(E_n-\mu)/k_BT}-1}. \qquad (3.14)$$

This summation can be approximated by an integral [35]:

$$N_{ex}=N-N_0=\int_0^\infty \frac{dn}{e^{(E_n-\mu)/k_BT}-1}. \qquad (3.15)$$

It is more convenient to perform the integration in equation 3.15 over energy E rather than over the quantum number n. To do this, the zero-point energy is ignored, so that the ground state has energy $E_0 = 0$. This approximation is valid in the limit of a large number of particles N. The change of variable is carried out using the relation in equation 3.9:

$$N_{ex} = N - N_0 = \int_0^\infty \frac{D\left(E\right)\, dE}{e^{(E-\mu)/k_BT} - 1}\ . \tag{3.16}$$

The transition temperature T_c is now defined as the highest temperature at which the macroscopic (i.e. of the order of N) occupation of the lowest-energy state appears [11, 35]. This means that above T_c, all of the particles can be accommodated in excited states, but below T_c, at least some of the particles must be in the lowest-energy state. The highest temperature at which this transition can occur is attained when the chemical potential $\mu = E_0$ [11].

Now consider how μ varies with temperature. At high temperatures, $N_n\left(E_0\right) << 1$, hence from equation 3.12 $\mu << E_0$. As the temperature drops, $N_n\left(E_0\right)$ increases, and hence μ increases. However, μ cannot exceed E_0, or $N_n\left(E_0\right)$ would become negative, and hence unphysical. At the transition temperature, μ is equal to E_0, and remains equal to it if the gas is cooled to lower temperatures [11, 35].

The transition temperature is determined by satisfying the condition that all the particles are in excited states, i.e. $N = N_{ex}$. Below the transition temperature this can no longer be true. Since the ground state energy is set to zero in equation 3.16, the chemical potential is also set to zero [11].

Hence, at the transition temperature equation 3.16 becomes:

$$N = N_{ex} = \int_0^\infty \frac{D\left(E\right)\, dE}{e^{E/k_B T_c} - 1}\,. \tag{3.17}$$

The density of states $D\left(E\right)$ is now replaced by the general form given in equation 3.11. Equation 3.17 is then rewritten in term of the dimensionless variable $w = E/k_B T_c$:

$$N = C_\chi \left(k_B T_c\right)^\chi \int_0^\infty \frac{w^{\chi-1}\, dw}{e^w - 1}\,. \tag{3.18}$$

Equation 3.18 contains the standard integral

$$\int_0^\infty \frac{w^{\chi-1}\, dw}{e^w - 1} = \Gamma\left(\chi\right) \zeta\left(\chi\right), \tag{3.19}$$

where $\Gamma\left(\chi\right)$ is the gamma function and $\zeta\left(\chi\right)$ is the Reimann zeta function. Hence, it follows from equations 3.18 and 3.19 that:

$$T_c = \frac{N^{1/\chi}}{k_B \left[C_\chi \Gamma\left(\chi\right) \zeta\left(\chi\right)\right]^{1/\chi}}\,. \tag{3.20}$$

Equation 3.20 is now applied to the specific case of a condensate in a three-dimensional harmonic oscillator potential. For this potential, $\chi = 3$ and $C_\chi = \frac{1}{2\hbar^3 \omega_x \omega_y \omega_z}$ (see equation 3.10). Also, $\Gamma\left(3\right) = 2$ and $\zeta\left(3\right) \approx 1.202$. Hence, equation 3.20 can be simplified to the following useful form:

$$T_c \approx 4.5 \left(\frac{\bar{F}}{100}\right) N^{\frac{1}{3}} \text{ nK}, \tag{3.21}$$

where $\bar{F}$ is the geometric mean of the trap frequencies F_i in Hz. i.e.

$$\bar{F} = \left(F_x F_y F_z\right)^{\frac{1}{3}}. \tag{3.22}$$

A typical experiment might produce a condensate of 10^4 atoms in a trap of frequency 30 Hz in each axial direction [42]. According to equation 3.21, the transition temperature for such a condensate would be about 30 nK.

Now consider a uniform Bose gas in a three-dimensional box of volume V. In this case, $\chi = \frac{3}{2}$ and $C_\chi = \frac{V m^{\frac{3}{2}}}{\sqrt{2}\pi^2 \hbar^3}$ [11]. Also, $\Gamma\left(\frac{3}{2}\right) = \frac{\sqrt{\pi}}{2}$ and $\zeta\left(3\right) \approx 2.612$. Hence, equation 3.20 can be simplified to the following form:

$$T_c \approx 3.31 \frac{\hbar^2 n^{\frac{2}{3}}}{m k_B}\,, \tag{3.23}$$

which is approximately half the rough estimate of T_c in equation 3.3.

The reader should be aware that several approximations were made in the derivation of equation 3.20. Most importantly, the derivation assumes that the condensate contains an infinite number of particles, and consequently neglects the effects of the zero-point motion. In reality, there is a shift in the value of T_c as predicted by equation 3.20 because the number of particles in the condensate in finite. A calculation of this shift will not be included in this report. The finite-size correction tends to reduce T_c by a factor of order 1% [11, 35].

Below the transition temperature, the particles begin to drop into the lowest energy state. As the temperature decreases further, the number of particles in excited states becomes smaller and smaller. The fraction of particles in the lowest energy state is known as the condensate fraction [11, 35]. The condensate fraction can be derived by considering the number of particles in excited states as a function of temperature. An expression for this number has already been derived in equation 3.16, which is reproduced below:

$$N_{ex} = N - N_0 = \int_0^\infty \frac{D\left(E\right)\, dE}{e^{(E-\mu)/k_B T} - 1}\,. \tag{3.24}$$

As before, μ is set to zero and the density of states $D(E)$ is replaced by the general form given in equation 3.11. The equation is then rewritten in term of the dimensionless variable $w = E/k_B T_c$:

$$N_{ex} = C_\chi \left(k_B T\right)^\chi \int_0^\infty \frac{w^{\chi-1}\, dw}{e^w - 1} = C_\chi \left(k_B T\right)^\chi \Gamma\left(\chi\right) \zeta\left(\chi\right) \tag{3.25}$$

(using the standard result in equation 3.19). When $T = T_c$, $N_{ex} = N$, and so

$$N = C_\chi \left(k_B T_c\right)^\chi \Gamma\left(\chi\right) \zeta\left(\chi\right). \tag{3.26}$$

Dividing equation 3.25 by equation 3.26 gives

$$\frac{N_{ex}}{N} = \left(\frac{T}{T_c}\right)^\chi. \tag{3.27}$$

Hence, the number of particles in the condensate N_0 is:

$$N_0 = N - N_{ex} = N\left[1 - \left(\frac{T}{T_c}\right)^\chi\right]. \tag{3.28}$$

Again, the reader should be aware that approximations were made in the derivation of equation 3.28. Most importantly, it was assumed that the number of bosons is large, and that there are no interactions between them. When these effects are taken into account, there is a slight reduction in the condensate fraction as stated in equation 3.28 [35]. In fact, as a result of the interactions between the particles the condensate fraction is always < 1, even at absolute zero.

Below the transition temperature, the condensate appears as a sharp peak in the density of the atom cloud, superimposed on a broad background corresponding to excited bosons. As the temperature drops, the condensate fraction increases, and so the sharp peak becomes more pronounced. Similarly, the momentum distribution of the condensate is far narrower than that of the excited bosons. The sharp peaks in the density and momentum distributions are a signature of Bose-Einstein condensation [11, 35]. This is the principal piece of evidence with which experimentalists support their claim to have achieved Bose-Einstein condensation.

At the transition temperature, there are discontinuities in the thermodynamic properties of the Bose gas (or their derivatives). The precise nature of these discontinuities depends on the box or confining potential. For example, at the transition temperature there is a discontinuity in the specific heat of a Bose gas in a three-dimensional harmonic oscillator potential. These discontinuities demonstrate why Bose-Einstein condensation is considered to be a phase transition, and Bose-Einstein condensates are regarded as a new state of matter.

3.3 Interactions between atoms

The atom-atom interaction potential is, in general, a complicated function of the atomic separation. At low separations there is a strong repulsive core due to the overlapping of electron clouds. At large separations there is attraction due to the Van der Waals interaction. However, for the low densities and low temperatures associated with dilute gas BECs, the interatomic interactions can be characterised by a single parameter: the s-wave scattering length [11, 35, 43, 44].

At the densities characteristic of dilute gas BECs, three-body collisions are rare, and so the interatomic interactions can be modelled as two-body scattering events. The corresponding wavefunction ψ in the centre-of-mass frame is a sum of an incoming plane wave and an outgoing scattered wave, $\psi_{sc}(\mathbf{r})$. If the direction of travel of the incoming plane wave is defined to be the z-axis, then

$$\psi = e^{ikz} + \psi_{sc}\left(\mathbf{r}\right). \tag{3.29}$$

For large interatomic separations, the scattered wave is an outgoing spherical wave $f\left(\mathbf{k}\right)\frac{e^{ikr}}{r}$, where $f\left(\mathbf{k}\right)$ is the *scattering amplitude*, $\mathbf{k}$ is the wavevector of the scattered wave, and r is the radial distance from the scattering event. It is assumed that the interatomic interaction is spherically symmetric, and that the scattering amplitude depends only on the scattering angle β, which is the angle between z-axis and the direction of the scattered particle. For these approximations, equation 3.29 becomes:

$$\psi = e^{ikz} + f\left(\beta\right)\frac{e^{ikr}}{r}. \tag{3.30}$$

In dilute gas BECs, the de Broglie wavelength is large compared to the range of the interatomic forces, and the energy of the bosons is small compared with the mean atom-atom interaction potential. In this limit, only scattering of atoms in the zero orbital angular momentum state ($l = 0$) contributes to the total scattering amplitude [11, 43]. Scattering of particles in the $l = 0$ state is known as *s-wave scattering.* As a result, $f\left(\beta\right)$ approaches a constant value, denoted by $-a$, and the exact shape of the interatomic potential is unimportant. The parameter a is known as the *s-wave scattering length.* In the low energy limit, $k \to 0$, so the wavefunction ψ in equation 3.30 can be written

$$\psi = \left(1 - \frac{a}{r}\right). \tag{3.31}$$

By expanding the wavefunction ψ in terms of Legendre polynomials, it can be shown that the scattering cross-section σ in this low energy limit is [11, 43]

$$\sigma = 4\pi a^2. \tag{3.32}$$

This equation illustrates that the scattering length also determines the effective range of the interatomic potential. In fact, the effect of the interatomic potential is equivalent to that of a hard sphere of radius a. (Note that the quantum-mechanical cross-section given in equation 3.32 is four times the classical value in this low energy limit.)

The quantity a is used to characterise the effective average interactions within a dilute gas BEC, avoiding the need to consider the details of atomic scattering events. It can have either positive or negative values, which represent repulsive and attractive interactions respectively. Since the BEC is dilute, the interatomic spacing is large compared to the scattering length. Consequently, the s-wave scattering potential can be modelled as an effective zero-range potential [11, 35, 44]:

$$V\left(\mathbf{r}-\acute{\mathbf{r}}\right)=U_0\delta\left(\mathbf{r}-\acute{\mathbf{r}}\right), \tag{3.33}$$

where $\mathbf{r}$ and $\acute{\mathbf{r}}$ are the positions of two particular atoms, δ is the Dirac delta function (defined in section 2.3.1), and

$$U_0=\frac{4\pi\hbar^2 a}{m}\,. \tag{3.34}$$

This result is used to derive a quantum-mechanical model of the BEC in the following section.

In the derivation of equation 3.33, it was assumed that the scattering length is small compared to the interatomic spacing. This is a required condition for the BEC to be weakly interacting, or, equivalently, for the condensate fraction to be large. The reader will also recall that, in a BEC, the de Broglie wavelength is larger than the interatomic spacing. Hence, for weakly-interacting dilute gas BECs, the following inequality must be satisfied:

$$\lambda > n^{-\frac{1}{3}} >> a. \tag{3.35}$$

3.4 The Gross-Pitaevskii equation

In 1961, Gross and Pitaevskii independently derived a non-linear Schrödinger equation to describe BECs [45]. It uses a mean field approach to model the interactions between the bosons. Despite its simplicity, and the assumptions made in its derivation, it accurately (typically to within an error of a few per cent) reproduces the density and momentum profiles observed in BECs, and even their dynamics and excitations.

The derivation of the Gross-Pitaevskii equation assumes that all of the N bosons in the BEC occupy the same quantum state. Strictly, this is only true for non-interacting particles at zero temperature. At finite temperature, some bosons occupy excited states. The interactions cause a further reduction in the condensate fraction, which persists even at absolute zero. However, the assumption is approximately true for low temperatures and weak interactions[1].

If the N bosons all reside in the single-particle state ϖ, the wavefunction of the condensed state ψ can be written

$$\psi\left(\mathbf{r}\right) = N^{\frac{1}{2}}\varpi\left(\mathbf{r}\right), \tag{3.36}$$

where N is the number of bosons in the condensate. The single-particle wavefunction ϖ is normalised in the usual way:

$$\int \left|\varpi\left(\mathbf{r}\right)\right|^2 d\mathbf{r} = 1, \tag{3.37}$$

---

[1] Weak interactions are characterised by the condition that the scattering length is much less than the interparticle spacing.

which means that

$$\int |\psi(\mathbf{r})|^2 \, d\mathbf{r} = N. \tag{3.38}$$

Hence, $|\psi(\mathbf{r})|^2$ is interpreted as the number of atoms per unit volume, or simply the density of the condensate.

The effective many-body Hamiltonian of the condensate wavefunction is

$$H = \sum_{i=1}^{N} \left[\frac{\mathbf{p}_i^2}{2m} + V(\mathbf{r}_i) \right] + U_0 \sum_{i<j} \delta(\mathbf{r}_i - \mathbf{r}_j), \tag{3.39}$$

where

$$U_0 = \frac{4\pi\hbar^2 a}{m}. \tag{3.40}$$

The terms within the first summation are the familiar kinetic and potential energy terms ($V(\mathbf{r})$ being the external potential). The interactions are modelled by a zero-range potential, which was discussed in the previous section (see equation 3.33). The strength of the potential is characterised by the s-wave scattering length a. (The reader is reminded that this model of the interactions is valid in the limit of low energies and weak interactions.)

Proceeding from the many-body Hamiltonian, it is possible to derive an expression for the energy of the condensate wavefunction. The energy is then minimised with respect to variation of ψ in order to obtain the optimal form for ψ. This procedure yields the following Schrödinger equation [11, 35]

$$i\hbar \frac{\partial \psi(\mathbf{r})}{\partial t} = -\frac{\hbar^2}{2m} \nabla^2 \psi(\mathbf{r}) + V(\mathbf{r}) \psi(\mathbf{r}) + U_0 |\psi(\mathbf{r})|^2 \psi(\mathbf{r}). \tag{3.41}$$

Equation 3.41 is the time-dependent Gross-Pitaevskii equation [11, 35, 44, 45]. The first and the second terms on the right-hand side of the equation are respectively the usual kinetic and potential energy terms of an ordinary Schrödinger equation. The third term on the right-hand side of the equation is a mean field term which accounts for the interatomic interactions. It can be thought of as an additional potential term. Each particle feels this "additional potential" due to the mean field of all the other particles in the condensate. Given this interpretation, it is not surprising that the term is proportional to $|\psi(\mathbf{r})|^2$, namely the density of the condensate.

There is a corresponding time-*independent* Gross-Pitaevskii equation [11, 35], which describes static BECs:

$$\mu\psi(\mathbf{r}) = -\frac{\hbar^2}{2m}\nabla^2\psi(\mathbf{r}) + V(\mathbf{r})\psi(\mathbf{r}) + U_0|\psi(\mathbf{r})|^2\psi(\mathbf{r}). \tag{3.42}$$

Notice that the energy eigenvalue in equation 3.42 is the chemical potential, rather than the energy per particle as it is in the usual Schrödinger equation. The chemical potential is equal to the energy per particle for non-interacting particles in the same quantum state. However, the same is not true for interacting particles.

Due to the non-linear $|\psi(\mathbf{r})|^2$ term, it is difficult to solve the Gross-Pitaevskii equation analytically. It is only possible for very simple examples, such as the ground state of a BEC in a box with infinitely hard walls [45, 46]. However, these examples have illustrated some fundamental behaviour of BECs.

Consider, for example, a condensate in a potential which is zero for $x \geq 0$, and infinite for $x < 0$. Clearly, as x tends to zero from positive values the wavefunction ψ must also tend to zero, and must remain zero for all negative x. For large x, the wavefunction approaches some 'bulk' value. The distance over which the wavefunction grows from zero to the 'bulk' value is characterised by a length scale ξ.

The interaction term minimises its contribution to the energy of the wavefunction by spreading the atoms as widely as possible, and hence tends to reduce the value of ξ. The kinetic energy term minimises its contribution to the energy of the wavefunction by making $\nabla^2\psi(\mathbf{r})$ as small as possible, and hence tends to increase the value of ξ. The value of ξ is obtained by equating the interaction energy term and the kinetic energy term. The interaction energy term is of order nU_0, where n is the density. The kinetic energy term is of order $\frac{\hbar^2}{2m\xi^2}$. Equating these two values yields the result:

$$\frac{\hbar^2}{2m\xi^2} = nU_0, \tag{3.43}$$

which gives

$$\xi = \frac{1}{\sqrt{8\pi na}}\,. \tag{3.44}$$

The quantity ξ is known as the healing length [11, 35]. It is the characteristic length scale of fluctuations in the condensate density. It is of importance in the description of topological condensate excitations, as shall be discussed in sections 3.5 and 3.6.

Further results can be derived from the Gross-Pitaevskii equation. To proceed, multiply the time-dependent Gross-Pitaevskii equation (equation 3.41) by $\psi^*(\mathbf{r})$, and then subtract the complex conjugate of the resulting equation. This algebra yields

$$\frac{\partial|\psi|^2}{\partial t} + \nabla\cdot\left[\frac{\hbar}{2mi}\left(\psi^*\nabla\psi - \psi\nabla\psi^*\right)\right] = 0. \tag{3.45}$$

Equation 3.45 has the form of a continuity equation for particle density, given by

$$\frac{\partial n}{\partial t} + \nabla\cdot(n\mathbf{v}) = 0, \tag{3.46}$$

where $\mathbf{v}$ is the local velocity of the atoms in the condensate. By inspection of equations 3.45 and 3.46, $\mathbf{v}$ can be written

$$\mathbf{v} = \frac{\hbar}{2mi} \frac{\left(\psi^* \nabla \psi - \psi \nabla \psi^*\right)}{|\psi|^2} \,. \tag{3.47}$$

If the condensate wavefunction ψ is then written in terms of its amplitude and phase,

$$\psi = A e^{i\phi(\mathbf{r},t)}, \tag{3.48}$$

it follows from equation 3.47 that

$$\mathbf{v} = \frac{\hbar}{m} \nabla \phi \left(\mathbf{r}, t\right). \tag{3.49}$$

Equation 3.49 shows that the velocity of the condensate is proportional to the derivative of the condensate wavefunction phase [11, 35]. This result is important in the description of topological BEC excitations, as shall be discussed in sections 3.5 and 3.6.

3.5 Solitons

Solitons are topological excitations characteristic of BECs. They are localised disturbances in the atom density which travel through BECs without spreading, and generally behave like particles [11, 47, 48, 49]. Solitons propagate like waves, so they are also known as *solitary waves*.[2]

The form of solitons in BECs depends on the sign of the s-wave scattering length a. If a is positive (repulsive interactions), as is the case in this study, solitons are characterised by a local density minimum, and a sharp phase

---

[2] In the literature there is some controversy over the definition of the word soliton. In some cases, the definition requires that the disturbances exhibit special properties, which might include, for example, that they should repel at short range. However, usually collisional properties are not considered, and the terms soliton and solitary wave are taken to be synonymous [11, 48]. This convention shall be accepted in this study.

gradient of the wavefunction at the position of the minimum. These solitons are known as *dark solitons.* This category of solitons is further divided into *black solitons* and *grey solitons.* Black solitons have a density minimum of zero, and a sharp phase change of π at the position of the minimum (see figure 3.1). Grey solitons have a density minimum greater than zero, and a smoother phase change of modulus less than π at the position of the minimum. It will be shown later in this section that black solitons are stationary, and grey solitons are non-stationary. If a is negative (attractive interactions), solitons are characterised by a peak in the density, which has no associated phase jump. These solitons are known as *bright solitons.*

Solitons preserve their form because the interaction term in the Hamiltonian balances the dispersion (spreading) of the wavefunction caused by the kinetic energy term. Consider, for example, a dark soliton in a BEC in which the interactions are repulsive. The kinetic energy is related to the second derivative of the wavefunction, so it is minimised by smoothing out sharp fluctuations. This effect broadens the soliton. However, the repulsive interactions attempt to force particles into the minima, and hence narrow the soliton. For a particular soliton width, these two effects balance.

It is now clear why dark solitons occur in BECs which have repulsive interactions, and why bright solitons occur in BECs which have attractive interactions. In both cases the kinetic energy tends to broaden the soliton, and the interactions tend to narrow the soliton. This infers a density minimum if the interactions are repulsive, and a density maximum if the interactions are attractive.

The one-dimensional time-dependent Gross-Pitaevskii equation possesses stable soliton solutions. Consider the simple case of a single soliton propagating at a velocity v_x through an otherwise uniform BEC, for which the

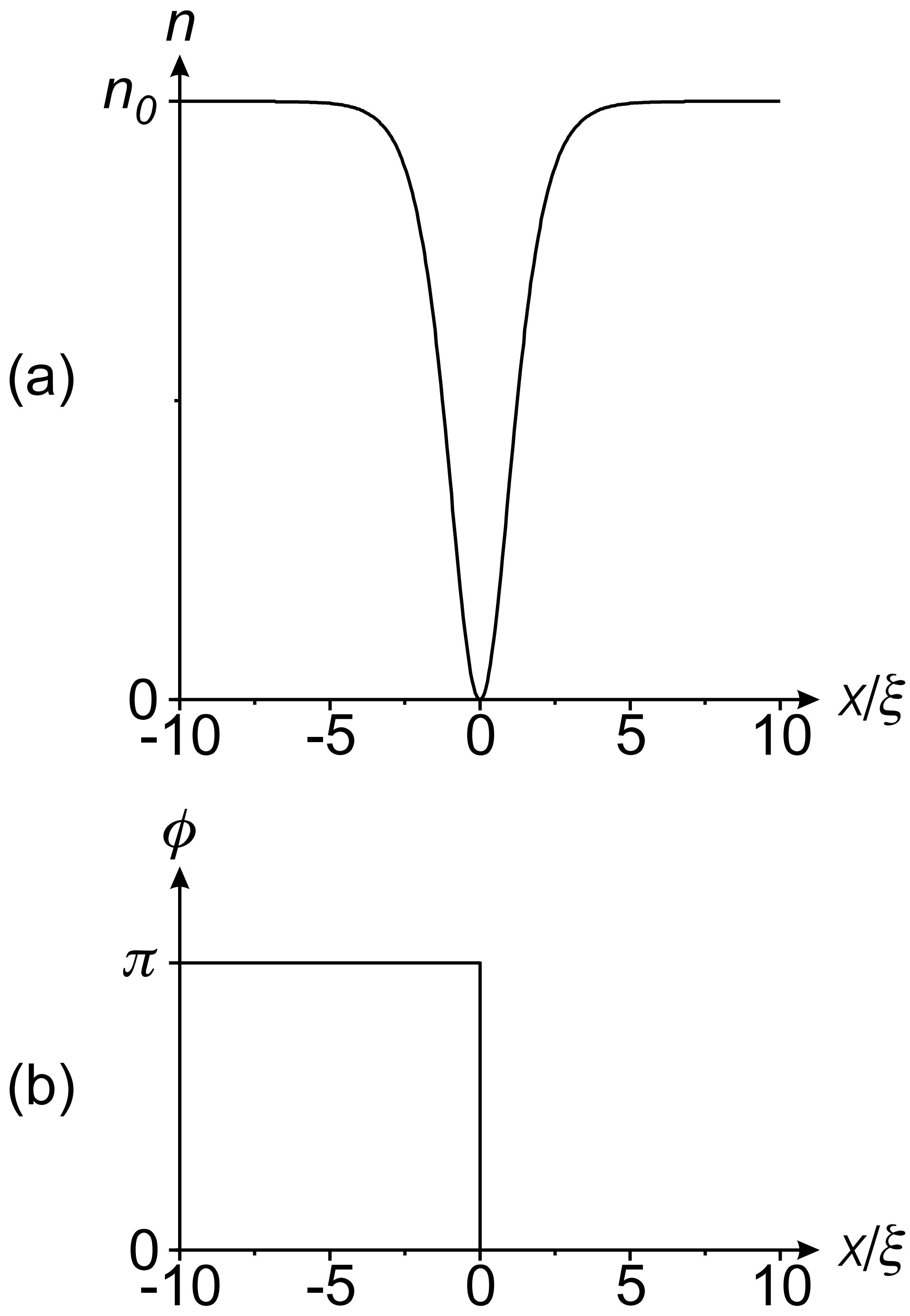

Figure 3.1: Density profile (a) and phase profile (b) of a black soliton. The position variable x is in units of healing length ξ. The constant n_0 denotes the bulk condensate density.

interactions are repulsive. As the spatial coordinate x approaches infinity or negative infinity, the condensate density n approaches a non-zero value n_0. The soliton does not change its shape, so x and the time t can only appear in the solution in the combination $x - v_x t$. Such a solution can be derived by means of the continuity equation (equation 3.46) [11]. When the boundary conditions $n \rightarrow n_0$ as $x \rightarrow \pm\infty$ are applied, the following expression for the condensate density can be obtained:

$$n\left(x,t\right) = n_{min} + \left(n_0 - n_{min}\right) \tanh^2 \left[\frac{x - v_x t}{\sqrt{2}\xi'}\right] , \tag{3.50}$$

where

$$\xi' = \frac{\xi}{\sqrt{1 - \left(\frac{v_x}{v_s}\right)^2}} , \tag{3.51}$$

in which

$$v_s = \sqrt{\frac{n_0 U_0}{m}} . \tag{3.52}$$

The quantity v_s is the velocity of sound in the uniform BEC. Note that equation 3.51 shows that the soliton speed v_x cannot exceed the speed of sound v_s.

Further algebra shows that there is a phase change Δ_ϕ between $x = \infty$ and $x = -\infty$. The relationship between Δ_ϕ, n_{min} and v_x is given below:

$$\frac{v_x}{v_s} = \cos\left(\frac{\Delta_\phi}{2}\right) = \frac{n_{min}}{n_0} . \tag{3.53}$$

Equation 3.50 describes a notch in the condensate density which travels without altering its shape or velocity. The density at the bottom of the notch is n_{min}, and the width of the notch is described by the parameter ξ'. When the soliton is stationary ($v_x = 0$), $\xi' = \xi$, $n_{min} = 0$ and $\Delta_\phi = \pi$. This means that the notch is narrow, its point reaches zero density, and it has a sharp π phase change across it. This is the description of a *black soliton*, which was defined earlier in this section (see also figure 3.1). Hence, the analysis demonstrates that black solitons are stationary. As the soliton's speed increases, it becomes wider and shallower, and the associated phase change becomes smaller and smoother (see equations 3.51 and 3.53). This is the description of a *grey soliton*, which was defined earlier in this section. Hence, the analysis demonstrates that grey solitons are non-stationary.

Studies of the motion of dark solitons have shown that they generally behave like particles [11, 50]. Unless they are subject to an external force, or they encounter fluctuations in condensate density, their acceleration remains zero (see equation 3.50). By considering the energy of the soliton, it is possible to derive an expression for the soliton's velocity in the presence of an external spatially-varying potential [11]. The result shows that the motion of solitons in an external potential is equivalent to the motion of a single particle of mass $2m$ in the same potential.

Although solitons are stable in model one-dimensional uniform systems at zero temperature, they are unstable in real three-dimensional systems. This is because the speed and shape of the soliton depends on the local speed of sound s, which is a function of the density n. Perturbations in the density of the condensate, or fluctuations in the density due to the confining potential, cause different parts of the soliton to move at different velocities. Hence the soliton bends (refracts), and eventually snaps into separate sections. This effect is known as the *snake instability* [49, 51]. It causes solitons to break up into more stable topological excitations, such as *vortex lines*, or *vortex rings*. These excitations shall be examined in the following section.

3.6 Vortices

Vortices, like solitons, are characteristic topological excitations of a BEC [11, 35, 49, 52, 53]; but, in contrast to solitons, they are stable in two and three dimensions. They can occur in various forms, such as *vortex lines* or *vortex rings*. Vortex formation has also been observed in superfluid Helium in response to rotation, and in superconductors in response to the application of a magnetic field. Vortices are a consequence of the existence of a macroscopic wavefunction, which describes the BEC.

The exact form of the vortex depends on the manner of its creation and on the dimensionality of the BEC. However, generally vortices appear as a line of zero density, around which condensate circulates. In short, they have the appearance of a whirlpool in a river. To understand the nature and origin of vortices, it is necessary to consider the phase of the condensate.

The condensate wavefunction is single-valued, i.e. at any point in space the wavefunction has just one particular value. Consequently, if the theorist imagines a closed loop in the BEC, which begins at a particular point and ends at that same point, the change in phase around the path must be an integer multiple of 2π. This is expressed mathematically as follows:

$$\Delta\phi = \oint \nabla\phi \cdot d\mathbf{l} = 2\pi q, \tag{3.54}$$

where ϕ is the phase, $\mathbf{l}$ is the positional coordinate on the loop and q is an integer. The *circulation* Λ around the closed loop is defined as

$$\Lambda = \oint \mathbf{v} \cdot d\mathbf{l}, \tag{3.55}$$

where $\mathbf{v}$ is the velocity. Using the relationship between $\mathbf{v}$ and ϕ given in equation 3.49, and the result in equation 3.54, it follows from equation 3.55 that:

$$\Lambda = \frac{\hbar}{m}\oint \nabla\phi \cdot d\mathrm{l} = \frac{\hbar}{m}2\pi q = q\frac{h}{m}\,. \tag{3.56}$$

This result shows that circulation in BECs is quantised in units of $\frac{h}{m}$.

Now imagine a BEC which contains one vortex. If the closed loop happens to enclose the vortex, then the circulation will be finite, and $|q| \geq 1$. The wavefunction corresponding to this example can be modelled most simply in cylindrical polar coordinates. If the vortex is defined to be at the position $\rho = 0$, the condensate wavefunction may be written as

$$\psi\left(\rho, \varphi, z\right) = A\left(\rho, z\right) e^{iq\varphi}. \tag{3.57}$$

The reader will observe that in following a closed path which encloses the line $\rho = 0$, φ must increase by 2π. Consequently, the phase change around such a path is $2\pi q$, and the circulation is $q\frac{h}{m}$.

In order to describe the velocity of the condensate around the vortex, the relationship between $\mathbf{v}$ and ϕ (equation 3.49) must be expressed in cylindrical polar coordinates. This has been done below for the specific case of the velocity in the $\boldsymbol{\varphi}$ direction:

$$v_\varphi = \frac{\hbar}{m}\frac{1}{\rho}\frac{\partial\phi}{\partial\varphi}\,. \tag{3.58}$$

For the wavefunction given in equation 3.57

$$v_\varphi = q\frac{h}{2\pi m\rho}\,. \tag{3.59}$$

Equation 3.59 explains the characteristic features of a vortex. It states that there is a constant velocity in the $\boldsymbol{\varphi}$ direction for a particular value of ρ.

This is the characteristic feature of condensate circulating around a vortex. The equation also shows that the velocity increases as ρ decreases. Hence, as $\rho \to 0$, the kinetic energy of bosons in the condensate tends to infinity. To avoid this problem, the density of the condensate must tend to zero as $\rho \to 0$ (i.e. if $|q| \geq 1$ then $A \to 0$ as $\rho \to 0$). This explains the characteristic feature of a zero in the density at the centre of a vortex.

Further conclusions can be drawn from equation 3.59. Using the classical expression for the angular momentum $\mathbf{L}$, namely,

$$\mathbf{L} = m\left(\mathbf{r} \times \mathbf{v}\right), \tag{3.60}$$

it follows from equation 3.59 that the angular momentum of each particle about the axis $\rho = 0$ is $q\hbar$. Hence, the total angular momentum about the axis $\rho = 0$ is $Nq\hbar$.

The Gross-Pitaevskii equation has solutions for BECs which contain vortices. If the wavefunction in equation 3.57 is substituted into the time-independent Gross-Pitaevskii equation (equation 3.42) in cylindrical polar coordinates, the following expression for $A\left(\rho, z\right)$ is obtained:

$$\left[-\frac{\hbar^2 \nabla^2}{2m} + \frac{\hbar^2 q^2}{2m\rho^2} + V\left(\rho, z\right) + U_0 A^2\left(\rho, z\right)\right] A\left(\rho, z\right) = \mu A\left(\rho, z\right). \tag{3.61}$$

Compare the above equation for the case of no vortex ($q = 0$) to the case of a single vortex at $\rho = 0$ ($|q| \geq 1$). The only difference between the two cases is that for $|q| \geq 1$, the equation contains an extra term in $\frac{1}{\rho^2}$. This term will become large as $\rho \to 0$, which confirms the earlier conclusion that if $|q| \geq 1$ then $A \to 0$ as $\rho \to 0$.

The length scale over which $A \to 0$ determines the typical size of a vortex. Let us suppose that the condensate is infinite, and that the potential is uniform. So, $V(\rho, z)$ is set to zero, and A tends to a constant value A_0 as $\rho \to \infty$. Given these conditions, equation 3.61 can be solved numerically. Unsurprisingly, the calculation reveals that $A \to 0$ on the scale of the healing length (see equation 3.44). Hence, the vortex is about two healing lengths wide.

In three-dimensional condensates, vortices appear as *vortex lines* or *vortex rings*. The example wavefunction in equation 3.57 describes a vortex line. A vortex line is so called because the core of the vortex lies on a line (the $\rho = 0$ line in the case of equation 3.57). A vortex ring is similar to a vortex line, but the core forms a closed loop rather than an open-ended line. Its form can be compared to that of a smoke ring.

The above discussion pertains to the general case of a vortex for which $|q| \geq 1$. In fact, vortices for which $|q| > 1$ are unstable, and a BEC preferentially forms multiple vortices rather than a large single vortex [45, 53].

Vortices have been produced in experiment by imparting angular momentum to the condensate by rotating an anisotropic trap [52, 53]. In this study, vortices are produced indirectly via the decay of dark solitons [49, 51].

Chapter 4

Classical and quantum mechanical descriptions of an atom in an optical lattice and a tilted harmonic trap

4.1 Introduction

As discussed in chapter 2, chaos is a classical idea, and can only be defined in classical terms. This leaves the physicist in some doubt as to what the term "quantum chaos" actually means. A more precise, but less concise name for this topic might be "the study of quantum systems with chaotic classical analogues." The "chaos" in quantum chaos is identified by comparing the quantum systems with their classical equivalents. Since optical lattices (OLs) can be used to investigate both classical energy band transport (see sections 1.2.1 and 1.3.5) *and* the corresponding quantised states, (Wannier-Stark ladders, see section 1.3.5), they are well-suited to experimental studies of the classical-quantum correspondence. Consequently, OLs are an ideal tool for exploring quantum chaos. OLs have already been used to realise the quantum δ-kicked rotor, which served as a model system for the study of quantum chaos for many years [21].

This chapter discusses an uncharged sodium atom moving in a one-dimensional OL, confined by a three-dimensional harmonic magnetic trap. Sodium was chosen because it has been manipulated in magnetic traps and OLs in recent experiments [7, 38]. See figure 4.1 for a schematic representation of the system. The magnetic trap can be tilted with respect to the OL, whose orientation is fixed. To describe this, the axis of the OL is defined to be the x-axis, and the symmetry axes of the magnetic trap are defined to be the x_t-axis and the z_t-axis. The angle between the principle axis of the magnetic trap (the x_t axis) and the axis of the OL (the x-axis) is defined as θ. The frequencies of the trap are sufficiently low for the trap to have a negligible effect on the band structure of the OL.

When one of the symmetry axes of the trap is aligned with the axis of the OL, i.e. $\theta = 0^\circ$ or 90°, the sodium atom follows regular classical paths. But tilting the symmetry axis away from these directions brings about a transition from stable regular motion to mixed stable-chaotic dynamics [54, 55]. The unique feature of this system is that the chaotic classical dynamics originate from an intrinsically quantum-mechanical property of the OL: the band structure. Similar dynamics have been reported for electrons in a semiconductor superlattice with a tilted magnetic field [56]. In both systems the one-dimensional lattice gives rise to an anisotropic and energy-dependent effective mass, which induces mixed stable-chaotic dynamics.

In this chapter, the system is examined using both quantum and semiclassical theory for various values of θ. The connections between classical and quantum-mechanical descriptions, as described in chapter 2, are explored.

The parameters chosen for this study have been used in experiments to

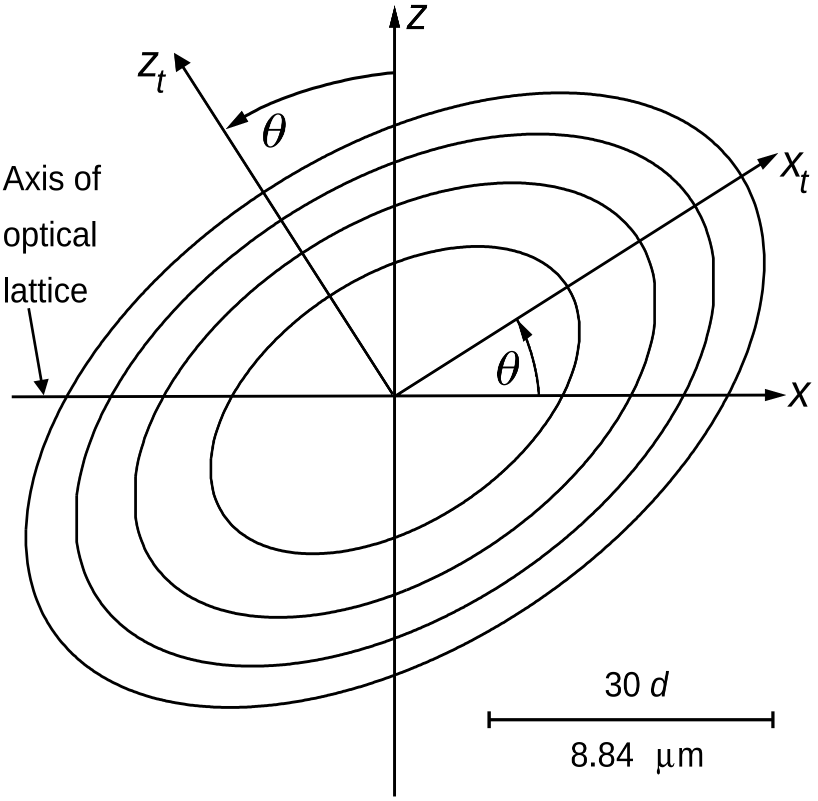

Figure 4.1: Schematic diagram showing orientation of the OL and tilted harmonic trap. Ellipses show contours of potential energy in the $x - z$ plane for a sodium atom confined by a harmonic trap with symmetry axes parallel to the x_t- and z_t-directions. The contours range from 10 to 40 peV at 10 peV intervals. The x_t-symmetry axis of the harmonic potential is tilted at an angle θ to the x-axis and laser field. Horizontal line indicates scale, where d is the spatial period of the OL.

detect Wannier-Stark ladders [7] (see also section 1.3.5), and to create Bose-Einstein condensates [38] (see also chapter 3). Similar parameters have been used to observe Bloch oscillations of cesium atoms in an optical lattice [5] (see also section 1.3.5). It is therefore emphasised that the effects discussed in this chapter should be accessible to experiment. The classical trajectories could be observed directly in a similar experiment to that used to detect the Bloch oscillations of cesium atoms [5]. Moreover, since the initial positions and velocities of the atoms are well defined and can be tailored at will, such experiments might also be able to map out Poincaré sections directly. In addition, it might be possible to investigate the quantised states in the lowest band by driving transitions to essentially free motion in higher bands [6, 7].

4.2 The quantum mechanics of the system

The potential energy of a sodium atom in the OL can be described by the following equation:

$$V_{\mathrm{OL}}(x) = V_0 \sin^2\left(\frac{\pi x}{d}\right). \tag{4.1}$$

For the system considered in this chapter, V_0 is 562.52 peV, and the OL period $d = \frac{\lambda}{2} = 294.5$ nm, where λ is the wavelength of the laser light. These OL parameters have been realised in recent experiments [7]. The form of $V_{\mathrm{OL}}(x)$ is shown in figure 4.2(a).

The potential energy of the sodium atom in the confining magnetic trap is:

$$V_{\mathrm{trap}}(x, y, z) = \frac{m}{2}\left(\omega_x^2 x_t^2 + \omega_y^2 y^2 + \omega_z^2 z_t^2\right), \tag{4.2}$$

where m is the mass of a single Na atom, and ω_x, ω_y and ω_z are the trap angular frequencies in the x_t, y and z_t directions respectively.

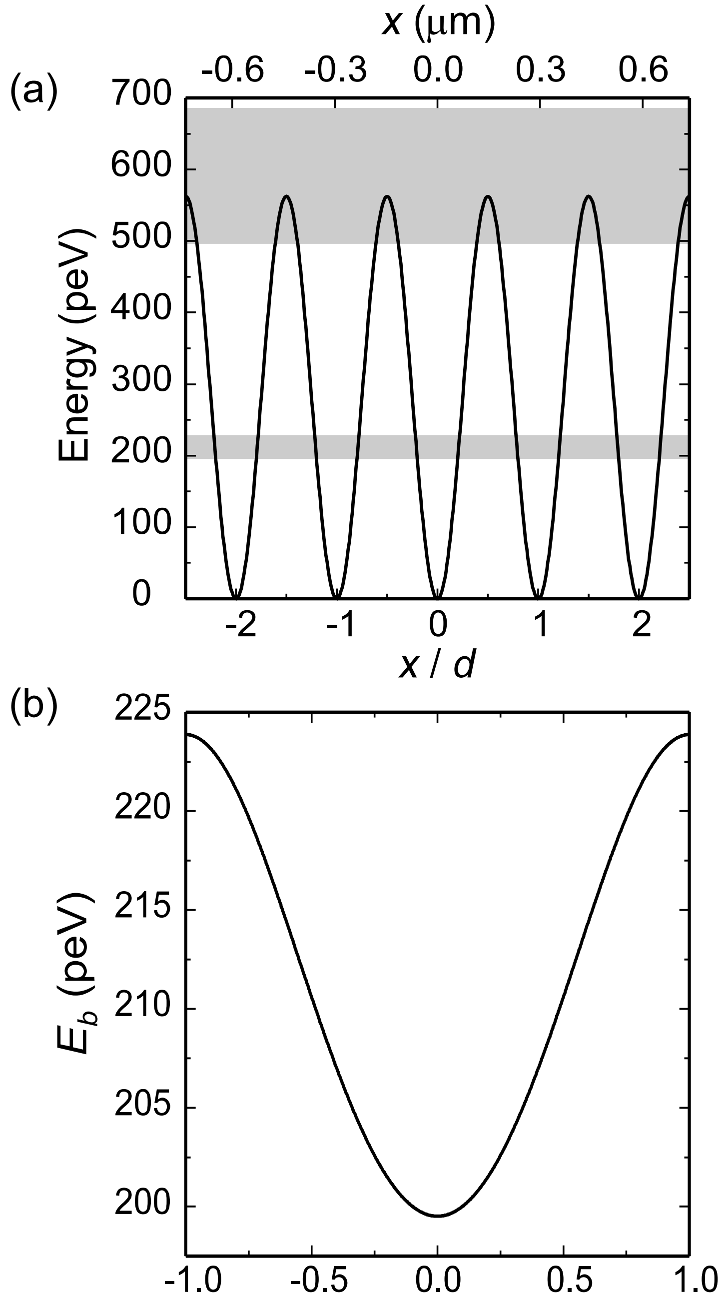

Figure 4.2: (a) Solid curve shows potential energy $V(x)$ of a sodium atom in the OL. Gray rectangles show energy ranges of the first and second energy bands of the OL. (b) $E_b(p_x)$ dispersion relation calculated for the first energy band, where $p_x = \hbar k_x$ is the crystal momentum corresponding to wavevector k_x.

Equipotentials of the harmonic trap in the x-z plane are shown in figure 4.1. The x_t- and z_t-axes correspond respectively to the x- and z- axes tilted through an angle θ, as shown in figure 4.1. The two sets of coordinates are related by

$$x_t = x\cos\theta + z\sin\theta \quad \text{and} \quad z_t = -x\sin\theta + z\cos\theta. \tag{4.3}$$

The angular frequencies were chosen such that the change in magnetic potential energy across one lattice period is much less than the width of the lowest energy band. This ensures that the band structure is not broken by the trap. The trap frequencies $\omega_x = 1479$ rad s^{-1}, $\omega_y = 4702$ rad s^{-1}, and $\omega_z = 2561$ rad s^{-1} are taken from experiments on sodium atoms in the $F = 1$, $m_F = -1$ state [38].[1]

The quantum-mechanical Hamiltonian for the system is

$$\hat{H} = \frac{\hat{p}_x^2}{2m} + \frac{\hat{p}_y^2}{2m} + \frac{\hat{p}_z^2}{2m} + \frac{m}{2}\left(\omega_x^2 x_t^2 + \omega_y^2 y^2 + \omega_z^2 z_t^2\right) + V_{\mathrm{OL}}(x), \tag{4.4}$$

where

$$\hat{p}_x = -i\hbar\frac{\partial}{\partial x}, \tag{4.5}$$

$$\hat{p}_y = -i\hbar\frac{\partial}{\partial y}, \tag{4.6}$$

and

$$\hat{p}_z = -i\hbar\frac{\partial}{\partial z} \tag{4.7}$$

are the momentum operators. The first three terms in equation 4.4 correspond to the kinetic energy of the sodium atom in the x, y and z directions

---

[1] This form of harmonic potential assumes that all of the atoms have the same magnetic sublevel m_F. If there is a mixture of sublevels, all of the atoms follow qualitatively similar classical paths, but the details of the phase space depend on m_F. See section 1.3.3 for a more detailed treatment of magnetic trapping.

respectively. The last two terms correspond to the potential energy due to the magnetic trap and OL.

The reader will notice that there are no coupling terms between y and the other coordinates. Consequently, the Hamiltonian can be written as the sum of an operator $\hat{H}_1$ in x and z, and an operator $\hat{H}_2$ in y, as shown below:

$$\left\{\hat{H}_1 + \hat{H}_2\right\} \Omega(x, y, z) = E_{x,y,z}\Omega(x, y, z), \tag{4.8}$$

where

$$\hat{H}_1 = \frac{\hat{p}_x^2}{2m} + \frac{\hat{p}_z^2}{2m} + \frac{m}{2}\left(\omega_x^2 x_t^2 + \omega_z^2 z_t^2\right) + V_{\mathrm{OL}}\left(x\right), \tag{4.9}$$

$$\hat{H}_2 = \frac{\hat{p}_y^2}{2m} + \frac{m}{2}\omega_y^2 y^2, \tag{4.10}$$

and $\Omega(x, y, z)$ is the eigenfunction corresponding the the eigenvalue of total energy $E_{x,y,z}$. This means that the motion in the y-direction can be separated from that in the x-z plane. Consequently, the wavefunction can be considered as a product of a function $\Psi(x, z)$ in x and z, and a function $\Xi(y)$ in y. This new form for the wavefunction is substituted into equation 4.8:

$$\left\{\hat{H}_1 + \hat{H}_2\right\} \Psi(x, z)\Xi(y) = E_{x,y,z}\Psi(x, z)\Xi(y). \tag{4.11}$$

Expanding the bracket gives

$$\hat{H}_1\Psi(x, z)\Xi(y) + \hat{H}_2\Psi(x, z)\Xi(y) = \left\{E_{x,z} + E_y\right\}\Psi(x, z)\Xi(y), \tag{4.12}$$

where $E_{x,z}$ is the energy associated with the motion in x- and z-directions, and E_y is the energy associated with the motion in the y-direction. (N.B. $E_{x,y,z} = E_{x,z} + E_y$.) By separating the variables, equation 4.12 can written as the two independent equations, 4.13 and 4.14:

$$\hat{H}_1\Psi(x,z) = E_{x,z}\Psi(x,z), \tag{4.13}$$

and

$$\hat{H}_2\Xi(y) = E_y\Xi(y). \tag{4.14}$$

Of these two equations, equation 4.13 is the most important. The solutions to equation 4.14 are simple harmonic oscillator states. From this point on, only equation 4.13 will be considered. The following sections discuss the two-dimensional energy eigenfunctions $\Psi(x,z)$ of the Hamiltonian operator $\hat{H}_1$, and then the equivalent semi-classical atom trajectories.

4.2.1 Analysis of the full quantum-mechanical Hamiltonian

The eigenfunctions of the Hamiltonian 4.9 are calculated by expressing them as a summation of basis states. Since the wavefunctions are two-dimensional, each basis state is the product of a function in x and a function in z. This is summarised in the equation below:

$$\Psi(x,z) = \sum_{r,n} c_{r,n} b_r(x) f_n(z). \tag{4.15}$$

Once the basis states have been chosen, the time-independent Schrödinger equation can be expressed as a matrix problem. This is solved by using standard routines to extract the eigenvalues and eigenvectors of the matrix. The eigenvalues correspond to the energy levels $E_{x,z}$ and the eigenvectors are the coefficients $c_{r,n}$, from which the wavefunctions can be constructed.

The most crucial difficulty is choosing a suitable basis set. Most importantly, the technique requires that the basis states are orthogonal. Furthermore, the number of required basis states, and thus the size of the matrix, is greatly reduced if the basis set is physically reasonable. In short, the basis states should 'look' like a small part of the wavefunction.

Simple harmonic oscillator (SHO) states were chosen as the functions $f_n\left(z\right)$, as they are exact eigenfunctions of the Hamiltonian if $\theta = 0$. The SHO states are given by [57]

$$f_n\left(z\right) = \left(\frac{m\omega_t}{\pi\hbar}\right)^{\frac{1}{4}} \frac{1}{\sqrt{2^n n!}} e^{-\frac{m\omega_t z^2}{2\hbar}} \acute{H}_n\left(z\sqrt{\frac{m\omega_t}{\hbar}}\right), \tag{4.16}$$

where

$$\omega_t = \sqrt{\omega_x^2 \sin^2\theta + \omega_z^2 \cos^2\theta} \tag{4.17}$$

and $\acute{H}_n$ is the $\mathrm{n^{th}}$ Hermite polynomial. On calculation of the matrix elements this choice of basis set is shown to be wise, since it results in the matrix being composed of just three bands. Consequently, the matrix can be stored in a compressed form, thus reducing demand on memory and computing time.

As for the functions $b_r\left(x\right)$, it would seem sensible to use eigenfunctions of the OL potential. However, these eigenfunctions are Bloch states, which are completely delocalised. Such functions would be awkward to use, and it is unclear how they should be normalised. Therefore, Wannier functions [58] were chosen to be the functions $b_r\left(x\right)$. Wannier functions are linear combinations of Bloch states, defined by [58]

$$b_r(x) = \frac{d}{2\pi}\int_{\frac{-\pi}{d}}^{\frac{\pi}{d}} e^{irkd}\Phi_k(x)\,dk, \tag{4.18}$$

where d is the period of the lattice, r is an integer specifying the index of the basis state, and $\Phi_k(x)$ is the Bloch state corresponding to wavenumber k in a particular band. (In this study the energies considered are not high enough to allow transitions into the second band. Hence, the functions $\Phi_k(x)$ are Bloch states of the first band of the OL.) In order to completely define the Wannier functions, it is necessary to specify the phase of the Bloch functions. The phase was adjusted to satisfy the following two conditions [58]:

(a) $\Phi_{-k}(x) = \Phi_k^*(x)$ This keeps the Wannier functions real.

(b) $\Phi_k(x)$ is real at the point where $|\Phi_k(x)|^2$ is largest.

Each Wannier function corresponds to a particular lattice period and a particular band. The Wannier function $b_r(x)$ is peaked sharply around the r^{th} well in $V_{\text{OL}}(x)$, and decays rapidly outside it (see figure 4.3). These properties make them particularly suitable for constructing a basis set, since they enable the theorist to control the spatial width of the wavefunction, and also which bands are mixed into it. Furthermore, the functions are physically reasonable, as they are strongly peaked in a lattice well. Finally, but most importantly, Wannier functions in different wells and/or in different bands are orthogonal [58].

In order to calculate the Wannier functions, it is first required to determine the Bloch states for the OL. These Bloch states satisfy the one-dimensional Schrödinger equation

$$\frac{-\hbar^2}{2m}\frac{d^2\Phi_k}{dx^2} + V_0 \sin^2\left(\frac{\pi x}{d}\right)\Phi_k = E_k\Phi_k, \tag{4.19}$$

where E_k is the eigenvalue corresponding to wavevector k. This equation can be reduced to the following form:

$$\frac{d^2\Phi_k}{dx^2} + \{g - 2q\cos(2\tilde{x})\}\,\Phi_k = 0, \tag{4.20}$$

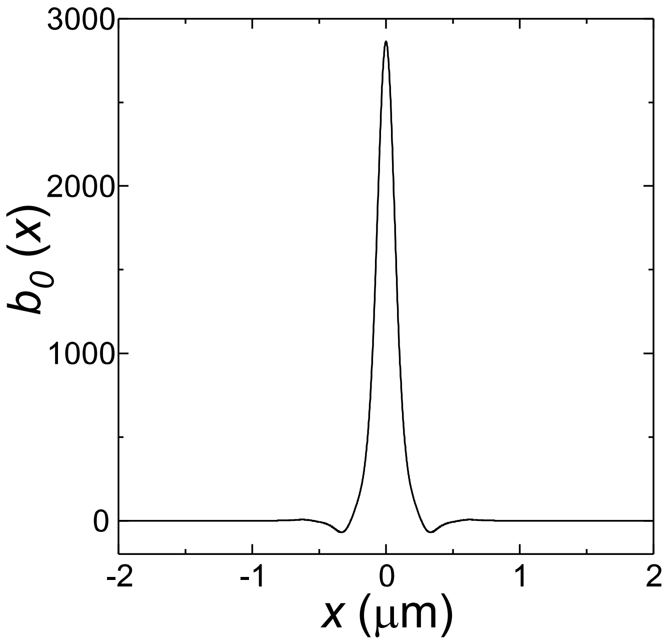

Figure 4.3: Wannier function b_0 as a function of x for the lowest band in the OL potential (equation 4.1).

where

$$g = \frac{2md^2}{\hbar^2\pi^2}\left(E_k - \frac{V_0}{2}\right), \tag{4.21}$$

$$q = -\frac{mV_0d^2}{2\pi^2\hbar^2}\,, \tag{4.22}$$

and

$$\tilde{x} = \frac{\pi x}{d}\,. \tag{4.23}$$

Equation 4.20 is a well known equation called Mathieu's equation [59], and its solutions are known as Mathieu functions. In this case, it is necessary to find Mathieu functions which satisfy Bloch's theorem (see section 1.2):

$$\Phi_k(x+d) = e^{ikd}\Phi_k(x), \tag{4.24}$$

or equivalently

$$\Phi_k(x) = u_k(x)e^{ikx}, \tag{4.25}$$

where $u_k(x)$ has the periodicity of the lattice. Equation 4.25 can be rewritten in terms of the variable $\tilde{x}$ in the following way:

$$F_\nu(\tilde{x}) = P_k(\tilde{x})e^{i\nu\tilde{x}}, \tag{4.26}$$

where $P_k(\tilde{x})$ has the periodicity π. The quantity ν is known as the characteristic exponent, and is related to the wavevector k by the following relationship:

$$\nu = \frac{kd}{\pi}\,. \tag{4.27}$$

The solutions which obey equation 4.26 are known as Floquet solutions [59]. They can be calculated using the following summation [59]:

$$F_\nu(\tilde{x}) = \sum_{j=-\infty}^{j=\infty} c_{2j}e^{i(\nu+2j)\tilde{x}}. \tag{4.28}$$

The coefficients c_{2j} are related by the following relationships:

$$G_m = \frac{c_m}{c_{m-2}} \qquad \text{for } m \geq 0, \tag{4.29}$$

and

$$H_{-m} = \frac{c_{-m-2}}{c_{-m}} \qquad \text{for } m \geq 0, \tag{4.30}$$

where

$$G_m = \frac{1}{V_m - \frac{1}{V_{m+2} - \frac{1}{V_{m+4} - \cdots}}}\,, \tag{4.31}$$

$$H_{-m} = \frac{1}{V_{-m-2} - \frac{1}{V_{-m-4} - \frac{1}{V_{-m-6} - \cdots}}}\,, \tag{4.32}$$

and

$$V_m = \frac{g - (m + \nu)^2}{q} . \tag{4.33}$$

(The variables g and q are defined in equations 4.21 and 4.22 respectively.)

Since g is a function of energy, the coefficients V_m cannot be calculated until the relationship between ν (i.e. k, the wavevector) and energy has been determined. That is to say, the dispersion relation must be calculated. This is done using the condition

$$H_0 G_0 = 1, \tag{4.34}$$

which follows from equations 4.29 and 4.30. The quantities H_0 and G_0 depend on both ν and E, through the relations 4.31, 4.32, 4.33 and 4.21. For each value of ν, a bracketing and bisection technique was used to find the value of energy for which equation 4.34 holds. This technique yielded the band structure $E_b\left(p_x\right)$, where $p_x = \hbar k_x$ shown in figure 4.2.

Once the dispersion relation is known, equations 4.29 to 4.33 can be used to determine the ratios of the coefficients c_m. Their values are then determined by setting c_0 arbitrarily to one. Finally, the Bloch functions are obtained using equations 4.28, 4.27 and 4.23, and normalised according to the following condition:

$$\int_0^d \left|\Phi_k(x)\right|^2 dx = 1. \tag{4.35}$$

The Wannier functions can now be calculated using equation 4.18.

Once the basis set has been determined, it is possible to substitute equation 4.15 into the time-independent Schrödinger equation to derive expressions for the elements of the Hamiltonian matrix. However, in order to proceed, the basis set and the Hamiltonian matrix must depend on the same set of coordinates. Unfortunately, the Hamiltonian (equation 4.9) presently contains terms in x_t and z_t. These must be expanded in terms of x and z. After simplification, the following Schrödinger equation is obtained:

$$\left\{\hat{H}_x + \hat{H}_z + \gamma x^2 + \eta xz\right\}\Psi(x,z) = E\Psi(x,z), \tag{4.36}$$

where

$$\hat{H}_x = -\frac{\hbar^2}{2m}\frac{\partial^2}{\partial x^2} + V_{\mathrm{OL}}(x), \tag{4.37}$$

$$\hat{H}_z = -\frac{\hbar^2}{2m}\frac{\partial^2}{\partial z^2} + \frac{m}{2}\left(\omega_x^2 \sin^2\theta + \omega_z^2 \cos^2\theta\right) z^2, \tag{4.38}$$

$$\gamma = \frac{m}{2}\left(\omega_x^2 \cos^2\theta + \omega_z^2 \sin^2\theta\right), \tag{4.39}$$

$$\eta = \frac{m}{2}\sin(2\theta)\left(\omega_x^2 - \omega_z^2\right), \tag{4.40}$$

and $E \equiv E_{x,z}$ is the energy associated with motion in the x-z plane (the subscripts have been omitted as E_y will not be considered again). The OL potential $V_{\mathrm{OL}}(x)$ is defined in equation 4.1.

The expansion of the eigenfunctions given in equation 4.15 is now easily substituted into equation 4.36. In order to produce a more useful expression, the resulting Schrödinger equation was multiplied through by the complex conjugate of a particular basis state, i.e. $b_{r'}^*(x)\, f_{n'}^*(z)$, and then integrated over all space. This procedure is shown in the following equation:

$$\begin{aligned}\int_{x,z} b_{r'}^*(x)\, f_{n'}^*(z)\left\{H_x + H_z + \gamma x^2 + \eta xz\right\}\sum_{r,n} c_{r,n} b_r(x) f_n(z)\, dx\, dz \\ = E\int_{x,z} b_{r'}^*(x)\, f_{n'}^*(z)\sum_{r,n} c_{r,n} b_r(x) f_n(z)\, dx\, dz.\end{aligned} \tag{4.41}$$

By making use of the orthogonality of the basis states, equation 4.41 can be reduced to the following expression:

$$\sum_r c_{r,n'} P^{r',r} + c_{r',n'} Q_n + \sum_r c_{r,n'-1} R_n^{r',r} + \sum_r c_{r,n'+1} S_n^{r',r} = E c_{r',n'}, \tag{4.42}$$

where

$$P^{r',r} = I_1^{r',r} + \gamma I_2^{r',r}, \tag{4.43}$$

$$Q_n = \left(n + \frac{1}{2}\right) \hbar \omega_t, \tag{4.44}$$

$$R_n^{r',r} = \eta \sqrt{\frac{\hbar}{2m\omega_t}} \sqrt{n+1} I_3^{r',r}, \tag{4.45}$$

and

$$S_n^{r',r} = \eta \sqrt{\frac{\hbar}{2m\omega_t}} \sqrt{n} I_3^{r',r}, \tag{4.46}$$

where

$$I_1^{r',r} = \int_x b_{r'}^* (x) H_x b_r (x) \ dx, \tag{4.47}$$

$$I_2^{r',r} = \int_x b_{r'}^* (x) x^2 b_r (x) \ dx, \tag{4.48}$$

$$I_3^{r',r} = \int_x b_{r'}^* (x) x b_r (x) \ dx, \tag{4.49}$$

and

$$\omega_t^2 = \omega_x^2 \sin^2 \theta + \omega_z^2 \cos^2 \theta. \tag{4.50}$$

Equation 4.42 can alternatively be expressed as a simple matrix problem:

$$\mathbf{H} \times \mathbf{C} = E\mathbf{C}, \tag{4.51}$$

where **H** is the Hamiltonian matrix and **C** is a matrix of basis state coefficients, corresponding to energy eigenvalue E. If the wavefunctions were composed of just four basis states in each axial direction, this matrix prob-

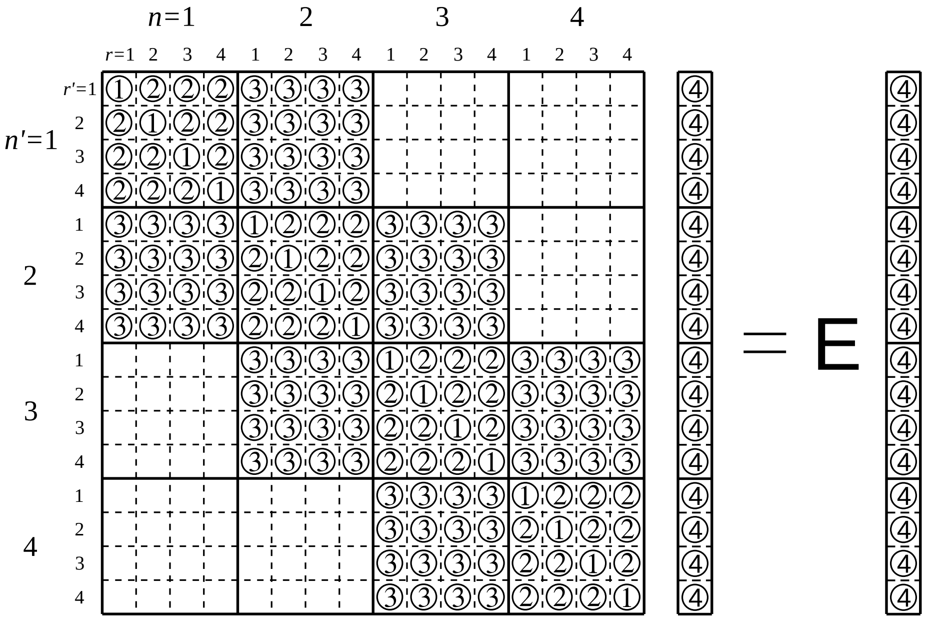

Figure 4.4: Schematic representation of the Hamiltonian matrix and the corresponding eigenvalue and eigenvector problem shown in equation 4.42. The matrix is drawn for a basis set of four wannier functions and four harmonic oscillator states. Elements labelled (1) are $P^{r',r} + Q_n$, those labelled (2) are $P^{r',r}$, those labelled (3) are $R_n^{r',r}$ or $S_n^{r',r}$, and those labelled (4) are $c_{r',n'}$. Since $R_n^{r',r} = S_{n+1}^{r,r'}$ (see text), the matrix is symmetric, and the elements $R_n^{r',r}$ and $S_n^{r',r}$ are denoted by the same label.

lem would be of the form shown in figure 4.4. N.B. By inspection of equations 4.45, 4.46 and 4.49, $R_n^{r',r} = S_{n+1}^{r,r'}$; hence the matrix is symmetric.

Equation 4.51 is a typical eigenvector and eigenvalue matrix problem, so standard routines [60] can be used to determine the values of **C** and E which satisfy it. The choice of basis states can now be seen to be wise, as a brief inspection of equation 4.42 and figure 4.4 reveals that **H** is banded, and sparsely populated by non-zero elements. Furthermore, since the matrix is symmetric, only the upper half above and including the leading diagonal needs to be calculated. Consequently, it can be stored in a compact format, and is more easily diagonalized.

In practice, about one hundred basis states were used in each axial direction. As a result, **H** was a square matrix of ten thousand rows and ten thousand columns, and **C** was a column matrix of ten thousand elements. The number of basis states was chosen as follows. The theorist guesses the required number of basis states, and solves the problem 4.51 for **C** and E. By inspection of matrix **C**, the theorist determines the value of $|c_{r,n}|$ for high values of r and n, compared to the largest value of $|c_{r,n}|$. If the ratio of these two numbers is 0.1% or less, then the number of basis states was deemed sufficient.

4.3 The semi-classical mechanics of the system

The band structure of the OL is a consequence of the translational symmetry of the OL, (see section 1.2.) This translational symmetry is broken by the magnetic trap, but the frequencies are sufficiently low such that it has a negligible effect on the band structure. Hence, it is valid to treat the trap potential as a perturbation of the optical potential. Time-dependent perturbation theory yields a very simple equation, which summarises the semi-classical mechanics [61] (see also section 1.2.1 which describes the semi-classical model of band transport):

$$\text{Force due to trap} = -\nabla V_{\text{trap}} = \hbar\dot{\mathbf{k}}. \tag{4.52}$$

where

$$V_{\text{trap}} = \frac{m}{2}\left(\omega_x^2 x_t^2 + \omega_z^2 z_t^2\right). \tag{4.53}$$

Equation 4.52 accounts for the laser potential via knowledge of the band structure. Hence the only force directly considered in the equation is that due to the magnetic trap.

The atom velocity $\mathbf{v}$ is related to the dispersion curve by the following relationship (see also equation 1.19):

$$\mathbf{v} = \frac{dE}{d\mathbf{p}} = \frac{1}{\hbar}\frac{\partial E\left(\mathbf{k}\right)}{\partial \mathbf{k}}\,, \tag{4.54}$$

where $\mathbf{p}$ is related to $\mathbf{k}$ by

$$\mathbf{p} = \left(p_x, p_z\right) = \hbar\mathbf{k} = \hbar\left(k_x, k_z\right). \tag{4.55}$$

The variable p_x is a crystal momentum, and the variable p_z is a true momentum.

The two semi-classical equations of motion 4.52 and 4.54 infer the effective classical Hamiltonian

$$H\left(x, z, p_x, p_z\right) = E_b\left(p_x\right) + \frac{p_z^2}{2m} + V_{\text{trap}}, \tag{4.56}$$

where $E_b\left(p_x\right)$ is the dispersion relation of the OL, and V_{trap} is as defined in equation 4.53.

By using equation 4.53, it is easy to substitute for V_{trap} in equation 4.52 and hence perform the differentiation to derive the following two equations of motion:

$$\frac{dp_x}{dt} = \hbar\frac{dk_x}{dt} = -m\omega_x^2 x_t \cos\theta + m\omega_z^2 z_t \sin\theta, \tag{4.57}$$

and

$$\frac{dp_z}{dt} = \hbar\frac{dk_z}{dt} = -m\omega_x^2 x_t \sin\theta - m\omega_z^2 z_t \cos\theta. \tag{4.58}$$

Equations 4.57 and 4.58, in conjunction with equation 4.54, determine the semi-classical paths of the atoms. In order to calculate the atom trajectories, equations 4.57 and 4.58 have to be numerically integrated. The method chosen was the fourth-order Runge-Kutta method [60].

The semi-classical trajectories were then used to plot Poincaré sections. These diagrams provide the theorist with an instant overview of the dynamics for particular energies and tilt angle θ, (see section 2.2.4). In this case, the diagrams were constructed by plotting a point on the z-p_z plane each time p_x passed through zero from positive p_x to negative p_x. A wide range of starting conditions, in terms of position and launch angle, was required to build up a complete picture of the dynamics.

4.3.1 Locating periodic orbits

An orbit is periodic if the atom returns to the same point in phase space after a period of time. Locating a periodic orbit, be it stable or unstable, involves searching phase space for a point that fulfills this condition. This is a computationally intensive process, not only because of the volume of phase space to be searched, but also because the atom's position in phase space must be checked after each time step to determine whether it has returned to its starting conditions. The technique chosen is known as the *downhill simplex method* by Nelder and Mead [60]. The technique works as follows.

To begin, a guess is made of the starting conditions for a periodic orbit. In this case, the starting conditions were defined in terms of a position on the Poincaré section, i.e. p_x was initially set to zero, and the coordinates z and p_z, which specify position on the Poincaré section, were considered to be the variables. In order to obtain the value of x corresponding to a particular position (z, p_z) on the Poincaré section, the atom energy is equated to the classical Hamiltonian (equation 4.56), i.e.

$$E = E_b\left(p_x\right) + \frac{p_z^2}{2m} + \frac{m}{2}\left(\omega_x^2 x_t^2 + \omega_z^2 z_t^2\right). \tag{4.59}$$

This equation is quadratic in x, so there are two possible values of x which satisfy it. Solving for x (see appendix A) yields

$$x = \frac{mz\cos\theta\sin\theta\left(\omega_z^2-\omega_x^2\right) \pm \sqrt{\frac{m}{2}\left(\omega_x^2\cos^2\theta+\omega_z^2\sin^2\theta\right)\left(E-E_b\left(0\right)-\frac{p_z^2}{2m}\right)}}{m\left(\omega_x^2\cos^2\theta+\omega_z^2\sin^2\theta\right)}. \tag{4.60}$$

(N.B. The term $E_b\left(p_x\right)$ has been replaced by $E_b\left(0\right)$ since $p_x = 0$ on the Poincaré surface of section.) Further algebra (see appendix A) reveals that, for the smaller value of x

$$\frac{dp_x}{dt} = \hbar\frac{dk_x}{dt} = \sqrt{\frac{m}{2}\left(\omega_x^2\cos^2\theta+\omega_z^2\sin^2\theta\right)\left(E-E_b\left(0\right)-\frac{p_z^2}{2m}\right)}\ , \tag{4.61}$$

and for the larger value of x

$$\frac{dp_x}{dt} = \hbar\frac{dk_x}{dt} = -\sqrt{\frac{m}{2}\left(\omega_x^2\cos^2\theta+\omega_z^2\sin^2\theta\right)\left(E-E_b\left(0\right)-\frac{p_z^2}{2m}\right)}\ . \tag{4.62}$$

Equations 4.61 and 4.62 show that the two possible values of x correspond to the two conditions $\frac{dp_x}{dt} > 0$ and $\frac{dp_x}{dt} < 0$. The value of x chosen was the latter, since this condition was used to construct the Poincaré sections.

Having determined the starting conditions, the atom is allowed to trace out its trajectory until it strikes the Poincaré section again. A measurement is made of the distance between the initial position on the Poincaré section, and the final position. This distance between the initial and final positions is considered to be a function (let us call it $\Upsilon(z, p_z)$) which depends on the starting conditions for the atom path. In order to find a periodic orbit, the variables z and p_z must be adjusted to minimise the function $\Upsilon(z, p_z)$ until it reaches zero.

The difficulty arises because the distance moved across the Poincaré section depends on two variables, z and p_z. Therefore, it is impossible to use a simple bracketing and bisection technique to find a minimum in $\Upsilon(z, p_z)$. Instead, a *simplex* is used. A *simplex* is a geometrical figure which moves in parameter space. In this case the simplex is a triangle, and it travels across the Poincaré section searching for minima in $\Upsilon(z, p_z)$. If it finds one, it contracts and slides into the minimum. The simplex continues to shrink until it has found the minimum to the desired accuracy.

The above explanation describes the method for finding simple periodic orbits which always strike the Poincaré section in the *same* place. However, it is possible to conceive of more complicated orbits, which strike the Poincaré section more than once before repeating themselves. In principle, separate searches have to be made for these longer orbits. However, the results in section 4.5 show that only the shortest, simplest orbits affect the energy level distribution and wavefunction patterns, as expected from the Gutzwiller trace formula (see section 2.3.1). Hence, searches for highly complicated orbits are not necessary.

4.4 Results for a trap tilt angle $\theta = 0°$

Setting θ to zero considerably simplifies the Schrödinger equation (equation 4.36) to

$$\left\{-\frac{\hbar^2}{2m}\frac{\partial^2}{\partial x^2} + \frac{m}{2}\omega_x^2 x^2 + V_{\mathrm{OL}}\left(x\right) - \frac{\hbar^2}{2m}\frac{\partial^2}{\partial z^2} + \frac{m}{2}\omega_z^2 z^2\right\}\Psi(x,z) = E\Psi(x,z). \tag{4.63}$$

The term which couples the motion in the x and z direction has disappeared, so the Hamiltonian can be written as the sum of a function in x and a function in z. The Hamiltonian is said to have become separable. This means that the wavefunction can be written simply as a product of a function in x, and a function in z. This is shown below:

$$\Psi(x,z) = r(x)s(z). \tag{4.64}$$

The function $r(x)$ satisfies

$$\left\{-\frac{\hbar^2}{2m}\frac{\partial^2}{\partial x^2} + \frac{m}{2}\omega_x^2 x^2 + V_{\mathrm{OL}}(x)\right\} r(x) = E_x r(x), \tag{4.65}$$

where E_x is the energy associated with motion in the x direction. The function $s(z)$ satisfies

$$\left\{-\frac{\hbar^2}{2m}\frac{\partial^2}{\partial z^2} + \frac{m}{2}\omega_z^2 z^2\right\} s(z) = E_z s(z), \tag{4.66}$$

where E_z is the energy associated with motion in the z direction. (N.B. $E = E_x + E_z$)

Since the Hamiltonian is separable, the dynamics in the x and z-directions are independent. There are no terms in the Hamiltonian which link the two directions, so no energy can be exchanged between them. Consequently, the energy in the x-direction and the energy in the z-direction are constants of the motion. Since there are two constants of the motion, and two degrees of freedom, the system is integrable. Hence, the motion for $\theta = 0$ cannot be chaotic.

In the z-direction, the sodium atom is a simple harmonic oscillator with frequency ω_z, (equation 4.66). In the x-direction, the sodium atom performs oscillations in a band, driven by the trap potential, (equation 4.65). This motion is clearly stable. Figure 4.5 shows a brief selection of the wavefunctions, all of which have a very regular appearance. The wavefunctions have been overlaid by periodic and quasi-periodic classical orbits to illustrate the correspondence between the two theories. The dashed ellipses enclose the classically allowed region for an atom of energy E, where E is the energy of the eigenstate; i.e. each ellipse corresponds to the trap equipotential $V_{\text{trap}}(x,z) = E - E_b(0)$. [2]

The stability of the system for $\theta = 0°$ is also illustrated by the Poincaré section, (figure 4.6(a)). The nested ellipses are slices through the tori of quasi-periodic orbits, and correspond to simple harmonic motion in the z-direction. The Poincaré section for $\theta = 90°$ (figure 4.6(f)) is very similar, and evidently also stable. This is because setting θ to $90°$ generates equations of exactly the same form as equation 4.63, the only difference being that the frequencies ω_x and ω_z are swapped. However, all the other Poincaré sections in figure 4.6 for intermediate trap tilt angles show more complicated behaviour. All of them contain concentric sets of points corresponding to quasi-periodic orbits, plus the apparently random, even distribution of points signifying chaotic dynamics. This regime of mixed stable-chaotic motion will now be considered in more detail.

4.5 Results for a trap tilt angle $\theta = 30°$

As θ is increased from $0°$, the regular, quasi-periodic orbits become distorted. Figure 4.7(a) shows a typical quasi-periodic orbit for $\theta = 0°$, and figure 4.7(b) shows a similar trajectory for $\theta = 30°$. At $\theta = 30°$, this type of trajectory is still quasi-periodic and stable, but now only occupies part of the phase space. Such trajectories produce the crescent-shaped stable

---

[2] The term $E_b(0)$ originates from the quantum confinement of the atom in each quantum well of the OL, and must be included in this expression since it represents the effective zero of energy for the semi-classical dynamics.

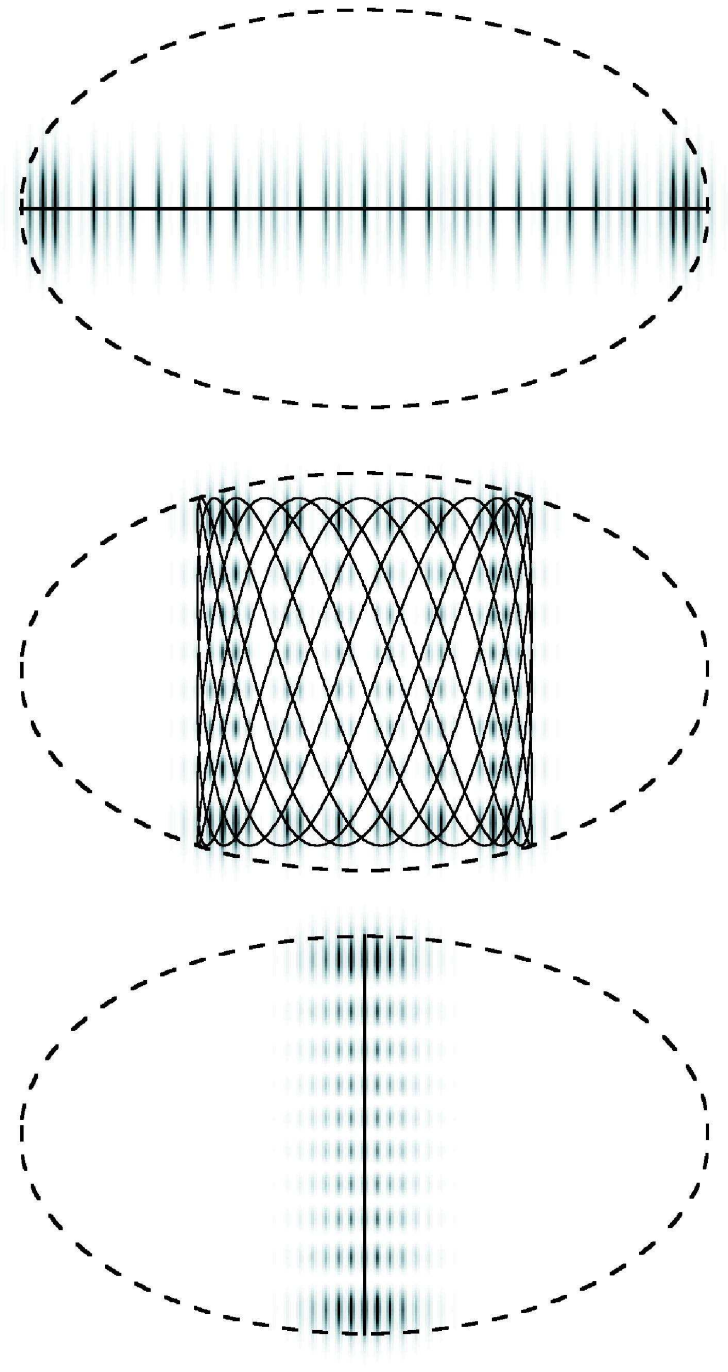

Figure 4.5: Energy eigenfunctions for $\theta = 0°$, overlaid by the corresponding classical orbits. The upper and lower wavefunctions are overlaid by periodic orbits, and the middle wavefunction is overlaid by a quasi-periodic orbit. The dashed ellipses enclose the classically allowed region for an atom of energy E (see text).

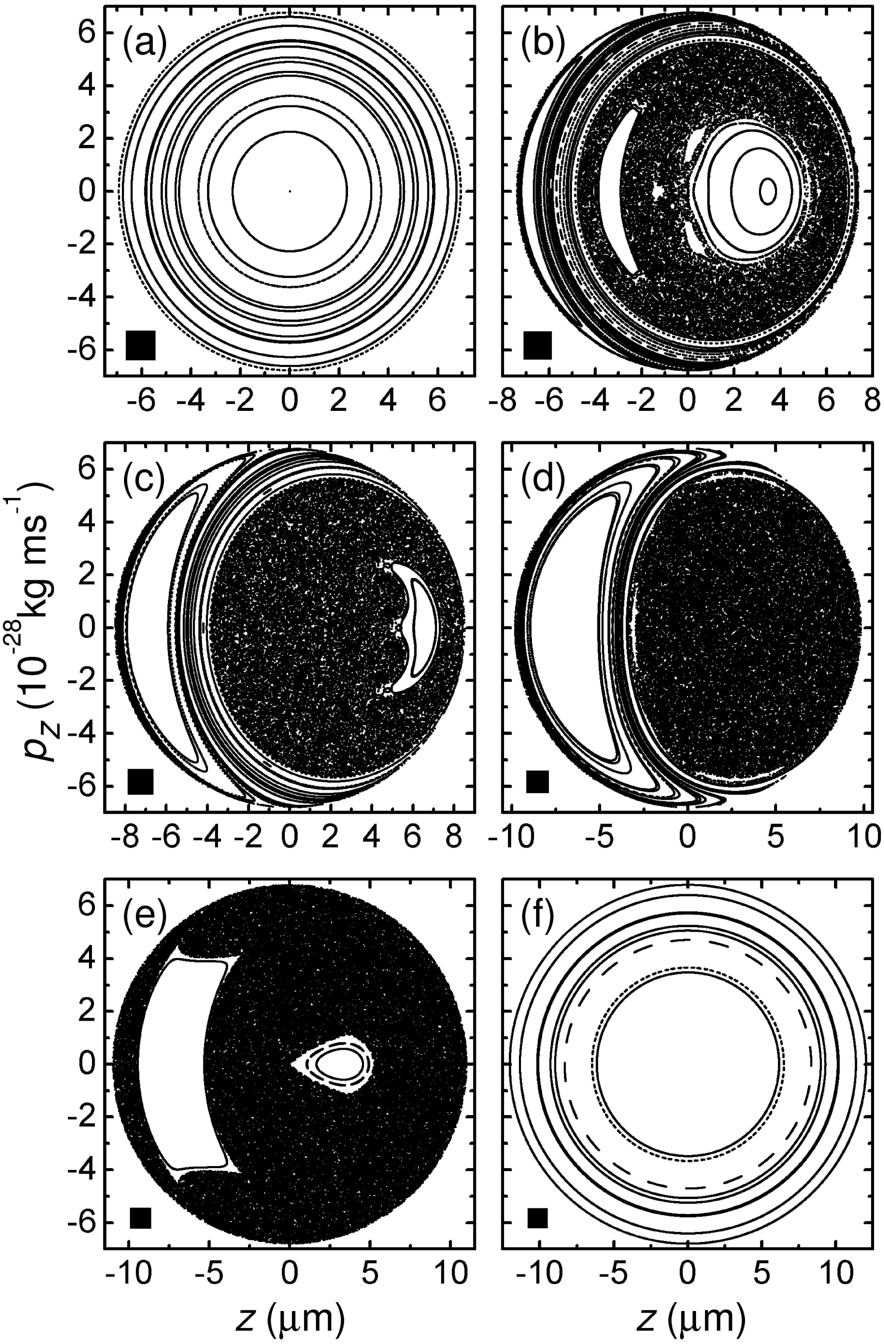

Figure 4.6: Poincaré sections in the (z, p_z) plane through the classical phase space calculated for atoms in the first energy band of the OL with $\theta = 0°$ (a), 15° (b), 30° (c), 45° (d), 60° (e), and 90° (f). Each section is constructed from 220 different trajectories with $E = 237.3$ peV. Areas of black squares equal $\hbar$.

islands towards the left hand sides of the Poincaré sections in figures 4.6(b) and 4.6(c), which correspond to $\theta = 15°$ and $30°$ respectively. Towards the right hand sides of figures 4.6(b) and 4.6(c) are regions of phase space which contain an apparently random, even distribution of points. These regions are indicative of chaotic behaviour, and are known as *chaotic seas.*

The chaotic region of the phase space grows quickly as θ increases from zero. It occupies a significant fraction of the phase space for $\theta = 15°$, (figure 4.6(b)), and is very well developed when θ reaches $30°$, (figure 4.6(c)). The highly irregular path of a typical chaotic trajectory is shown in figure 4.7(d). Periodic orbits do exist in the chaotic sea, and an example is shown in figure 4.7(c). These periodic orbits are extremely unstable, since an arbitrarily small change in the initial conditions causes the atom path to deviate rapidly from the periodic orbit, and thereafter follow a highly irregular path like that shown in figure 4.7(d).

The chaotic seas in figures 4.6(b) and 4.6(c) are enclosed by rings generated by stable quasi-periodic orbits. These rings are the remnants of the elliptical phase space structure at $\theta = 0°$ (figure 4.6(a)). The chaotic sea contains several additional stable islands, which gradually shrink and then vanish as θ increases.

When θ is increased to $45°$ (figure 4.6(d)), the stable islands within the chaotic sea disappear, and there are no longer any ring shaped islands surrounding the chaotic sea. Raising θ to $60°$ (figure 4.6(e)) increases the size of the chaotic sea, which now encloses all of the stable islands. As θ is increased beyond $60°$, these stable islands grow until they occupy the entire phase space when θ reaches $90°$ (figure 4.6(f)).

The mix of chaotic and stable behaviour in the classical phase space for a tilt angle of $30°$ is reflected in the nature of the quantum-mechanical results.

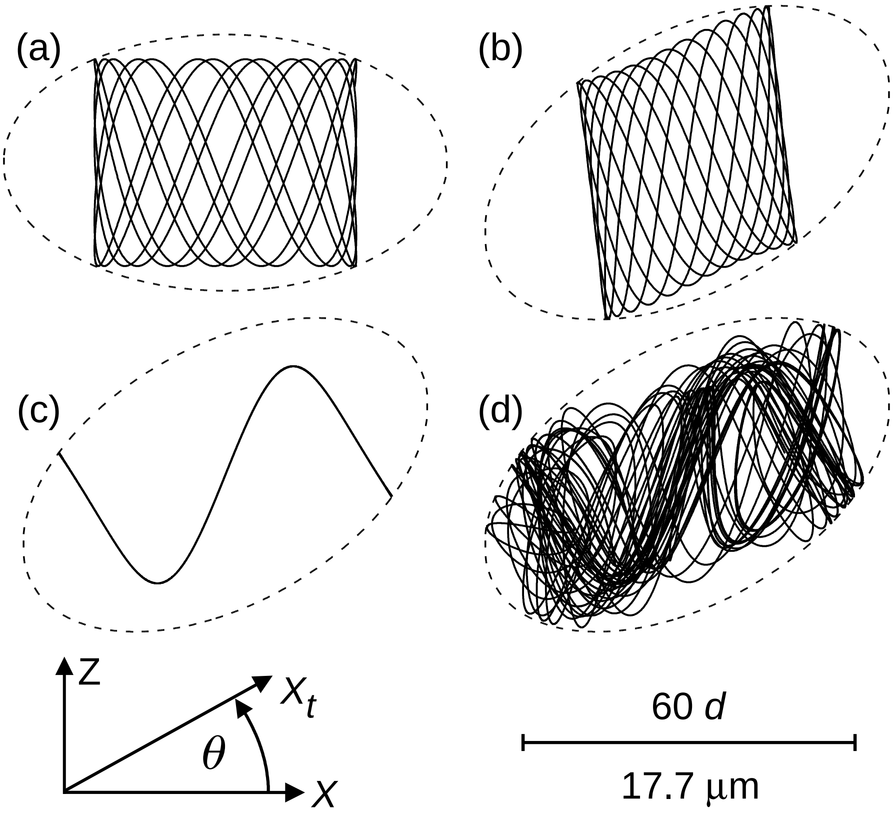

Figure 4.7: Classical orbits in the $x - z$ plane calculated for atoms in the first energy band of the OL with energy $E = 235.8$ peV and $\theta = 0°$ (a) and 30° (b)-(d). The dashed ellipses show the classically allowed locus for $E = 235.8$ peV. Orbits (c) and (d) both start from rest but with slightly different initial positions. Axes inset show orientation of symmetry axis x_t of the harmonic trap relative to the (x-) axis of the laser field. Horizontal line indicates scale.

Figures 4.8(a) and 4.8(b) show eigenfunctions for $\theta = 30^\circ$, which have a stable and a chaotic character respectively. A dashed ellipse has been included on both figures to indicate the classically allowed locus. Figure 4.8(a) has been overlaid by a semi-classical trajectory to illustrate the correspondence between the semi-classical and quantum-mechanical results.

Each wavefunction can be related directly to the classical phase space via its Wigner function [30, 34]. As described in section 2.3.3 (see equation 2.36), the Wigner function is defined as

$$W\left(\mathbf{p},\mathbf{q}\right) = \frac{1}{h^N}\int_{-\infty}^{\infty}\Psi^*\left(\mathbf{q}+\frac{\boldsymbol{\lambda}}{2}\right)\Psi\left(\mathbf{q}-\frac{\boldsymbol{\lambda}}{2}\right)e^{\frac{-i\mathbf{p}\cdot\boldsymbol{\lambda}}{\hbar}}\,d^N\lambda, \tag{4.67}$$

where $\boldsymbol{\lambda}$ is a position vector, and N is the number of degrees-of-freedom, which in this case is two. Setting $N = 2$ simplifies equation 4.67 to

$$\begin{aligned} W\left(x,z,p_x,p_z\right) = \frac{1}{\hbar^2}\int_{-\infty}^{\infty}\int_{-\infty}^{\infty}\Psi^*\left(x+\frac{\lambda_x}{2},z+\frac{\lambda_z}{2}\right)& \\ \Psi\left(x-\frac{\lambda_x}{2},z-\frac{\lambda_z}{2}\right)e^{-\frac{ip_x\lambda_x}{\hbar}}e^{-\frac{ip_z\lambda_z}{\hbar}}\,d\lambda_x d\lambda_z.& \end{aligned} \tag{4.68}$$

If the Wigner functions are to be directly comparable to the Poincaré sections (figure 4.6), they must be plotted on the same z-p_z plane in phase space. This means that p_x should be set to zero, as for the Poincaré sections. Setting p_x to zero for a particular pair of z-p_z coordinates implies two possible values of x for a particular semi-classical energy. These values of x are determined by equating the energy eigenvalue E to the classical Hamiltonian (equation 4.56), i.e.

$$E = E_b\left(p_x\right) + \frac{p_z^2}{2m} + \frac{m}{2}\left(\omega_x^2 x_t^2 + \omega_z^2 z_t^2\right). \tag{4.69}$$

This equation has already been solved for x (see equation 4.60 and ap-

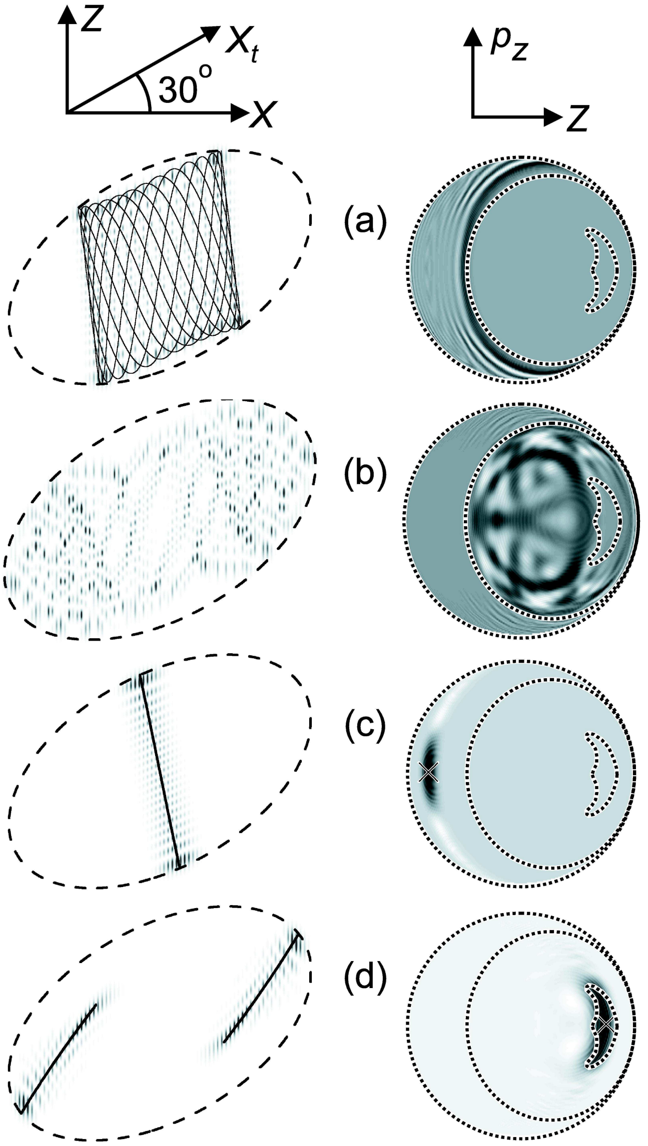

Figure 4.8: Left: probability density plots in the $x - z$ plane (coordinate axis shown top left) for eigenstates of the system with $\theta = 30°$ and (n, E_n) = (674, 235.8 peV) (a), (760, 238.0 peV) (b), (670, 235.7 peV) (c), (675, 235.9 peV) (d). The dashed ellipses denote the classically allowed locus. Classical paths associated with wavefunctions (a), (c) and (d) are overlaid. Right: the corresponding Wigner functions $W_n(z, p_z)$ (white << 0, gray = 0, black >> 0) with coordinate axes shown top right. The coordinate ranges of the Wigner functions are approximately -9μm $< z <$ 9μm and -7×10^{-28}kg ms^{-1} $< p_z <$ 7×10^{-28}kg ms^{-1}, as in figure 4.6(c). Crosses in (c) and (d) indicate the points where the classical orbits shown on the left of the figure strike the Poincaré section in figure 4.6(c).

pendix A). It was shown that the two possible values of x correspond to the two conditions $\frac{dp_x}{dt} > 0$ and $\frac{dp_x}{dt} < 0$ (see equations 4.61 and 4.62 and appendix A). In order to be consistent with the Poincaré sections, the Wigner functions were constructed using the latter value of x. Hence, the Wigner function $W(x, z, p_x, p_z)$ (equation 4.68) is reduced to a two-dimensional function of z and p_z, given by

$$W(z, p_z) = \frac{4}{\hbar^2} \int_0^\infty \int_0^\infty \Psi^* \left(x + \frac{\lambda_x}{2}, z + \frac{\lambda_z}{2} \right) \Psi \left(x - \frac{\lambda_x}{2}, z - \frac{\lambda_z}{2} \right) e^{-\frac{ip_z \lambda_z}{\hbar}} d\lambda_x d\lambda_z. \quad (4.70)$$

The two-dimensional Wigner functions corresponding to the the wavefunctions shown in figure 4.8 are shown to the right of the appropriate wavefunction. For ease of comparison, each Wigner function is overlaid with a dotted outline of the stable islands in the Poincaré section for $\theta = 30°$ (figure 4.6(c)). On comparison with the semi-classical phase space, the Wigner function in figure 4.8(a) is found to be concentrated in the large crescent-shaped stable island on the left-hand side of the Poincaré section. The Wigner function extends across all of the invariant curves within this stable region, suggesting that the wavefunction is associated with all of the stable orbits in this area of phase space, rather than a single path. Conversely, the Wigner function below (figure 4.8(b)) is concentrated in the chaotic sea of the Poincaré section. The extended nature of the Wigner function across the entire chaotic region shows that the wavefunction corresponds to aperiodic chaotic motion, which accounts for its complex, diffuse form.

Figure 4.8 also shows that some wavefunctions can be associated with particular periodic semi-classical orbits. The wavefunction in figure 4.8(c) is localised along the stable periodic orbit[3] (overlaid) that lies at the centre of the large crescent-shaped stable island on the left hand side of the Poincaré section (figure 4.6(c)). The corresponding Wigner function is shown to the right of the wavefunction. It is clearly peaked in the large stable region of the classical phase space. The point where the orbit strikes the Poincaré section is marked by a cross, which lies in the region of highest Wigner function amplitude.

The wavefunction in figure 4.8(d) is localised along the two overlaid stable periodic orbits (see footnote 3), which reflects the symmetry of the system under 180° rotation. The orbit on the right-hand side strikes the Poincaré section in the centre of the small stable island within the chaotic sea (figure 4.6(c)). The left-hand orbit does not strike the Poincaré section, since when $p_x = 0$ along this path, $\frac{dp_x}{dt} > 0$. At the outer turning point of these orbits, the atom paths are bounded by the dashed equipotential of the harmonic trap. But at the inner turning points, the motion is reversed by Bragg reflection at the edge of the first Brillouin zone. As before, a cross has been superimposed on the Wigner function to show where the orbit strikes the Poincaré section, and again it lies in the region of highest Wigner function amplitude.

Figure 4.9 shows five wavefunctions overlaid by another semi-classical periodic orbit. Consider initially the third wavefunction from the top. The wavefunction is concentrated around the overlaid S-shaped periodic orbit. In figure 4.10, the peak in the Wigner function (black region) again coincides with the point where the the orbit strikes the corresponding Poincaré section

---

[3] The wavefunction in figure 4.8(c) is a special case in which the probability density closely resembles the stable periodic orbit at the centre of the stable island in phase space. More generally, the wavefunctions associated with stable motion resemble orbits away from the centre of the stable island in phase space, and cannot be associated with a *single* stable periodic orbit (see, for example, figure 4.8(a)).

(marked by a cross). However, this example is different to those shown in figures 4.8(c) and (d) because the S-shaped orbit is unstable. Figure 4.10 confirms that S-shaped orbit strikes the Poincaré section within the chaotic sea. This is an example of *wavefunction scarring* (see section 2.3.2).

Wavefunctions which are localised around particular unstable but periodic orbits tend to appear regularly in the energy level spectra [23]. Theory predicts that such wavefunctions are spaced at energies of $\frac{h}{T}$, where T is the period of the orbit (see sections 2.3.1 and 2.3.2). This effect is illustrated for the *scarred* states shown in figure 4.9. The figure shows a sequence of five scarred states, overlaid by the S-shaped semi-classical orbit, alongside the energy level spectra. At the bottom of the figure an unscarred state is included for comparison. The position of the scarred states is marked by an elongated solid line in the spectra, which is connected to the corresponding wavefunction by a solid arrow. The line spectra shows that adjacent scarred states are separated by an energy of approximately 0.53 peV. This agrees with the predicted value of $\frac{h}{T_S}$, obtained from the orbit period $T_S = 7.8$ ms, to within 1%.

The energy level spectrum in figure 4.9 exhibits the complex, aperiodic distribution characteristic of nonintegrable systems. Despite this complexity, the sequences of scarred wavefunctions illustrate that there are profound links between the energy level spectrum and the semi-classical dynamics. The ideas discussed in section 2.3.1 are now applied to investigate the extent to which it is possible to relate the semi-classics to the energy level statistics.

The number of energy levels below an energy E is given by the staircase function

$$N(E) = \sum_n \Theta(E - E_n), \tag{4.71}$$

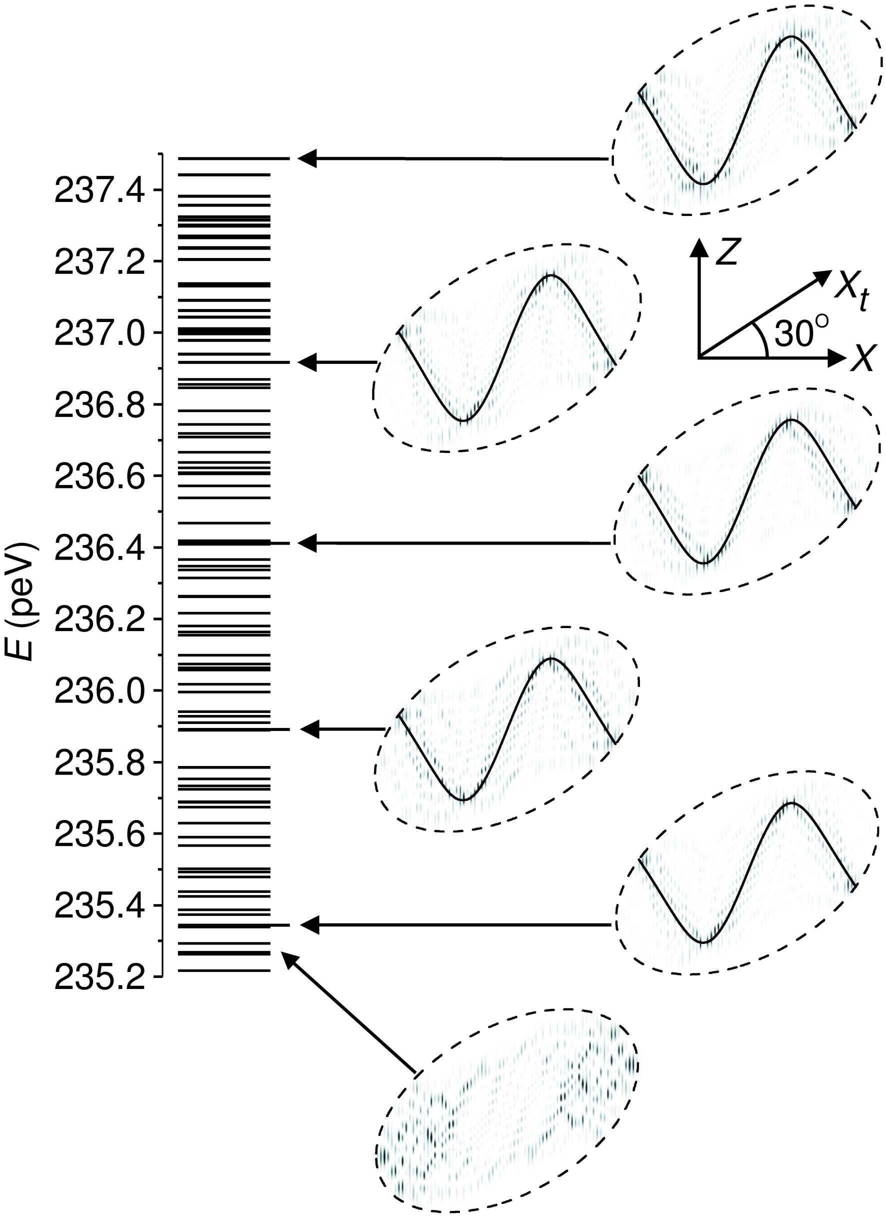

Figure 4.9: Horizontal lines: energy eigenvalues for $\theta = 30°$. Longer lines mark the energies of the scarred wavefunctions shown on the right of the figure (top five plots) with spatial axes inset. The S-shaped unstable periodic orbits (black curves) are overlaid on the probability density plots (white = 0, black = high) of each scarred wavefunction. The probability distribution of an unscarred wavefunction (bottom plot) is shown for comparison. In each wavefunction plot, the dashed ellipse shows the equipotential energy curve of the harmonic trap defined by $V(x, z) = E_n - E_b(0)$.

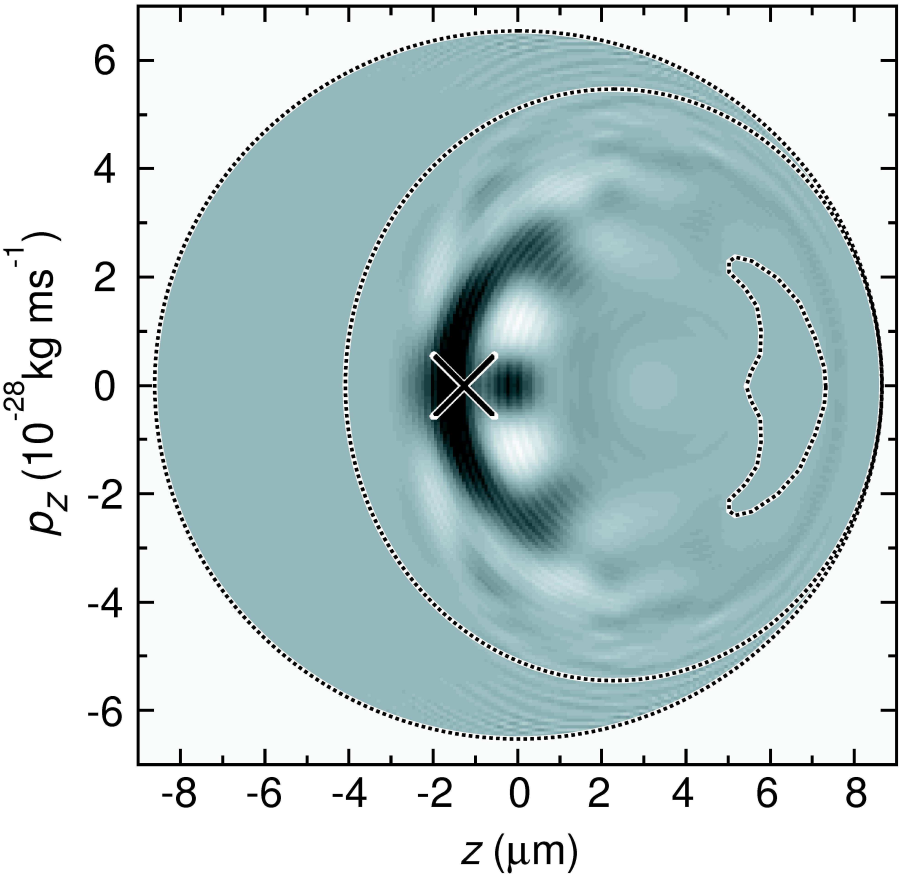

Figure 4.10: Wigner function $W_n\left(z,p_z\right)$ (white $<<0$, grey $=0$, black $>>0$) corresponding to the third scarred wavefunction from the top in figure 4.9. Cross indicates the point where the S-shaped scarring orbit crosses the $p_x=0$ plane with $\frac{dp_x}{dt}<0$. Dotted lines show the outlines of the stable islands in the corresponding mixed stable-chaotic phase space (which is shown in detail in figure 4.6(c)).

where $\Theta(E - E_n)$ is the step function of unit height (see section 2.3.1). The solid curve in figure 4.11(a) shows $N(E)$ for $N(E) \leq 20$ and $\theta = 30°$. The curve contains sudden steps, which originate from the energy quantization. However, this jagged structure is superimposed on a smoothly-varying background. Hence it is possible to consider the density of states as the sum of two terms: a slowly-varying, local average density of levels, $D_{AV}(E)$, and a rapidly-oscillating contribution, $D_{OS}(E)$. This idea is more fully explored in section 2.3.1, and is summarised in the equation

$$D(E) = D_{AV}(E) + D_{OS}(E) . \tag{4.72}$$

The slowly-varying contribution to the density of states can be linked to the semi-classics via the *Weyl formula.* The *Weyl formula* predicts a system's density of states by simply integrating over the available phase space at a particular energy, (see section 2.3.1). It is stated below for a two dimensional system:

$$D_{AV}(E) = \frac{1}{h^2} \int \delta\left\{E - H(x, z, p_x, p_z)\right\} dx\, dz\, dp_x\, dp_z, \tag{4.73}$$

where δ is the Dirac delta function.

A difficulty arises since the Hamiltonian for this system is most conveniently expressed in terms of the tilted spatial coordinates x_t and z_t, (see equation 4.9). However, the integrals with respect to x_t and z_t can be related to those with respect to x and z by

$$\int \delta\left\{E - H(x_t, z_t, p_x, p_z)\right\} dx_t\, dz_t\, dp_x\, dp_z = \int \delta\left\{E - H(x, z, p_x, p_z)\right\} |\mathbf{J}|\, dx\, dz\, dp_x\, dp_z, \tag{4.74}$$

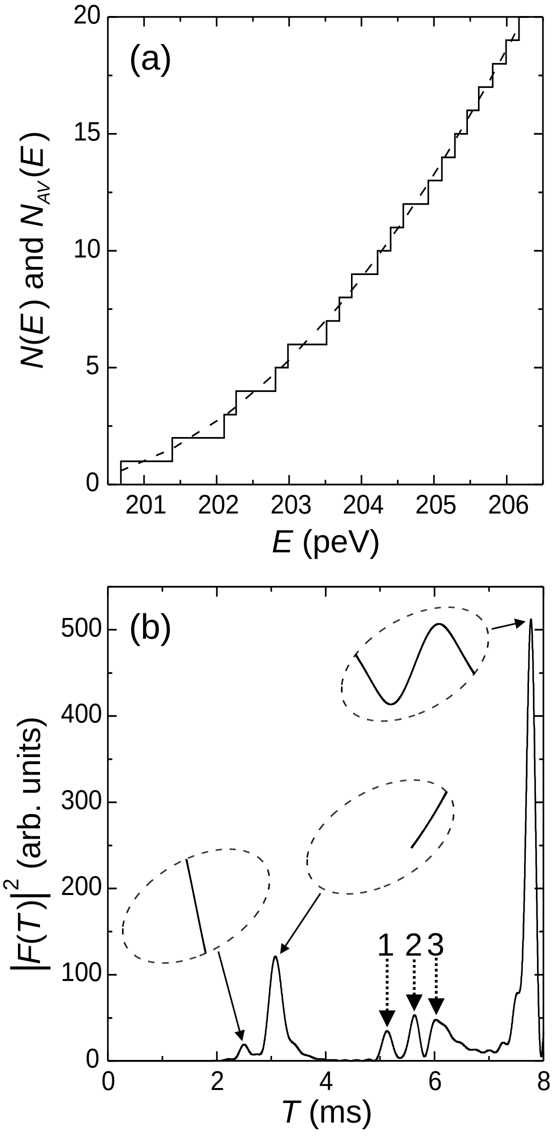

Figure 4.11: (a) $N(E)$ (solid curve) and $N_{AV}(E)$ (dashed curve) plots calculated for $\theta = 30°$. (b) Fourier power spectrum of $D_{OS}(E)$ in the range 224.6 peV $\leq E \leq$ 247.1 peV, shown as function of time T. Inset: periodic atom orbits corresponding to the peaks marked by solid arrows. Ellipses show the equipotential energy curve of the harmonic trap defined by $V(x, z) = E - E_b(0)$, with $E = 237.3$ peV. The origin of peaks 1-3 (dotted arrows) is described in the text.

where $|\mathbf{J}|$ is the determinant of the Jacobian matrix

$$\mathbf{J} = \begin{pmatrix} \frac{\partial x_t}{\partial x} & \frac{\partial x_t}{\partial z} \\ \frac{\partial z_t}{\partial x} & \frac{\partial z_t}{\partial z} \end{pmatrix}. \tag{4.75}$$

By making the appropriate substitutions using equation 4.3, the determinant of the Jacobian can be evaluated as shown below:

$$|\mathbf{J}| = \begin{vmatrix} \cos\theta & \sin\theta \\ -\sin\theta & \cos\theta \end{vmatrix} = \left|\cos^2\theta + \sin^2\theta\right| = 1. \tag{4.76}$$

This means that the integral with respect to x_t and z_t is equivalent to the integral with respect to x and z. Hence, equation 4.73 can be rewritten as

$$D_{AV}\left(E\right) = \frac{1}{h^2}\int \delta\left\{E - H\left(x_t, z_t, p_x, p_z\right)\right\} dx_t\, dz_t\, dp_x\, dp_z. \tag{4.77}$$

The semi-classical Hamiltonian (equation 4.56) is now substituted for H so the integration can be performed.

$$\begin{aligned} D_{AV}\left(E\right) = \frac{1}{h^2}\int_{p_z}\int_{p_x}\int_{z_t}\int_{x_t} \\ \delta\left\{E - E_b\left(p_x\right) - \frac{p_z^2}{2m} - \frac{1}{2}m\omega_x^2 x_t^2 - \frac{1}{2}m\omega_z^2 z_t^2\right\} dx_t\, dz_t\, dp_x\, dp_z. \end{aligned} \tag{4.78}$$

Due to the change in variables from x to x_t and from z to z_t, equation 4.78 contains no terms in θ. As a result, the density of states is independent of tilt angle. Evaluating the integral in equation 4.78 (see appendix B for details of calculation) yields

$$D_{AV}\left(E\right) = \sqrt{\frac{2}{m}}\frac{2}{\omega_x\omega_z\hbar^2\pi}\int_0^{\frac{\pi\hbar}{d}}\sqrt{E - E_b\left(p_x\right)}dp_x. \tag{4.79}$$

It is more convenient to express this in terms of the number of states, which is related to the density of states by

$$N_{AV}\left(E\right) = \int_0^E D_{AV}\left(E\right) dE = \sqrt{\frac{2}{m}} \frac{4}{3\omega_x \omega_z \hbar^2 \pi} \int_0^{\frac{\pi\hbar}{d}} \left\{E - E_b\left(p_x\right)\right\}^{\frac{3}{2}} dp_x. \tag{4.80}$$

The integral in equation 4.80 has to be evaluated numerically, since $E_b\left(p_x\right)$ is not expressible in closed form.

Figure 4.11(a) shows $N\left(E\right)$ (solid curve) and $N_{AV}\left(E\right)$ (dashed curve) plotted on the same axes. Even though $N_{AV}\left(E\right)$ is derived from an effective classical Hamiltonian (equation 4.56), it gives a good approximation to the $N\left(E\right)$ staircase function obtained from full quantum-mechanical calculations. This supports the premise that a semi-classical picture of band dynamics is valid. Although $N\left(E\right)$ closely follows the smooth $N_{AV}\left(E\right)$ function, it oscillates about it in a sharp, erratic fashion. This reminds the theorist that the density of states is a combination of two components: a smooth, slowly-varying component, and an irregular, rapidly-varying component. This idea was explained in section 2.3.1, and outlined in equation 4.72.

Theory predicts that periodic orbits impose periodic modulations in $D_{OS}\left(E\right)$, which are known as *Gutzwiller fluctuations* (see section 2.3.1). They have an energy period of $\frac{h}{T}$, where T is the period of the orbit responsible. The importance of periodic orbits has already been demonstrated in the example of the S-shaped scarred wavefunctions (figure 4.9), which occurred regularly in the energy level spectrum. In order to identify the periodic fluctuations in $D_{OS}\left(E\right)$, its Fourier transform $F\left(T\right)$ was taken as follows:

$$F\left(T\right)=\int_{E_{N_1}}^{E_{N_2}} D_{OS}\left(E\right)e^{-\frac{iET}{\hbar}}dE=\int_{E_{N_1}}^{E_{N_2}}\left[D\left(E\right)-D_{AV}\left(E\right)\right]e^{-\frac{iET}{\hbar}}dE. \tag{4.81}$$

The theorist chooses a suitable energy range over which to perform this integration. The limits of the integration must be sufficiently far apart for the energy range to contain many Gutzwiller fluctuations. However, the limits must also be sufficiently close together to ensure that the phase space structure does not change radically over the range of energy.

$D\left(E\right)$ is simply a stick spectrum, so it can be represented by a sum of δ-functions as shown in equation 4.82. A Welch window function $W\left(E\right)$ [60] has also been included to suppress ringing in the Fourier transform.

$$F\left(T\right)=\int_{E_{N_1}}^{E_{N_2}}\left[\sum_{j=N_1}^{N_2}\delta\left(E-E_j\right)-D_{AV}\left(E\right)\right]W\left(E\right)e^{-\frac{iET}{\hbar}}dE, \tag{4.82}$$

where

$$W\left(E\right)=1-\left(\frac{2E-E_{N_2}-E_{N_1}}{E_{N_2}-E_{N_1}}\right)^2. \tag{4.83}$$

It follows directly from equation 4.82 that

$$F\left(T\right)=\sum_{j=N_1}^{N_2}W\left(E_j\right)e^{-\frac{iE_jT}{\hbar}}-\int_{E_{N_1}}^{E_{N_2}}D_{AV}\left(E\right)W\left(E\right)e^{-\frac{iET}{\hbar}}dE, \tag{4.84}$$

where $D_{AV}\left(E\right)$ is given by equation 4.79.

$F\left(T\right)$ is plotted in figure 4.11(b). The three peaks marked by solid arrows occur at $T=2.50$ms, 3.08ms and 7.77ms. These times correspond to the periods of the orbits shown as insets in figure 4.11(b). The two shortest orbits are stable, and were previously shown in figure 4.8. The longest of the three orbits is the familiar unstable S-shaped orbit, studied in figures 4.7(c) and 4.9. The peaks in the Fourier transform have a finite width since the periods of the orbits gradually change over the range of energies studied. There are three additional peaks indicated by dotted arrows, labelled 1-3. Peaks 1 and 3 are harmonics of the maxima at 2.50ms and 3.08ms respectively. There is no periodic orbit corresponding to peak 2. It probably originates from complex 'ghost' trajectories [24] (see section 2.3.2).

Chapter 5

Creation of solitons and vortices by Bragg reflection of Bose-Einstein condensates in an optical lattice

5.1 Introduction

Over the past three years, several techniques have been developed to create and detect topological excitations in dilute gas Bose-Einstein condensates. In analogy to the famous 'rotating bucket' experiment with liquid helium, it is possible to create vortex lattices by rotating the condensate [52, 53]. More recently, Strecker et al. successfully created chains of bright solitons by inverting the sign of the scattering length [62]. Many of the techniques involve using laser potentials to modify the phase or density profile of the condensate. Some groups used the homogeneous dipole potential of a laser beam to imprint a phase shift of approximately π on one side of a condensate [47, 48]. The resulting phase slip produces a dark soliton. Burger et al. [63] later used a focused laser to create a local minimum in a condensate on the scale of the healing length, which then evolves into pairs of solitons. Other groups used similar techniques, but moved the laser potential in order to produce pairs of vortices with opposite circulation [64, 65]. In this study, Bragg reflection is proposed as a new mechanism for manipulating the condensate phase and density, hence producing solitons and vortices.

This chapter discusses dilute rubidium (^{87}Rb) gas condensates, which are accelerated through the lowest band of a one-dimensional OL. This may lead to Bloch oscillations, depending on the system parameters. Experiments have confirmed that for low equilibrium peak densities, typically 10^{14} cm^{-3} or lower, ^{87}Rb condensates undergo Bloch oscillations in OLs [42, 66]. Hitherto, numerical studies have not related such motion to changes in the *internal structure* of the condensate [67, 68, 69]. This chapter uses the two and three-dimensional Gross-Pitaevskii equations to examine the topological excitations produced via Bragg reflection, and the subsequent breakdown of Bloch oscillations.

The system studied in this chapter is summarised in figure 5.1, and shall be referred to as system A. A dilute gas condensate of 1.2×10^4 ^{87}Rb atoms is prepared in a one-dimensional OL and a harmonic magnetic trap. The potential energy profiles due to the OL and the trap are described respectively by the following equations:

$$V_{\mathrm{OL}}(x) = V_0 \sin^2\left(\frac{\pi x}{d}\right), \tag{5.1}$$

$$V_{\mathrm{trap}}(x, y) = \frac{m}{2}\left(\omega_x^2 x^2 + \omega_y^2 y^2 + \omega_z^2 z^2\right). \tag{5.2}$$

Figure 5.1(a) shows the potential energy profile due to the OL, (solid line). The depth of the OL $V_0 = 1.55 E_R = 23.3$ peV, and period $d = \frac{\lambda}{2} = 397.5$ nm, are taken from experiment [69]. The periodic potential of the OL produces a band structure, which was calculated using Mathieu functions, as in section 4.2. The energy range of the lowest band is indicated in figure 5.1(a) by a grey rectangle. As the figure shows, the width of the lowest band, Δ_{BW}, is 0.67 E_R (10.0 peV). The bottom of the second band is above the top of the OL potential at 2.15 E_R (32.2 peV). The trap frequencies of $\omega_x = 2\pi \times 50$ rad s^{-1} and $\omega_y = \omega_z = 2\pi \times 35$ rad s^{-1} are attainable in experiment [42, 69]. In figure 5.1(a), the trap potential energy along $y = z = 0$ (dotted line) is plotted on the same axes as the OL potential energy. The reader will notice that the change in trap potential across each lattice period is much less than the band width of the lowest band. Consequently, the harmonic trap only weakly perturbs the band structure.

At the start of the simulation (t=0) the condensate is in the ground state of the OL and harmonic magnetic trap. (The method of calculating the ground state is described in section 5.3.) Figure 5.1(b) shows the one-dimensional profile of this condensate ground state along $y = z = 0$. The reader will notice that the density profile of the condensate is modulated by the peaks and troughs in the OL potential. The peak density is at the trap minimum, which is initially at $x = 0$. At time $t = 0$, the harmonic trap is displaced along the OL direction, which is defined as the x-axis, (see figure 5.1). Displacing the trap increases the potential energy of the condensate, hence driving it into oscillation. If the trap is displaced by a distance Δx (see figure 5.1(b) inset), the increase in the potential energy ΔV of an atom in the condensate can be approximated as

$$\Delta V \simeq \frac{1}{2} m \omega_x^2 \left(\Delta x\right)^2 . \tag{5.3}$$

This potential energy is then converted into kinetic energy as the condensate

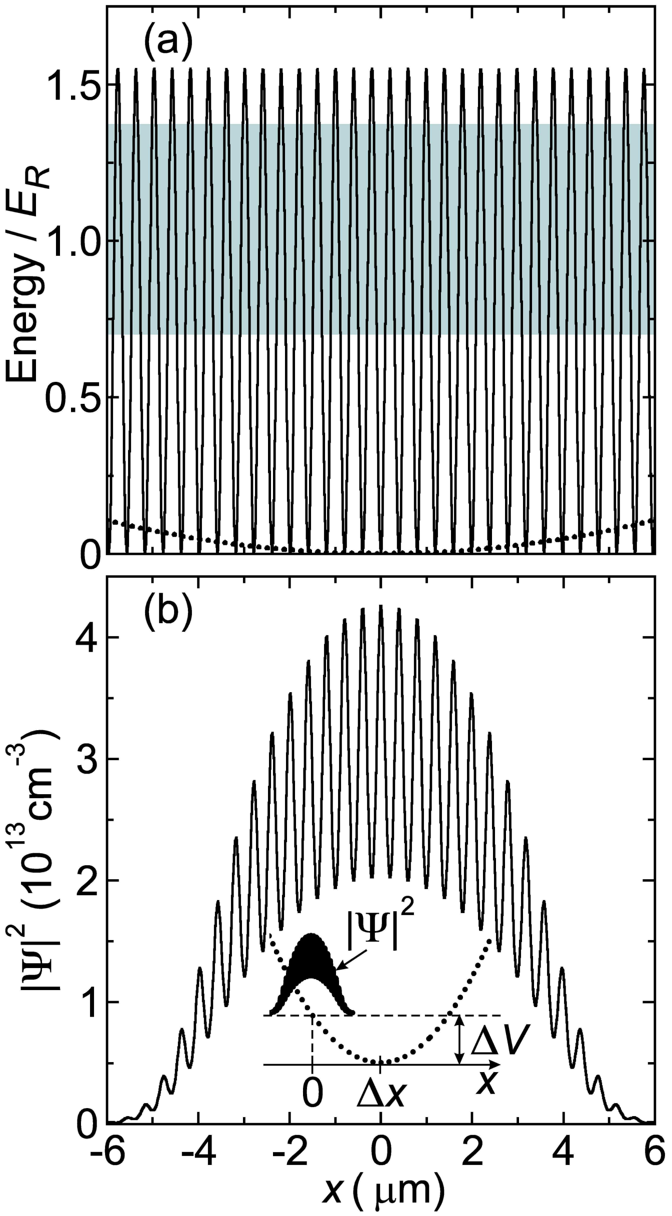

Figure 5.1: (a) Solid curve: potential energy profile of the OL. Grey rectangle: energy range of the lowest energy band. Dotted curve: x-dependence of the harmonic potential energy for $y = z = 0$ ($\rho = 0$). (b) Initial density profile of the condensate, along $y = z = 0$ ($\rho = 0$). Inset: density profile and x-dependence of the harmonic potential energy (dotted) immediately after trap displacement.

is accelerated up the first energy band. If the condensate is to reach the top of the band and undergo Bragg reflection, the increase in potential energy ΔV must equal or exceed the band width Δ_{BW}. This implies the following lower limit on the trap displacement:

$$\Delta x \geq \sqrt{\frac{2\Delta_{\mathrm{BW}}}{m\omega_x^2}} = 15\ \mu\mathrm{m}. \tag{5.4}$$

The dynamics of the condensate, both in terms of its centre of mass motion and its internal structure, are wildly different depending on whether the trap displacement is below or above this critical value. The two regimes will be investigated in sections 5.4 and 5.5 respectively.

5.2 Numerical integration of the Gross-Pitaevskii equation

In this study, the dynamics of Bose-Einstein condensates are simulated by numerically solving the Gross-Pitaevskii equation. This equation assumes that the mean interparticle spacing is much greater than the scattering length, and that the condensate is at zero temperature (see section 3.4). The condensates considered here have densities of order 10^{14} cm^{-3}, which implies a mean particle spacing of approximately 200 nm. This is approximately forty times the scattering length $a = 5.4$ nm. The latter assumption that the condensate is at zero temperature is, in practice, a good approximation for temperatures well below the transition temperature.

For a condensate in a three-dimensional harmonic oscillator potential, the transition temperature is given by [11]:

$$T_c \approx 4.5 \left(\frac{\bar{F}}{100}\right) N^{\frac{1}{3}}\ \mathrm{nK}, \tag{5.5}$$

where $\overline{F}$ is the geometric mean of the three oscillator frequencies (see section 3.2, equation 3.21). For the parameters specified in section 5.1 the transition temperature is 40nK.

The time-dependent Gross-Pitaevskii equation, as stated in section 3.4, equation 3.41, is

$$i\hbar\frac{\partial\psi\left(\mathbf{r}\right)}{\partial t}=-\frac{\hbar^2}{2m}\nabla^2\psi\left(\mathbf{r}\right)+V_{\mathrm{ext}}\left(\mathbf{r}\right)\psi\left(\mathbf{r}\right)+U_0\left|\psi\left(\mathbf{r}\right)\right|^2\psi\left(\mathbf{r}\right), \tag{5.6}$$

where

$$U_0=\frac{4\pi\hbar^2a}{m}. \tag{5.7}$$

(For ^{87}Rb the scattering length a = 5.4 nm.) In this study, it was most convenient to incorporate the external potential and interaction terms into one effective potential. Hence equation 5.6 becomes

$$i\hbar\frac{\partial\psi\left(\mathbf{r}\right)}{\partial t}=-\frac{\hbar^2}{2m}\nabla^2\psi\left(\mathbf{r}\right)+V\left(\mathbf{r}\right)\psi\left(\mathbf{r}\right), \tag{5.8}$$

where

$$V\left(\mathbf{r}\right)=V_{\mathrm{ext}}\left(\mathbf{r}\right)+U_0\left|\psi\left(\mathbf{r}\right)\right|^2. \tag{5.9}$$

For this system, the external potential $V_{\mathrm{ext}}\left(\mathbf{r}\right)$ is composed of an optical lattice term and a harmonic magnetic trap term:

$$V_{\mathrm{ext}}\left(\mathbf{r}\right)=V_{\mathrm{OL}}\left(x\right)+V_{\mathrm{trap}}\left(\mathbf{r}\right). \tag{5.10}$$

In order to solve equation 5.8 in two dimensions, it is expressed in the following form:

$$i\hbar\frac{\partial\Psi}{\partial t}=-\frac{\hbar^2}{2m}\frac{\partial^2\Psi}{\partial x^2}-\frac{\hbar^2}{2m}\frac{\partial^2\Psi}{\partial y^2}+V\left(x,y\right)\Psi, \tag{5.11}$$

where

$$V\left(x,y\right) = V_{\mathrm{OL}}(x) + V_{\mathrm{trap}}(x,y) + U_0 \left|\Psi\right|^2. \tag{5.12}$$

Initially, three-dimensional calculations appeared impossible due to the limitations of computer speed and memory, so equation 5.11 was solved to generate two-dimensional results. These calculations were later extended to three dimensions by exploiting the cylindrical symmetry of the problem, hence avoiding making more demands on computer memory and time. Since three-dimensional simulations are closer to the reality of current condensate experiments, this report shall put most emphasis on the three-dimensional calculations, and only briefly describe how the two-dimensional calculations compare.

The three-dimensional calculations were performed by expressing equation 5.8 in cylindrical polar coordinates:

$$i\hbar\frac{\partial\psi}{\partial t} = -\frac{\hbar^2}{2m}\left\{\frac{\partial^2\psi}{\partial x^2} + \frac{\partial^2\psi}{\partial\rho^2} + \frac{1}{\rho}\frac{\partial\psi}{\partial\rho} + \frac{1}{\rho^2}\frac{\partial^2\psi}{\partial\varphi^2}\right\} + V\left(x,\rho\right)\psi, \tag{5.13}$$

where ρ and φ are defined by

$$\rho = \sqrt{y^2+z^2}\,, \tag{5.14}$$

$$\varphi = \tan^{-1}\left(\frac{y}{z}\right). \tag{5.15}$$

Since the external potential is cylindrically symmetrical around the x-axis, there are solutions of equation 5.13 which are independent of φ, as well as solutions which are φ-dependent. This study examines the evolution of the lowest energy state of the optical lattice plus trap potential, so only φ-independent solutions are considered. As a result, ψ can be expressed as a function of x and ρ, and the $\frac{\partial^2\psi}{\partial\varphi^2}$ term in equation 5.13 is equal to zero.

Hence equation 5.13 becomes

$$i\hbar\frac{\partial\psi\left(x,\rho\right)}{\partial t}=-\frac{\hbar^{2}}{2m}\left\{\frac{\partial^{2}\psi\left(x,\rho\right)}{\partial x^{2}}+\frac{\partial^{2}\psi\left(x,\rho\right)}{\partial\rho^{2}}+\frac{1}{\rho}\frac{\partial\psi\left(x,\rho\right)}{\partial\rho}\right\}$$
$$+V\left(x,\rho\right)\psi\left(x,\rho\right). \quad (5.16)$$

If the ρ's are replaced by y's, this equation is very similar to the two-dimensional equivalent (equation 5.11). The only difference is the extra $\frac{\partial\psi(x,\rho)}{\partial\rho}$ term in equation 5.16. The calculations in this report show that this term rapidly becomes small as ρ increases from zero, and has little effect on the dynamics. Consequently, the general behaviour in two and three dimensions is essentially the same. Since this report concentrates on the three-dimensional results, the remainder of this section will be dedicated to solving the three-dimensional problem (equation 5.16). The method used to solve the two-dimensional problem (equation 5.11) is exactly the same, the only difference being that the $\frac{\partial\psi(x,\rho)}{\partial\rho}$ term is not present in the two-dimensional case.

The non-linear $|\Psi|^2$ term makes the Gross-Pitaevskii equation impossible to solve analytically, except in a few very simple cases. Hence, equation 5.16 must be integrated numerically to determine the time-dependent dynamics of the system. This is done by representing the condensate on a grid of points, and calculating the wavefunction at finite time steps. Consequently, the derivatives are approximated from discrete points and the differential equation 5.16 becomes an approximate *finite-difference* equation. This is known as the *finite-difference method.*

Every time step, a small change to the wavefunction is calculated. Thus the wavefunction evolves in time. In order to maintain a simple relationship between the wavefunction at time step n and the wavefunction at time step

$n+1$, the first order temporal derivative in equation 5.16 is approximated by

$$\frac{\partial \Psi_{j,l}}{\partial t} \approx \frac{\Psi_{j,l}^{n+1} - \Psi_{j,l}^{n}}{\Delta_t}, \tag{5.17}$$

where Δ_t is the size of each time step, and the integers j and l are the coordinates of a particular point on the rectangular wavefunction grid in the x and ρ-directions respectively. The spatial derivatives with respect to x are approximated by taking the Taylor expansions

$$\Psi_{j+1,l} \approx \Psi_{j,l} + \Delta_x \left.\frac{\partial \Psi}{\partial x}\right|_{j,l} + \frac{\Delta_x^2}{2} \left.\frac{\partial^2 \Psi}{\partial x^2}\right|_{j,l}, \tag{5.18}$$

and

$$\Psi_{j-1,l} \approx \Psi_{j,l} - \Delta_x \left.\frac{\partial \Psi}{\partial x}\right|_{j,l} + \frac{\Delta_x^2}{2} \left.\frac{\partial^2 \Psi}{\partial x^2}\right|_{j,l}. \tag{5.19}$$

where Δ_x is the grid spacing in the x-direction. Adding equations 5.18 and 5.19 yields

$$\left.\frac{\partial^2 \Psi}{\partial x^2}\right|_{j,l} \approx \frac{\Psi_{j+1,l} - 2\Psi_{j,l} + \Psi_{j-1,l}}{\Delta_x^2}. \tag{5.20}$$

Subtracting equation 5.19 from equation 5.18 yields

$$\left.\frac{\partial \Psi}{\partial x}\right|_{j,l} \approx \frac{\Psi_{j+1,l} - \Psi_{j-1,l}}{2\Delta_x}. \tag{5.21}$$

Using approximations 5.17, 5.20 and 5.21, together with equivalent expressions for derivatives with respect to ρ, it is possible to rewrite equation 5.16

as finite difference equation. The result is

$$\frac{\Psi^{n+1}_{j,l}-\Psi^{n}_{j,l}}{\Delta_t}=\frac{i\hbar}{2m}\left(\frac{\Psi^{n}_{j+1,l}-2\Psi^{n}_{j,l}+\Psi^{n}_{j-1,l}}{\Delta_x^2}\right)+$$
$$\frac{i\hbar}{2m}\left(\frac{\Psi^{n}_{j,l+1}-2\Psi^{n}_{j,l}+\Psi^{n}_{j,l-1}}{\Delta_\rho^2}\right)+\frac{i\hbar}{4m\rho\Delta_\rho}\left(\Psi^{n}_{j,l+1}-\Psi^{n}_{j,l-1}\right)-\frac{i}{\hbar}V^{n}_{j,l}\Psi^{n}_{j,l}\,. \tag{5.22}$$

where Δ_ρ is the grid spacing in the ρ-direction.

The reader will notice that every Ψ value on the right-hand side of equation 5.22 corresponds to the condensate wavefunction at the n^{th} time step, which means that the kinetic and potential energy terms are calculated from the wavefunction at the n^{th} time step. Since Ψ^n is known, the right-hand side of the equation can be immediately evaluated, and the equation solved for Ψ^{n+1}. Equation 5.22 is known as an *explicit scheme*, as it can be explicitly solved using quantities already known. However, it would be equally valid to calculate the kinetic and potential energy terms from the wavefunction at the $(n+1)^{\text{th}}$ time step, by replacing all the Ψ^n's on the right-hand side of equation 5.22 with Ψ^{n+1}'s. In which case, the finite difference equation is called an *implicit scheme*, and is given by

$$\frac{\Psi^{n+1}_{j,l}-\Psi^{n}_{j,l}}{\Delta_t}=\frac{i\hbar}{2m}\left(\frac{\Psi^{n+1}_{j+1,l}-2\Psi^{n+1}_{j,l}+\Psi^{n+1}_{j-1,l}}{\Delta_x^2}\right)+$$
$$\frac{i\hbar}{2m}\left(\frac{\Psi^{n+1}_{j,l+1}-2\Psi^{n+1}_{j,l}+\Psi^{n+1}_{j,l-1}}{\Delta_\rho^2}\right)+\frac{i\hbar}{4m\rho\Delta_\rho}\left(\Psi^{n+1}_{j,l+1}-\Psi^{n+1}_{j,l-1}\right)-\frac{i}{\hbar}V^{n+1}_{j,l}\Psi^{n+1}_{j,l}\,. \tag{5.23}$$

Solving an implicit scheme is far more difficult than solving the corresponding explicit scheme. This is because explicit scheme equations contain just one grid-point value of Ψ^{n+1}, and so they can be solved individually.

In contrast, implicit scheme equations contain several grid-point values of Ψ^{n+1}, and so are coupled. Both schemes have the disadvantage that different sides of the equation are centred at different times. Specifically, the left-hand side of the explicit scheme (equation 5.22) is centred at time $n + \frac{1}{2}$, while the right-hand side is centred at time n. The left-hand side of the implicit scheme is also centred at time $n + \frac{1}{2}$, but the right-hand side is centred at time $n + 1$. In order to create an equation which has both sides centred at the same time, the theorist must take an average of the explicit and implicit schemes. This is called the *Crank-Nicolson* method [60], which gives the finite difference equation

$$\begin{aligned}
\frac{\Psi^{n+1}_{j,l} - \Psi^{n}_{j,l}}{\Delta_t} = \frac{1}{2}\times \\
\Bigg[\frac{i\hbar}{2m\Delta_x^2}\left\{\left(\Psi^{n+1}_{j+1,l} - 2\Psi^{n+1}_{j,l} + \Psi^{n+1}_{j-1,l}\right) + \left(\Psi^{n}_{j+1,l} - 2\Psi^{n}_{j,l} + \Psi^{n}_{j-1,l}\right)\right\} \\
\frac{i\hbar}{2m\Delta_\rho^2}\left\{\left(\Psi^{n+1}_{j,l+1} - 2\Psi^{n+1}_{j,l} + \Psi^{n+1}_{j,l-1}\right) + \left(\Psi^{n}_{j,l+1} - 2\Psi^{n}_{j,l} + \Psi^{n}_{j,l-1}\right)\right\} \\
\frac{i\hbar}{4m\rho\Delta_\rho}\left\{\left(\Psi^{n+1}_{j,l+1} - \Psi^{n+1}_{j,l-1}\right) + \left(\Psi^{n}_{j,l+1} - \Psi^{n}_{j,l-1}\right)\right\} \\
-\frac{i}{\hbar}V^{n+1}_{j,l}\Psi^{n+1}_{j,l} - \frac{i}{\hbar}V^{n}_{j,l}\Psi^{n}_{j,l}\Bigg] \; . \qquad (5.24)
\end{aligned}$$

Equation 5.24 can be rearranged so all the Ψ^{n+1} terms are on the left-hand side, and all Ψ^{n} terms are on the right. The equation can then be rewritten as a matrix problem and solved for Ψ^{n+1}. However, although this method is, in principle, sound, in practice the matrices rapidly become huge as the resolution of the grid increases. Unfortunately, for the system considered in this report, it was found that computer time and memory forbid an adequate grid resolution.

This problem was overcome by using the *time splitting* or *operator splitting* method [60]. In order to explain this technique, equation 5.24 has been rearranged as follows:

$$
\begin{aligned}
\Psi^{n+1}_{j,l} &= \Psi^{n}_{j,l} + \frac{\Delta_t}{2}\times \\
&\left[\frac{i\hbar}{2m\Delta x^2}\left\{\left(\Psi^{n+1}_{j+1,l} - 2\Psi^{n+1}_{j,l} + \Psi^{n+1}_{j-1,l}\right) + \left(\Psi^{n}_{j+1,l} - 2\Psi^{n}_{j,l} + \Psi^{n}_{j-1,l}\right)\right\}\right. \\
&\quad \frac{i\hbar}{2m\Delta_\rho^2}\left\{\left(\Psi^{n+1}_{j,l+1} - 2\Psi^{n+1}_{j,l} + \Psi^{n+1}_{j,l-1}\right) + \left(\Psi^{n}_{j,l+1} - 2\Psi^{n}_{j,l} + \Psi^{n}_{j,l-1}\right)\right\} \\
&\qquad \frac{i\hbar}{4m\rho\Delta_\rho}\left\{\left(\Psi^{n+1}_{j,l+1} - \Psi^{n+1}_{j,l-1}\right) + \left(\Psi^{n}_{j,l+1} - \Psi^{n}_{j,l-1}\right)\right\} \\
&\qquad\qquad \left. -\frac{i}{\hbar}V^{n+1}_{j,l}\Psi^{n+1}_{j,l} - \frac{i}{\hbar}V^{n}_{j,l}\Psi^{n}_{j,l}\right].
\end{aligned}
\tag{5.25}
$$

This equation is of the form:

$$
\Psi^{n+1}_{j,l} = \Psi^{n}_{j,l} + \Delta\Psi, \tag{5.26}
$$

where

$$
\begin{aligned}
\Delta\Psi &= \frac{\Delta_t}{2}\times \\
&\left[\frac{i\hbar}{2m\Delta x^2}\left\{\left(\Psi^{n+1}_{j+1,l} - 2\Psi^{n+1}_{j,l} + \Psi^{n+1}_{j-1,l}\right) + \left(\Psi^{n}_{j+1,l} - 2\Psi^{n}_{j,l} + \Psi^{n}_{j-1,l}\right)\right\}\right. \\
&\quad \frac{i\hbar}{2m\Delta_\rho^2}\left\{\left(\Psi^{n+1}_{j,l+1} - 2\Psi^{n+1}_{j,l} + \Psi^{n+1}_{j,l-1}\right) + \left(\Psi^{n}_{j,l+1} - 2\Psi^{n}_{j,l} + \Psi^{n}_{j,l-1}\right)\right\} \\
&\qquad \frac{i\hbar}{4m\rho\Delta_\rho}\left\{\left(\Psi^{n+1}_{j,l+1} - \Psi^{n+1}_{j,l-1}\right) + \left(\Psi^{n}_{j,l+1} - \Psi^{n}_{j,l-1}\right)\right\} \\
&\qquad\qquad \left. -\frac{i}{\hbar}V^{n+1}_{j,l}\Psi^{n+1}_{j,l} - \frac{i}{\hbar}V^{n}_{j,l}\Psi^{n}_{j,l}\right].
\end{aligned}
\tag{5.27}
$$

The single time step in equation 5.26 can be split into two steps by creating an intermediate state $\Psi^{n+\frac{1}{2}}_{j,l}$ between the states $\Psi^{n}_{j,l}$ and $\Psi^{n+1}_{j,l}$. The first step maps the wavefunction at time step n to that at time step $n+\frac{1}{2}$, and the second step maps the wavefunction at time step $n+\frac{1}{2}$ to that at time step

$n+1$. This is more easily explained mathematically. The first step is

$$\Psi_{j,l}^{n+\frac{1}{2}} = \Psi_{j,l}^{n} + \Delta\Psi_a \,, \tag{5.28}$$

and the second step is

$$\Psi_{j,l}^{n+1} = \Psi_{j,l}^{n+\frac{1}{2}} + \Delta\Psi_b \,. \tag{5.29}$$

In order for equations 5.28 and 5.29 to be equivalent to equation 5.26, $\Delta\Psi_a$ and $\Delta\Psi_b$ must satisfy

$$\Delta\Psi = \Delta\Psi_a + \Delta\Psi_b \,. \tag{5.30}$$

Applying this splitting technique to equation 5.25 produces the following equations, which are equivalent in form to equations 5.28 and 5.29:

$$\begin{aligned}\Psi_{j,l}^{n+\frac{1}{2}} = \Psi_{j,l}^{n} + \frac{\Delta_t}{2} \times \Bigg[& \frac{i\hbar}{2m\Delta_x^2}\left(\Psi_{j+1,l}^{n+\frac{1}{2}} - 2\Psi_{j,l}^{n+\frac{1}{2}} + \Psi_{j-1,l}^{n+\frac{1}{2}}\right) + \\ & \frac{i\hbar}{2m\Delta_\rho^2}\left(\Psi_{j,l+1}^{n} - 2\Psi_{j,l}^{n} + \Psi_{j,l-1}^{n}\right) + \frac{i\hbar}{4m\rho\Delta_\rho}\left(\Psi_{j,l+1}^{n} - \Psi_{j,l-1}^{n}\right) \\ & - \frac{i}{2\hbar}V_{j,l}^{n+\frac{1}{2}}\Psi_{j,l}^{n+\frac{1}{2}} - \frac{i}{2\hbar}V_{j,l}^{n}\Psi_{j,l}^{n}\Bigg] \,,\end{aligned} \tag{5.31}$$

and

$$\begin{aligned}\Psi_{j,l}^{n+1} = \Psi_{j,l}^{n+\frac{1}{2}} + \frac{\Delta_t}{2} \times \Bigg[& \frac{i\hbar}{2m\Delta_x^2}\left(\Psi_{j+1,l}^{n+\frac{1}{2}} - 2\Psi_{j,l}^{n+\frac{1}{2}} + \Psi_{j-1,l}^{n+\frac{1}{2}}\right) + \\ & \frac{i\hbar}{2m\Delta_\rho^2}\left(\Psi_{j,l+1}^{n+1} - 2\Psi_{j,l}^{n+1} + \Psi_{j,l-1}^{n+1}\right) + \frac{i\hbar}{4m\rho\Delta_\rho}\left(\Psi_{j,l+1}^{n+1} - \Psi_{j,l-1}^{n+1}\right) \\ & - \frac{i}{2\hbar}V_{j,l}^{n+\frac{1}{2}}\Psi_{j,l}^{n+\frac{1}{2}} - \frac{i}{2\hbar}V_{j,l}^{n+1}\Psi_{j,l}^{n+1}\Bigg] \,.\end{aligned} \tag{5.32}$$

Careful inspection of equations 5.31 and 5.32 reveals that equation 5.25 has not been split quite as simply and exactly as the illustration in equations 5.28 to 5.30. Consider the square bracket in equation 5.25. The first line (uppermost) in the bracket corresponds to $\frac{\partial^2\Psi}{\partial x^2}$ terms, the second line corresponds to $\frac{\partial^2\Psi}{\partial \rho^2}$ terms, the third line corresponds to $\frac{\partial\Psi}{\partial\rho}$ terms, and the forth line (bottom) corresponds to potential terms. The second line has indeed been split exactly between the two equations. The first half of the second line can be found in equation 5.32, while the second half can be found in equation 5.31. The third line has also been split exactly. However, the $\frac{\partial^2\Psi}{\partial x^2}$ terms in equation 5.25 contain terms in Ψ^n and terms in Ψ^{n+1}, but these are not found in equations 5.31 and 5.32. In their place are terms in $\Psi^{n+\frac{1}{2}}$. However, a little thought will convince the reader that the sum of the $\frac{\partial^2\Psi}{\partial x^2}$ terms in equations 5.31 and 5.32 is a very close approximation to the $\frac{\partial^2\Psi}{\partial x^2}$ terms in equation 5.25. Similarly, the potential terms in equation 5.25 are not the exact sum of the potential terms in equations 5.31 and 5.32. However, again they are are very close to being so.

So why have the terms in equation 5.25 not been split exactly between the two equations 5.31 and 5.32? The answer is that the chosen split allows the equations 5.31 and 5.32 to be written as two tridiagonal matrix problems. These are far easier to solve, and require much less memory than general matrix problems. Hence the computing problems associated with equation 5.24 have been overcome by the operator splitting technique.

Rearranging equation 5.31 yields

$$\begin{aligned}
&-i\varsigma_x\Psi^{n+\frac{1}{2}}_{j-1,l} + \left(1 + 2i\varsigma_x + \frac{i\Delta_t}{4\hbar}V^{n+\frac{1}{2}}_{j,l}\right)\Psi^{n+\frac{1}{2}}_{j,l} - i\varsigma_x\Psi^{n+\frac{1}{2}}_{j+1,l} = \\
&\left(i\varsigma_\rho - \frac{i\gamma_\rho}{\rho}\right)\Psi^n_{j,l-1} + \left(1 - 2i\varsigma_\rho - \frac{i\Delta_t}{4\hbar}V^n_{j,l}\right)\Psi^n_{j,l} + \left(i\varsigma_\rho + \frac{i\gamma_\rho}{\rho}\right)\Psi^n_{j,l+1}\,,
\end{aligned} \tag{5.33}$$

$$\text{where} \quad \varsigma_x = \frac{\hbar \Delta_t}{4m\Delta_x^2} \, , \tag{5.34}$$

$$\text{and} \quad \varsigma_\rho = \frac{\hbar \Delta_t}{4m\Delta_\rho^2} \, , \tag{5.35}$$

$$\text{and} \quad \gamma_\rho = \frac{\hbar \Delta_t}{8m\Delta_\rho} \, . \tag{5.36}$$

Similar simplification of equation 5.32 yields

$$\begin{aligned} &\left(\frac{i\gamma_\rho}{\rho} - i\varsigma_\rho\right) \Psi^{n+1}_{j,l-1} + \left(1 + 2i\varsigma_\rho + \frac{i\Delta_t}{4\hbar} V^{n+1}_{j,l}\right) \Psi^{n+1}_{j,l} + \left(-\frac{i\gamma_\rho}{\rho} - i\varsigma_\rho\right) \Psi^{n+1}_{j,l+1} \\ &\qquad = i\varsigma_x \Psi^{n+\frac{1}{2}}_{j-1,l} + \left(1 - 2i\varsigma_x - \frac{i\Delta_t}{4\hbar} V^{n+\frac{1}{2}}_{j,l}\right) \Psi^{n+\frac{1}{2}}_{j,l} + i\varsigma_x \Psi^{n+\frac{1}{2}}_{j+1,l} \, . \end{aligned} \tag{5.37}$$

Equations 5.33 and 5.37 can be written in the form of the two matrix equations

$$\mathbf{A}\Psi^{n+\frac{1}{2}} = \mathbf{B}\Psi^{n}, \tag{5.38}$$

and

$$\mathbf{A}'\Psi^{n+1} = \mathbf{B}'\Psi^{n+\frac{1}{2}}, \tag{5.39}$$

where $\mathbf{A}$, $\mathbf{B}$, $\mathbf{A}'$ and $\mathbf{B}'$ are matrices with three non-zero diagonals, and Ψ is a column matrix. In order for the operator splitting method to be useful, the matrices $\mathbf{A}$ and $\mathbf{A}'$ have to be tridiagonal. This is only possible if the method of storage of the wavefunction grid in the column matrix Ψ changes between the two steps. When evaluating equation 5.38, the i^{th} value of the column matrix Ψ and the grid position (j, l) are related by

$$i = l \times \text{GridW} + j \, , \tag{5.40}$$

and when evaluating equation 5.39 they are related by

$$i = j \times \text{GridH} + l \, , \tag{5.41}$$

where GridW and GridH specify respectively the number of points in the x- and ρ-direction of the wavefunction grid.

The matrix problem in equations 5.38 and 5.39 can now be written in the form:

$$\mathbf{M}\Psi = \mathbf{C}\,, \tag{5.42}$$

where $\mathbf{M}$ is tridiagonal, and Ψ and $\mathbf{C}$ are column matrices. The problem is solved by writing matrix $\mathbf{M}$ as the product of two matrices $\mathbf{L}$ and $\mathbf{U}$, where $\mathbf{L}$ is lower triangular (has elements only on the leading diagonal and the subsequent sub-diagonal), and $\mathbf{U}$ is upper triangular (has elements only on the leading diagonal and the subsequent super-diagonal):

$$\mathbf{M} = \mathbf{L} \times \mathbf{U}\,. \tag{5.43}$$

By substituting the product $\mathbf{L} \times \mathbf{U}$ for $\mathbf{M}$ as shown in equation 5.44, the matrix problem 5.42 can be split into the two simpler matrix problems 5.45 and 5.46.

$$\mathbf{M}\Psi = (\mathbf{L} \times \mathbf{U})\,\Psi = \mathbf{L} \times (\mathbf{U} \times \Psi) = \mathbf{C}\,. \tag{5.44}$$

$$\text{If the column vector } \mathbf{Y} \text{ is defined by } \mathbf{Y} = \mathbf{U} \times \Psi\,, \tag{5.45}$$

$$\text{then equation 5.44 can be rewritten as } \mathbf{L} \times \mathbf{Y} = \mathbf{C}\,. \tag{5.46}$$

So rather than solving equation 5.42 for Ψ directly, it is completely equivalent to solve equation 5.46 for $\mathbf{Y}$, and then solve equation 5.45 for Ψ. But what is the advantage of doing so? The advantage is that triangular matrix problems are trivial to solve. The algorithm to solve (say) equation 5.46 works simply by evaluating the elements of $\mathbf{Y}$ in ascending order of index. The theorist finds that, when solving for a particular element of $\mathbf{Y}$, only earlier elements of $\mathbf{Y}$ are needed for the calculation. This technique is known as *LU decomposition* followed by *forward and backward substitution* [60]. It is a robust method that can be applied to any type of square matrix, but is particularly efficient for tridiagonal matrices.

The reader may have noticed that one problem remains. Consider equation 5.38. If the equation is to be solved for $\Psi^{n+\frac{1}{2}}$, matrices $\mathbf{A}$, $\mathbf{B}$ and Ψ^n must be known. However, the evaluation of matrix $\mathbf{A}$ requires the value of $V_{j,l}^{n+\frac{1}{2}}$, which in turn requires $\Psi^{n+\frac{1}{2}}$. In order to resolve this, Ψ^n is used to estimate $V_{j,l}^{n+\frac{1}{2}}$, which is in turn used to obtain an estimate of $\Psi^{n+\frac{1}{2}}$. This estimate is called $\widetilde{\Psi}^{n+\frac{1}{2}}$. $\widetilde{\Psi}^{n+\frac{1}{2}}$ is then used to calculate a better estimate of $V_{j,l}^{n+\frac{1}{2}}$. In effect, this process is a two step iteration towards $\Psi^{n+\frac{1}{2}}$. This is more easily explained in mathematical form. The following four matrix equations 5.47 to 5.50 inclusive summarise the calculations performed during one time step. (N.B. In the following four equations, the round brackets denote “is a function of”.)

$$\mathbf{A}\left(\Psi^n\right)\widetilde{\Psi}^{n+\frac{1}{2}} = \mathbf{B}\left(\Psi^n\right)\Psi^n = \mathbf{C} \tag{5.47}$$

$$\mathbf{A}\left(\widetilde{\Psi}^{n+\frac{1}{2}}\right)\Psi^{n+\frac{1}{2}} = \mathbf{B}\left(\Psi^n\right)\Psi^n = \mathbf{C} \tag{5.48}$$

$$\mathbf{A}'\left(\Psi^{n+\frac{1}{2}}\right)\widetilde{\Psi}^{n+1} = \mathbf{B}'\left(\Psi^{n+\frac{1}{2}}\right)\Psi^{n+\frac{1}{2}} = \mathbf{D} \tag{5.49}$$

$$\mathbf{A}'\left(\widetilde{\Psi}^{n+1}\right)\Psi^{n+1} = \mathbf{B}'\left(\Psi^{n+\frac{1}{2}}\right)\Psi^{n+\frac{1}{2}} = \mathbf{D} \tag{5.50}$$

The accuracy of this method depends on the size of the time steps and grid spacings. The time steps have to be small on the time-scale of the condensate motion. Typically, their values are of the order of microseconds. The grid spacings in the x-direction have to be much less than the period of the optical lattice. More generally, the grid spacings have to be small on the scale of the healing length, so that features such as vortices can be clearly resolved. These conditions are usually approximately equivalent, and typically require a grid spacing of the order of ten nanometres.

5.3 Calculation of the ground state via an imaginary time algorithm

In order to simplify the evolution of the condensate as much as possible and eliminate any spurious effects, great care was taken to ensure that the condensate was in its ground state at time $t = 0$. The ground state chosen was correct for the potential of the OL plus the undisplaced harmonic trap.

The ground state was calculated using an *imaginary time algorithm* [70]. This is an iterative technique that converges on the ground state, provided that it begins with a reasonable initial guess of the ground state. It uses the same equations as the real time simulations, except that every Δ_t is replaced by $-i\Delta_t$. Hence, the simulation is said to be running in *imaginary time*. Specifically, equations 5.47 to 5.50 are solved as for the real time simulations, but the elements of $\mathbf{A}$, $\mathbf{B}$, $\mathbf{A}'$ and $\mathbf{B}'$ are slightly different due to the replacement of the Δ_t's. By inspection of $\mathbf{A}$, $\mathbf{B}$, $\mathbf{A}'$ and $\mathbf{B}'$, the reader will conclude that this operation results in $\mathbf{A}$, $\mathbf{B}$, $\mathbf{A}'$ and $\mathbf{B}'$ being completely real. Consequently, the ground state is completely real, which reduces the computing time required to calculate it.

The method can be understood by expressing the initial guess Ψ_{guess} as a sum of the eigenfunctions Ψ_n of the condensate in the combined harmonic trap and OL potential:

$$\Psi_{\text{guess}} = \sum_n c_n \Psi_n e^{-\frac{iE_n t}{\hbar}} , \tag{5.51}$$

where E_n is the energy of eigenstate Ψ_n, and c_n is a weighting factor which determines the size of Ψ_n's contribution to the summation. If the wavefunction Ψ_{guess} is to evolve in imaginary time, t must be replaced by $-it$. This converts equation 5.51 into equation 5.52:

$$\Psi_{\text{guess}} = \sum_n c_n \Psi_n e^{-\frac{E_n t}{\hbar}} \ . \tag{5.52}$$

Now, the magnitude of each term in the summation is decaying exponentially in time. However, since the ground state Ψ_0 has the lowest energy, it decays slower than all the other eigenstates of the system. Hence, if the wavefunction is allowed to evolve in imaginary time for a long time, eventually only the contribution from the ground state will remain. Of course, the ground state is also decaying in time, albeit slower than the other states, so the wavefunction has to be re-normalised after each iteration. Otherwise, the wavefunction tends to zero.

The ground state must be normalised to the total number of atoms in the condensate N, as shown below:

$$\int_\varphi \int_x \int_\rho |\Psi|^2 \rho \, d\rho \, dx \, d\varphi = N. \tag{5.53}$$

Since the wavefunction is independent of φ, integration with respect to φ merely produces the constant 2π. Hence, the normalisation condition is

$$\int_x \int_\rho |\Psi|^2 \rho \, d\rho \, dx = \frac{N}{2\pi} \ . \tag{5.54}$$

A slice through the condensate ground state along $\rho = 0$ is shown in figure 5.1(b). The modulations in the probability density are due to the OL potential energy profile.

In the case of the two-dimensional calculations, the wavefunctions are two-dimensional functions of x and y, and independent of z. Consequently, the integration with respect to z merely produces a constant L_z, which is the characteristic length of the condensate in the z-direction. Hence the normalisation condition is:

$$\int_y \int_x |\Psi|^2 \, dx \; dy = \frac{N}{L_z} = I_{x,y}. \tag{5.55}$$

L_z is unknown, so the spread in the z-direction is taken to be the same as the spread in the y-direction, which can be calculated as follows:

$$L_z = L_y = 2\sqrt{\int_y \int_x \Psi^* y^2 \Psi dx \; dy} \; . \tag{5.56}$$

Since L_z changes during the evolution in imaginary time, so does $I_{x,y}$. However, this does not effect the algorithm's success in finding the ground state.

The evolution of L_y, and the corresponding values L_x and L_ρ, were monitored during imaginary time simulations. When the fluctuations of these numbers became very small compared to their magnitude (about 0.1%), the algorithm was deemed to have converged. Typically, this required a simulation of approximately 10 ms in imaginary time.

5.4 Results for a 'small' trap displacement of 10 μm

As discussed in section 5.1, the required trap displacement for the condensate in system A to reach the Brillouin zone boundary is 15 μm. For displacements lower than this critical value, the condensate cannot undergo Bragg reflection or Bloch oscillations. Consequently, the condensate oscillates back and forth in the harmonic trap potential.

In this parameter regime, the results of the two and three-dimensional simulations agreed to an accuracy of order 0.1%. Consequently, only the results of the three-dimensional calculations are presented.

Figure 5.2(a) shows how the mean (centre-of-mass) position of the condensate, $< x >$, varies in time for a trap displacement of 10 μm. When the trap is displaced at t = 0 ms, the condensate is in the ground state of the OL and undisplaced harmonic trap. The trap displacement raises the potential energy of the condensate by ΔV, which can be approximated by the relation 5.3. As t increases from zero, the condensate begins to travel in the x-direction, into the harmonic trap potential well, converting its newly-acquired potential energy into kinetic energy. This accelerates the condensate up the first energy band. At t = 5.3 ms, the condensate reaches the bottom of the harmonic trap potential well, and begins to ride up the opposite side, converting its kinetic energy back into potential energy. When t = 10.6 ms the condensate reaches the position $< x >$ = 20 μm, and all of its kinetic energy has been spent climbing the opposite side of the trap. It then falls back into the trap centre. The peak-to-trough amplitude of the motion is simply double the trap displacement, indicating that the condensate is undergoing simple periodic trap oscillations.

Inspection of figure 5.2(a) also reveals that there is no damping of the oscillations, which infers that there is no dissipation of the energy associated with the centre-of-mass motion. This is confirmed by the observation that there are no changes in the internal structure of the condensate. The two insets in figure 5.2(a) show the condensate at t = 10.7 ms (left inset) and t = 21.3 ms (right inset). Both density profiles are the same as that at t = 0 ms.

The results can also be interpreted by studying the distribution of the

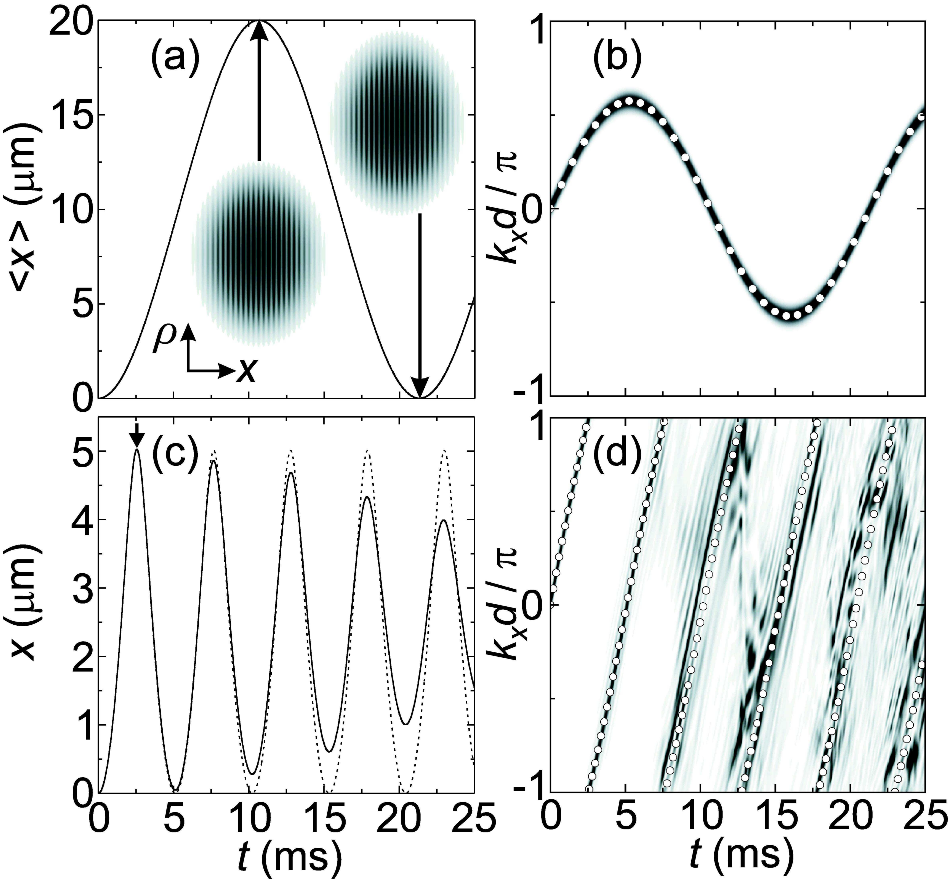

Figure 5.2: (a) $\langle x \rangle$ versus t for system A with $\Delta x = 10$ μm. Insets: grey-scale plots of density (black high) in $x - \rho$ plane (axes inset) at $t =$10.7 ms (left) and 21.3 ms (right). (b) Grey-scale plot: $|f(k_x, t)|^2$ (white = 0, black high) for system A with $\Delta x = 10$ μm. Open circles: points on corresponding semiclassical trajectory $k_x(t)$. (c) Solid curve: $\langle x \rangle$ versus t for system A with $\Delta x = 25$ μm. Arrow marks first turning point. Dashed curve: corresponding semiclassical orbit $x(t)$. (d) As (b), but for $\Delta x = 25$ μm.

condensate in k-space. This is achieved by performing a Fourier transform of the wavefunction along $\rho = 0$ at time t:

$$f\left(k, t\right) = \int_{-\infty}^{\infty} \Psi\left(x, 0, t\right) e^{-ikx} dx \; . \tag{5.57}$$

The integration was performed over the line $\rho = 0$ to simplify the calculation and produce a one-dimensional result.

The Fourier power spectrum, $\left|f\left(k_x, t\right)\right|^2$, corresponding to the motion in figure 5.2(a) is shown in a reduced zone scheme in figure 5.2(b). The plot confirms that at no point during the motion does the condensate cross the Brillouin zone boundary. The trap halts the condensate's passage through the band at $t = 5.3$ ms before it has gained sufficient kinetic energy to reach the top of the band. Consequently, the condensate never Bragg reflects. The distribution in k-space remains narrow throughout the motion, confirming that there is no dissipation of the energy associated with the centre-of-mass motion.

Since the condensate's internal structure does not change with t when $\Delta x = 10$ μm, the results can be understood by considering the motion of a single point particle in the lowest energy band. The single particle trajectories $x\left(t\right)$ and $k_x\left(t\right)$ in real and reciprocal space are determined by the same method used to determine semi-classical paths in section 4.3. In figure 5.2(b) the Fourier power spectrum (grey-scale plot) is overlaid by the corresponding single-particle $k_x\left(t\right)$ curve (white circles). The figure shows that the condensate distribution in k-space is tightly concentrated around the single-particle equivalent. The single-particle real-space trajectory, $x\left(t\right)$, is indistinguishable from the plot of $< x >$ verses t shown in figure 5.2(a). This excellent agreement between the two theories demonstrates that for displacements below the critical value, the condensate behaves like a single point particle, obeying semi-classical equations of motion. Given this fact, it is not surprising that the two-dimensional and three-dimensional results are almost identical in this parameter regime. Finally, it should be noted that the agreement of the quantum mechanics with semi-classical theory confirms the validity of this numerical solution of the Gross-Pitaevskii equation.

5.5 Results for a 'large' trap displacement of 25 μm

For displacements above the critical displacement, the condensate will reach the Brillouin zone boundary and undergo Bragg reflection and Bloch oscillations. In this regime, the energy associated with the centre-of-mass motion is dissipated by producing topological excitations in the internal structure of the condensate. Consequently, the condensate dynamics can no longer be described accurately by a simple semi-classical model.

The results of the two- and three-dimensional simulations are very similar in this parameter regime. This section concentrates on the three-dimensional results, but also draws attention to any discrepancies between the two-dimensional and three-dimensional simulations.

Figure 5.2(c) shows how the mean (centre-of-mass) position of the condensate, $< x >$, varies in time following a trap displacement of 25 μm at $t = 0$. The condensate performs periodic motion, similar to the oscillations observed for a trap displacement of 10 μm. However, in contrast to the previous results, the oscillations are now damped. Furthermore, the period and amplitude of the oscillations have decreased despite the increase in trap displacement. The grey-scale plot of $|f(k_x, t)|^2$ (figure 5.2(d)) shows that the motion is fundamentally different to the previous case, since the condensate is now reaching the Brillouin zone boundary and undergoing Bragg reflection.

As t increases from zero, the condensate's mean k_x value rises approximately linearly with t until it reaches the Brillouin zone boundary at 2.6 ms (see figure 5.2(d)). At this time, the condensate undergoes Bragg reflection, which produces the first (arrowed) turning point in figure 5.2(c). The mean k_x value switches to the other edge of the first Brillouin zone and continues to rise linearly with t. At $t = 5.1$ ms, the mean k_x value passes through zero, and the condensate undergoes reflection bounded by the trap potential. This produces the second turning point in figure 5.2(c), at the lower edge of the curve. All of the upper turning points on the curve are caused by Bragg reflection, and all of the lower turning points are caused by trap reflection. This analysis establishes that the condensate is performing Bloch oscillations, but it fails to explain why the motion is damped. (The reader should note that in this system the accelerating potential is quadratic rather than linear, as is usually the case for Bloch oscillations.)

In an attempt to interpret the results, the dynamics are compared to those of a single particle in the lowest energy band, obeying semi-classical laws of motion and band transport. The single particle trajectories $x\,(t)$ and $k_x\,(t)$ in real and reciprocal space are determined by the same method used to determine semi-classical paths in section 4.3. See figures 5.2(c) and 5.2(d), in which $x\,(t)$ and $k_x\,(t)$ are shown respectively by the dashed curve and open circles. Although the quantum and semi-classical results are reminiscent of each other, there are major discrepancies. Namely, although the two theories predict Bloch oscillations of the same period, the semi-classics fails to account for the damping observed in the quantum mechanics (see figure 5.2(c)). Also, for $t \gtrsim 7.5$ ms multiple peaks appear in $|f(k_x,t)|^2$, and after the full 25 ms, the Fourier transform of the condensate wavefunction contains components at all values of k_x. A single-particle model cannot hope to explain this. The discrepancies between the two theories demonstrate that the condensate is deviating from single-particle behaviour. The damping of the motion and the loss of coherence in k-space observed in the quantum-mechanical results indicate that energy is being dissipated via a process that does not occur semi-classically.

The deviation from single-particle behaviour suggests that changes in the internal structure of the condensate could explain the dynamics. To identify these changes, figures 5.3 to 5.8 show key stages in the evolution of the density (left-hand columns) and phase profile (right-hand columns). It is immediately obvious that the internal structure of the condensate changes dramatically throughout the motion. The various aspects of condensate dynamics demonstrated in this figure will be discussed in detail in the remainder of this section. However, the first point of interest is that as t increases from zero, the density minima deepen and fall to zero at the first Bragg reflection, ($t = 2.6$ ms). This is examined in detail in figure 5.9, which shows cross-sections through the wavefunction probability density and phase at $\rho = 0$.

The lower curves in figures 5.9(a), 5.9(b), and 5.9(c) show $|\Psi(x,0,t)|^2$ just before ($t = 2$ ms), at ($t = 2.6$ ms), and just after ($t = 3$ ms) the first Bragg reflection. The upper curves show the wavefunction phase, $\phi(x)$, which is defined as

$$\phi(x) = \tan^{-1}\frac{\mathrm{Im}\{\Psi\}}{\mathrm{Re}\{\Psi\}}\,. \tag{5.58}$$

Figure 5.9 shows $\phi(x)$ modulo 2π.

Just before reflection (figure 5.9(a)), the density near the centre of the

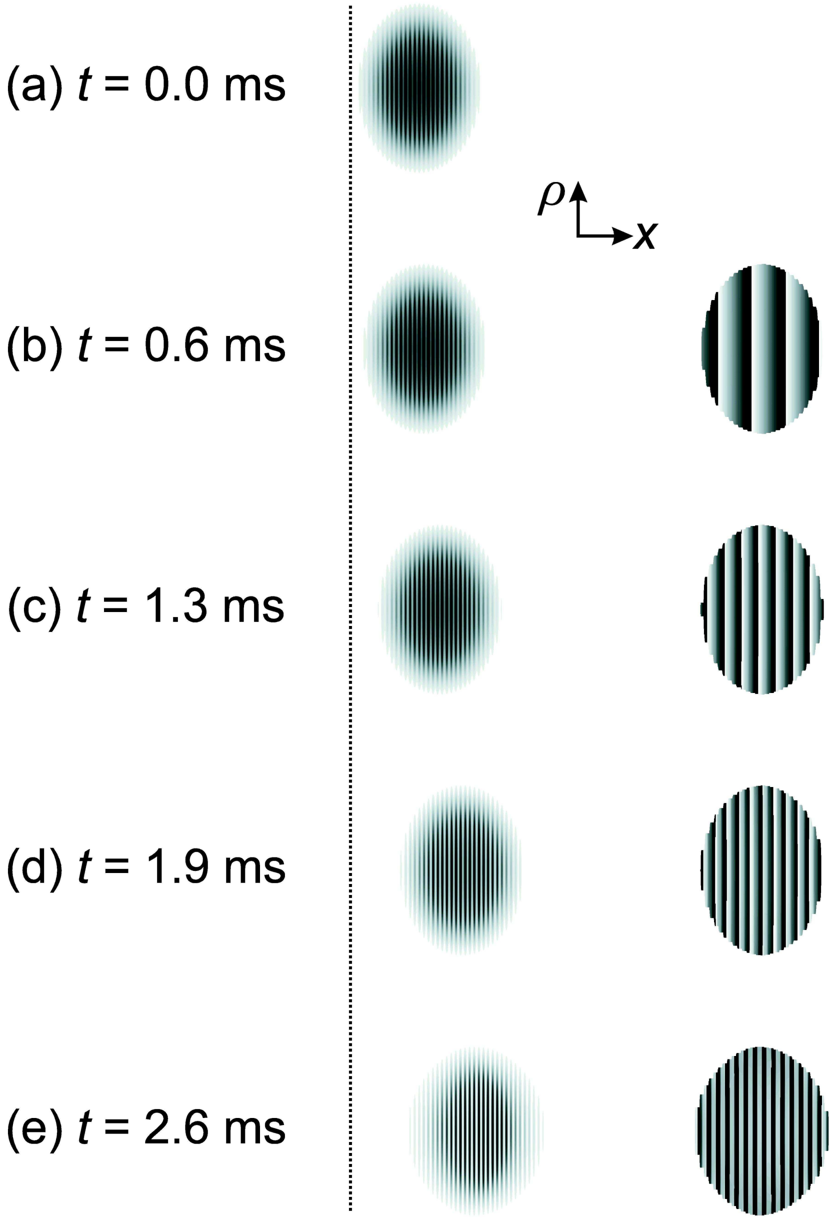

Figure 5.3: Left: Grey-scale plots of density (white = 0, black high) in $x - \rho$ plane (axes inset) for system A with $\Delta x = 25$ μm at various times t. Right: the corresponding phase profiles modulo 2π (white = 0, black = 2π, phase is not shown if corresponding probability density is less than 2% of maximum value). No phase profile is shown for $t = 0$ as the ground state is completely real. Dotted vertical line indicates the plane $x = -6$ μm. The range of t values $0 \leq t \leq 2.6$ ms corresponds to the time interval between the start of the simulation and the condensate's first Bragg reflection.

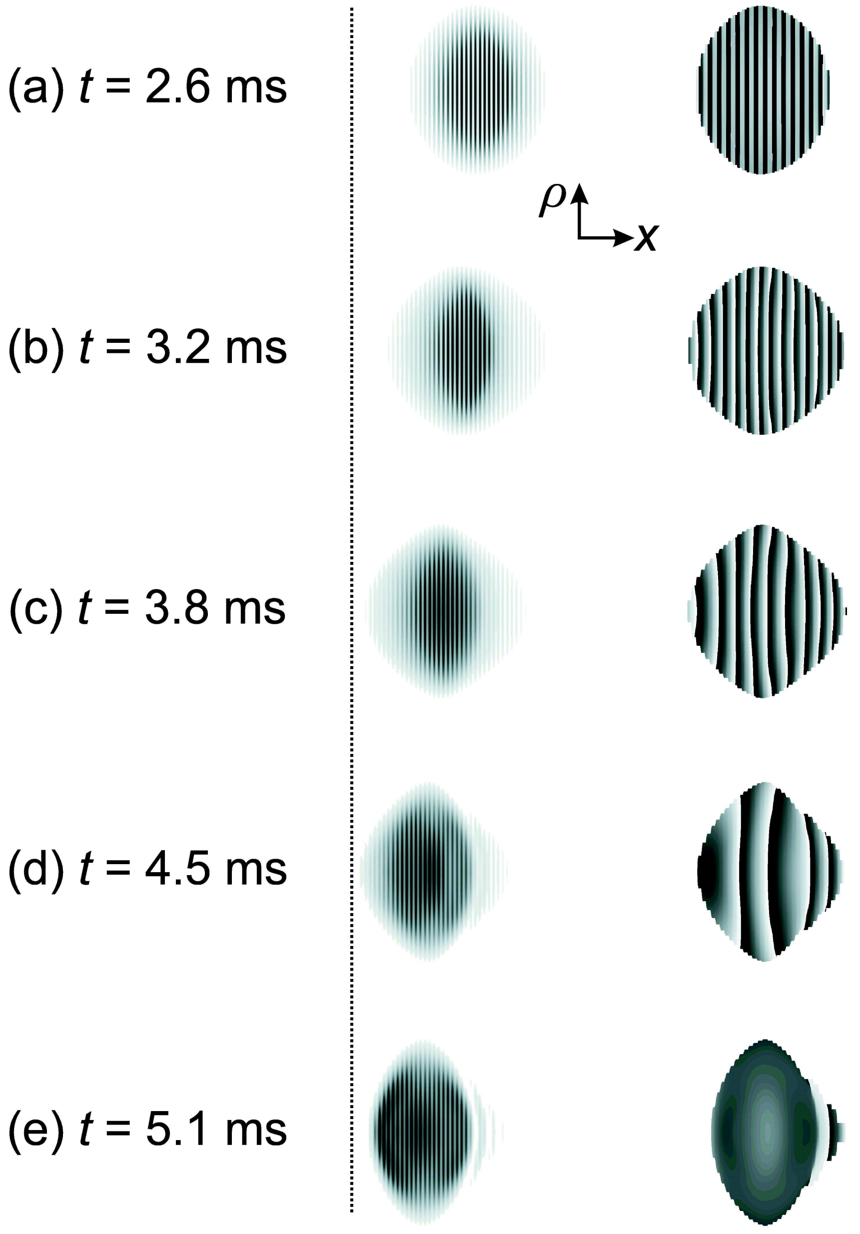

Figure 5.4: Left: Grey-scale plots of density (white = 0, black high) in $x - \rho$ plane (axes inset) for system A with $\Delta x = 25$ μm at various times t. Right: the corresponding phase profiles modulo 2π (white = 0, black = 2π, phase is not shown if corresponding probability density is less than 2% of maximum value). Dotted vertical line indicates the plane $x = -6$ μm. The range of t values $2.6 \leq t \leq 5.1$ ms corresponds to the time interval between the first Bragg reflection and the first trap reflection.

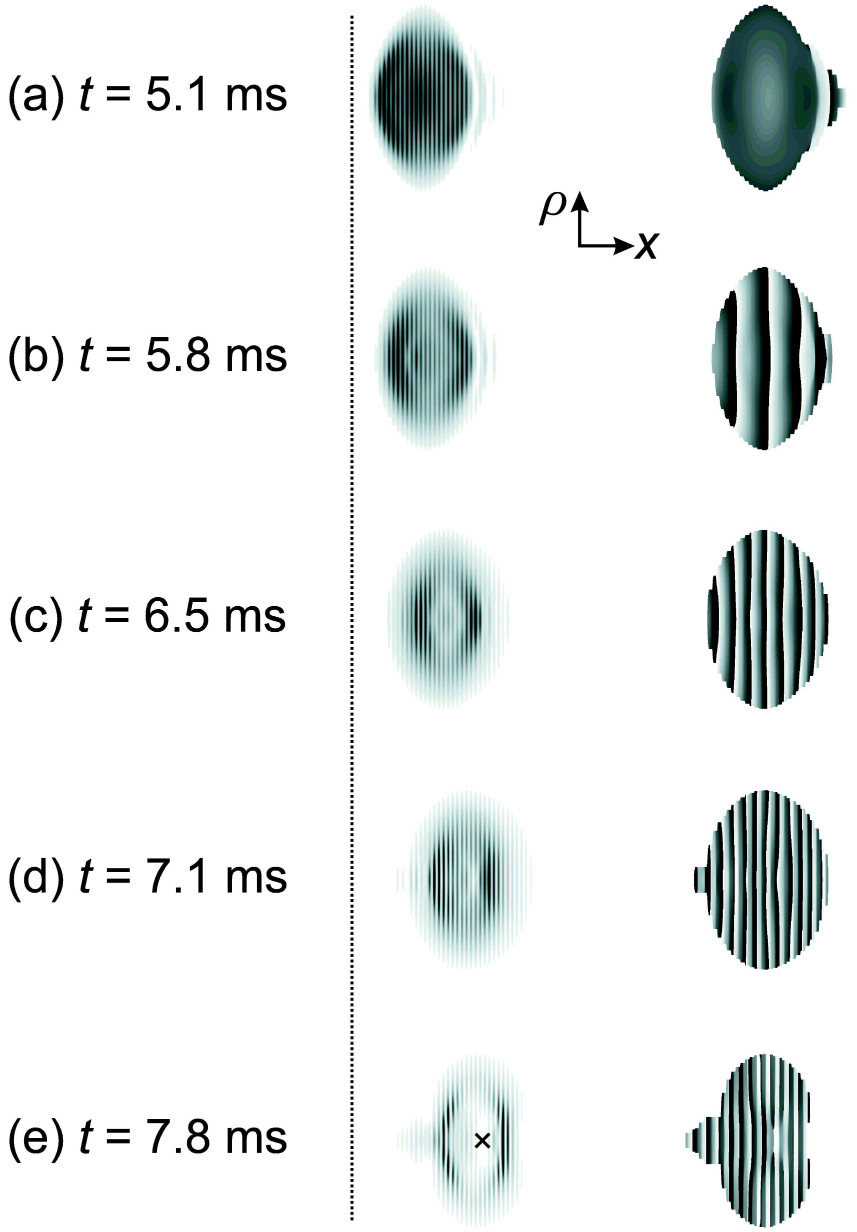

Figure 5.5: Left: Grey-scale plots of density (white = 0, black high) in $x - \rho$ plane (axes inset) for system A with $\Delta x = 25$ μm at various times t. Right: the corresponding phase profiles modulo 2π (white = 0, black = 2π, phase is not shown if corresponding probability density is less than 2% of maximum value). Dotted vertical line indicates the plane $x = -6$ μm. The range of t values $5.1 \leq t \leq 7.8$ ms corresponds to the time interval between the first trap reflection and the second Bragg reflection. The black cross in plot (e) marks the formation of the first significant soliton.

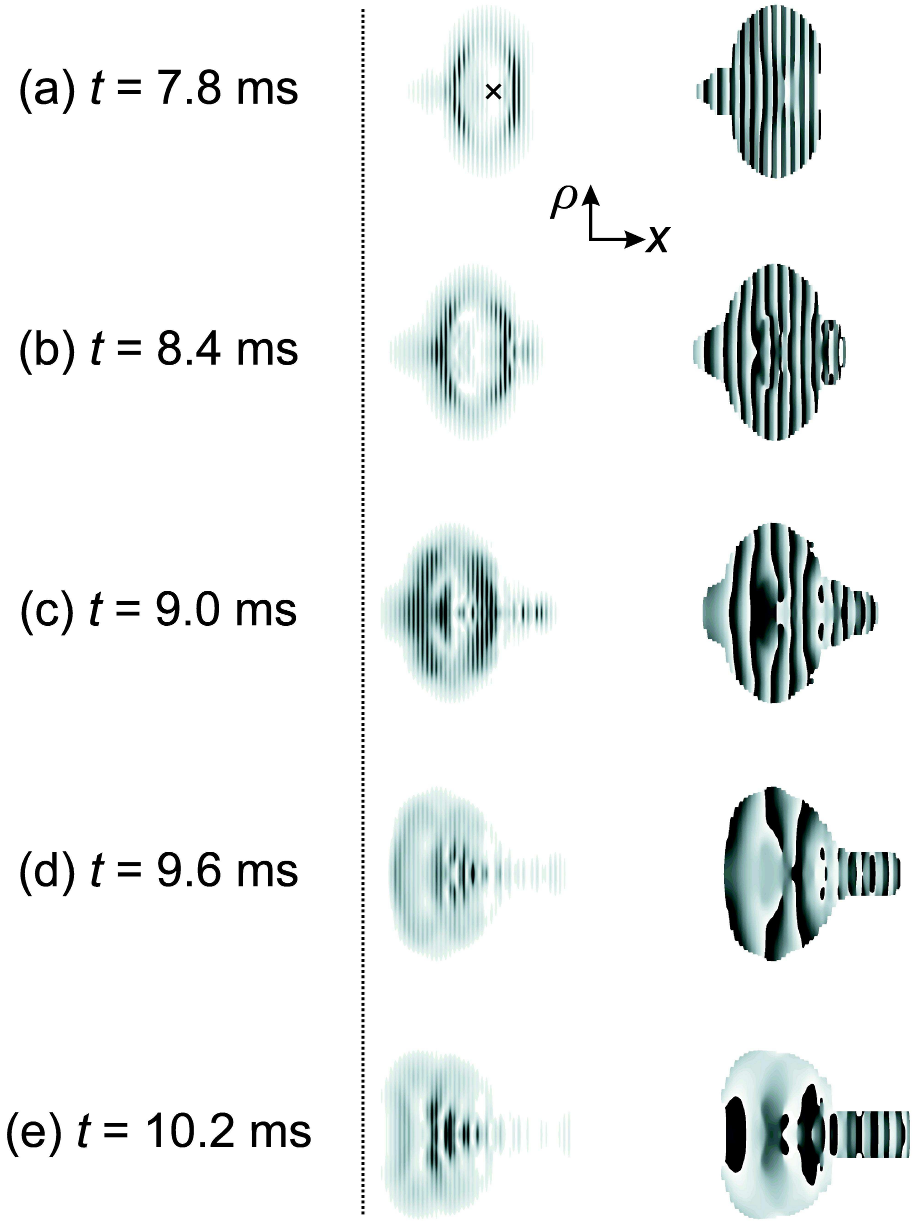

Figure 5.6: Left: Grey-scale plots of density (white = 0, black high) in $x - \rho$ plane (axes inset) for system A with $\Delta x = 25$ μm at various times t. Right: the corresponding phase profiles modulo 2π (white = 0, black = 2π, phase is not shown if corresponding probability density is less than 2% of maximum value). Dotted vertical line indicates the plane $x = -6$ μm. The range of t values $7.8 \leq t \leq 10.2$ ms corresponds to the time interval between the second Bragg reflection and the second trap reflection. The black cross in plot (a) marks the formation of the first significant soliton.

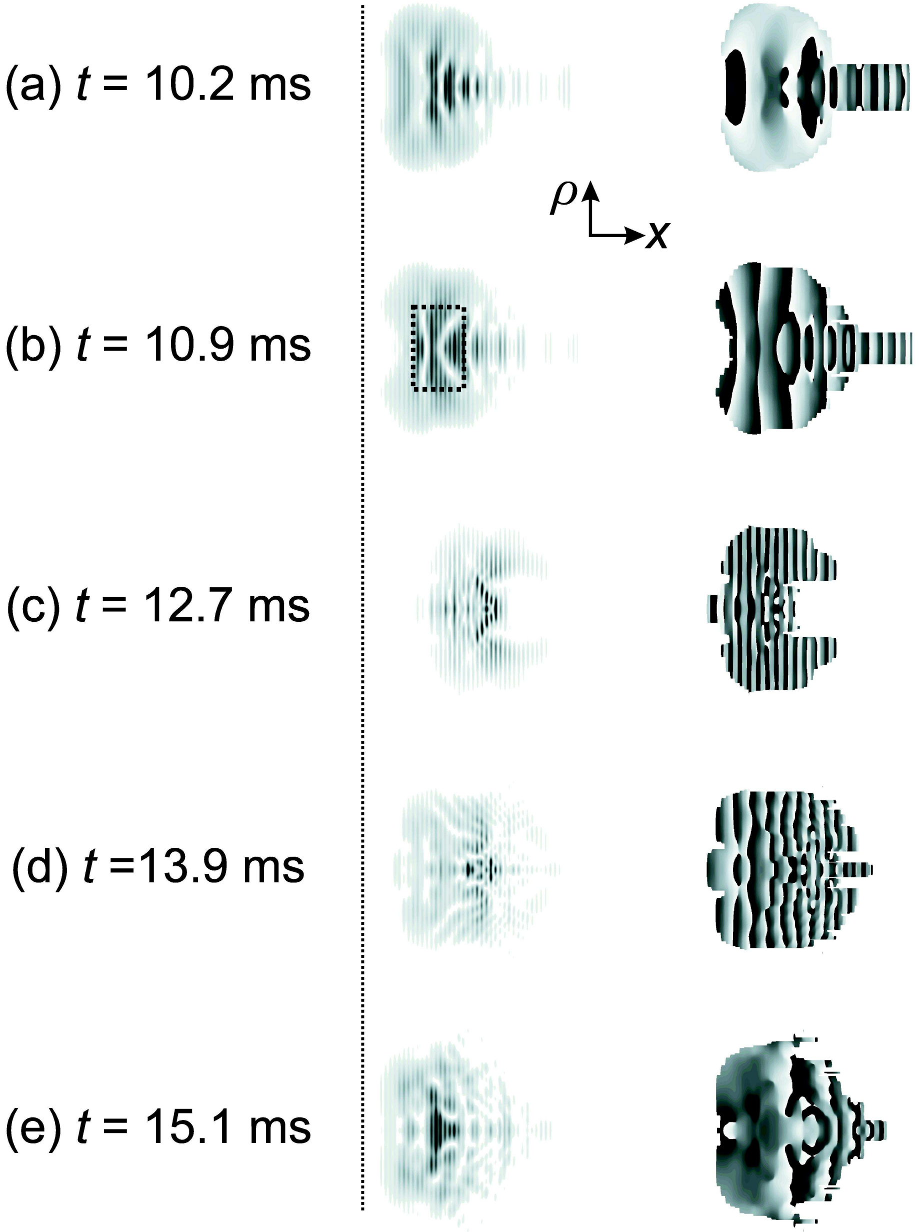

Figure 5.7: Left: Grey-scale plots of density (white = 0, black high) in $x - \rho$ plane (axes inset) for system A with $\Delta x = 25$ μm at various times t. Right: the corresponding phase profiles modulo 2π (white = 0, black = 2π, phase is not shown if corresponding probability density is less than 2% of maximum value). Dotted vertical line indicates the plane $x = -6$ μm. This figure shows further production of solitons and vortices, which creates a complex interacting system. The region contained within the dashed box in plot (b) is shown enlarged in figure 5.11.

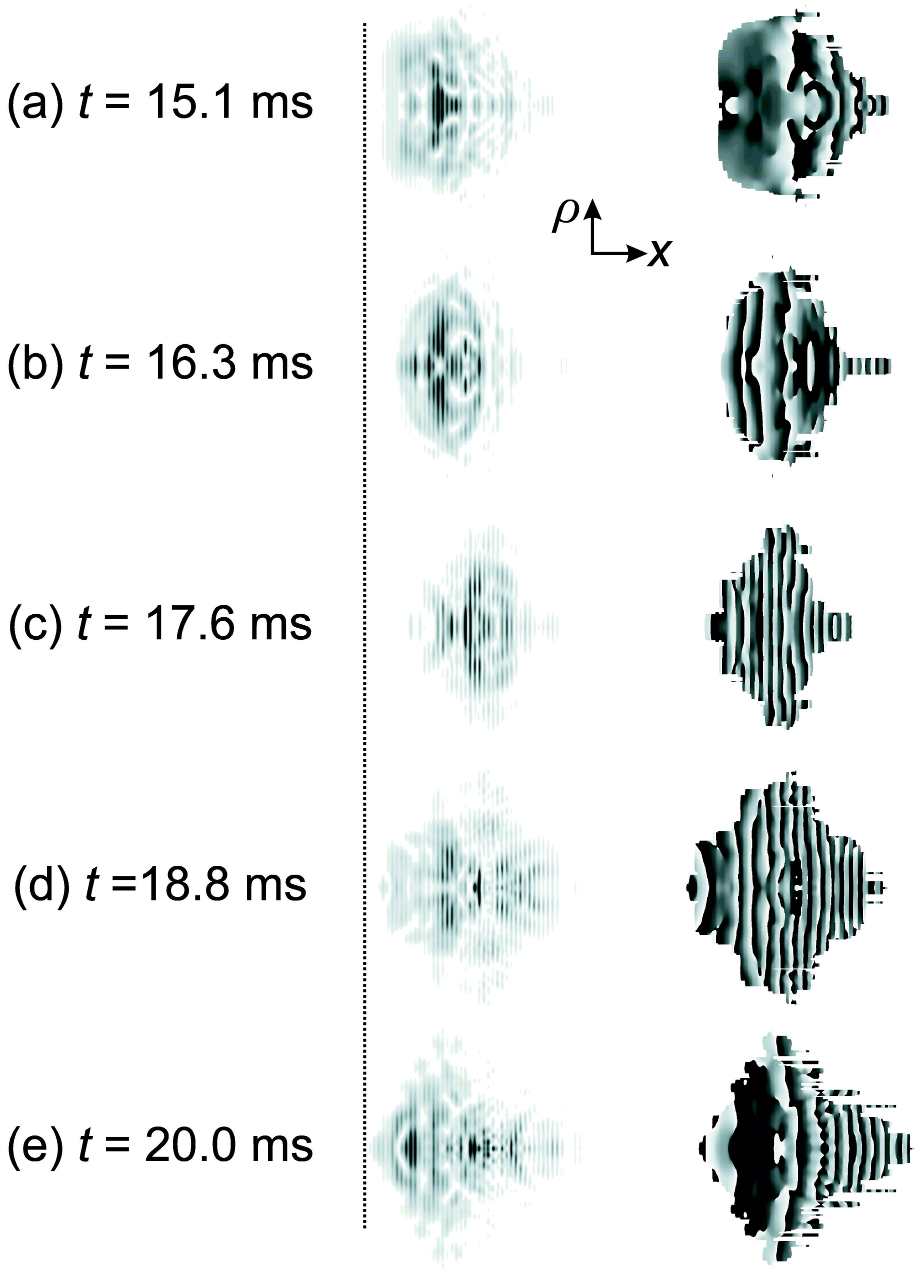

Figure 5.8: Left: Grey-scale plots of density (white = 0, black high) in $x - \rho$ plane (axes inset) for system A with $\Delta x = 25$ μm at various times t. Right: the corresponding phase profiles modulo 2π (white = 0, black = 2π, phase is not shown if corresponding probability density is less than 2% of maximum value). Dotted vertical line indicates the plane $x = -6$ μm. This figure shows that the condensate now contains many topological excitations, which leads to the eventual expansion and fragmentation of the condensate.

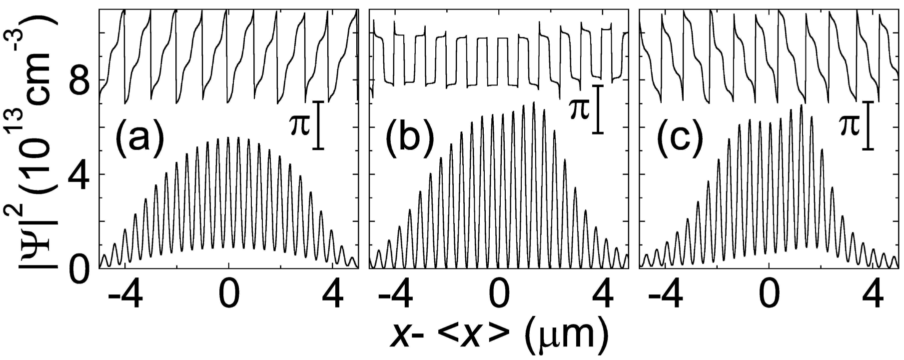

Figure 5.9: Density and phase profiles along $\rho = 0$ for the condensate in system A with $\Delta x = 25$ μm and $t = 2$ ms (a), 2.6 ms (b), 3 ms (c). In each figure, the lower curve is the density profile, and the upper curve shows the condensate phase modulo 2π, with vertical scale indicated by bars of length π.

BEC has a minimum value of $\sim 10^{13}$ cm^{-3}, which is approximately half that at $t = 0$ (figure 5.1(b)). The local velocity along the x−direction, $v_x = (\hbar/m)d\phi/dx$, is > 0 throughout the condensate. At the point of Bragg reflection (figure 5.9(b)), the density minima fall to zero at each peak in $V_{\mathrm{OL}}(x)$. At each zero, ϕ changes abruptly by π (upper curve in figure 5.9(b)). Away from the discontinuities, $d\phi/dx \simeq 0$, indicating that the BEC is at rest. This variation of density and phase demonstrates that a standing wave forms at the point of Bragg reflection. After reflection (figure 5.9(c)), the density minima rise away from zero and $d\phi/dx$ becomes negative for all x, as the condensate starts to move from right to left.

Figure 5.10 shows, for comparison, equivalent plots for a turning point bounded by the harmonic trap, when k_x passes through zero. The lower curves in figures 5.10(a), 5.10(b), and 5.10(c) show $|\Psi(x, 0, t)|^2$ just before ($t = 4.8$ ms), at ($t = 5.1$ ms), and just after ($t = 5.4$ ms) the first trap reflection. The upper curves show the wavefunction phase, $\phi(x)$, modulo 2π. The reader will notice that the density minima do not fall to zero, and there are no discontinuities in the phase at reflection. Instead, $\phi(x)$

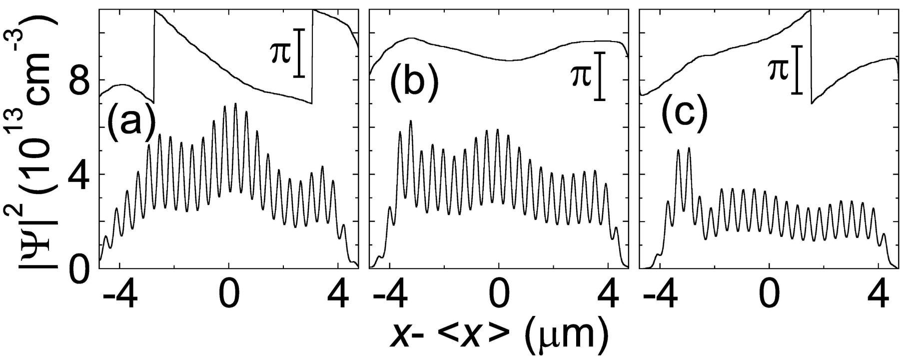

Figure 5.10: Density and phase profiles along $\rho = 0$ for the condensate in system A with $\Delta x = 25$ μm and $t = 4.8$ ms (a), 5.1 ms (b), 5.4 ms (c). In each figure, the lower curve is the density profile, and the upper curve shows the condensate phase modulo 2π, with vertical scale indicated by bars of length π.

is approximately constant across the condensate at the point of reflection, indicating that $d\phi/dx \simeq 0$, and hence indicating that the condensate is stationary. The standing wave shown in figure 5.9(b) is a consequence of Bragg reflection, and does not occur for trap reflection.

In recent experiments, laser illumination was used to produce similar individual density minima and/or π phase shifts, which subsequently evolved into dark solitons [47, 48, 63]. By analogy, the standing wave might be expected to generate a chain of stationary solitons. However, the reality is more complicated. The formation of the standing wave leads to a variety of behaviour, depending on the condensate density, the period of the Bloch oscillations, and the time elapsed since the trap displacement. In the case of a condensate in system A with a trap displacement of 25 μm, the standing wave formed on the first Bragg reflection (2.5 ms) produces no obvious solitons. Instead, after reflection, the density minima rise away from zero and $d\phi/dx$ becomes negative for all x, as the condensate starts to move from right to left, (see figure 5.9(c)). However, the subsequent Bragg reflection (7.5 ms) produces a large soliton in the centre of the condensate (marked by a cross in figure 5.5(e)).

After the second Bragg reflection, soliton production becomes more rapid. The wavefronts of the solitons are curved by refraction originating from the non-uniform density of the condensate [51], so they appear as white crescent shapes in figures 5.6-5.8. As the solitons curve, they become unstable and decay into vortex rings. This effect is known as *snake instability* [51]. An example of a vortex ring produced via this process is shown in figure 5.7(b). The vortex ring lies just inside the right-hand edge of the dashed box. The images in figure 5.7 are two-dimensional slices through the condensate, so the vortex ring appears as a pair of vortices with opposite circulation.

The region within the dashed box in figure 5.7(b) is enlarged in figure 5.11, which shows both the condensate density (figure 5.11(a)) and phase (figure 5.11(b)). The region contains the vortex ring in the centre of the condensate and the soliton immediately to the left of the vortex ring. The core of the vortex ring intersects the plane of the image at two points, which are enclosed by arrows. At these two points, there is a zero in the condensate density. Around these points, the phase changes continuously from 0 (white) to 2π (black), indicating quantised circulation in the direction of the arrows. The soliton is the white crescent on the left-hand side of figure 5.11(a), which represents a region of zero density. In figure 5.11(b), it appears as a curved line. This line marks an abrupt phase change from $3\pi/2$ (dark grey) on the left side of the line, to $\pi/2$ (light grey) on the right side of the line. The zero in the probability density and the π phase slip indicate that the soliton is stationary.

Vortex formation dissipates the energy associated with the centre-of-mass motion of the condensate, and hence damps the Bloch oscillations (figure 5.2(c)). After multiple Bragg reflections, many solitons and vortices

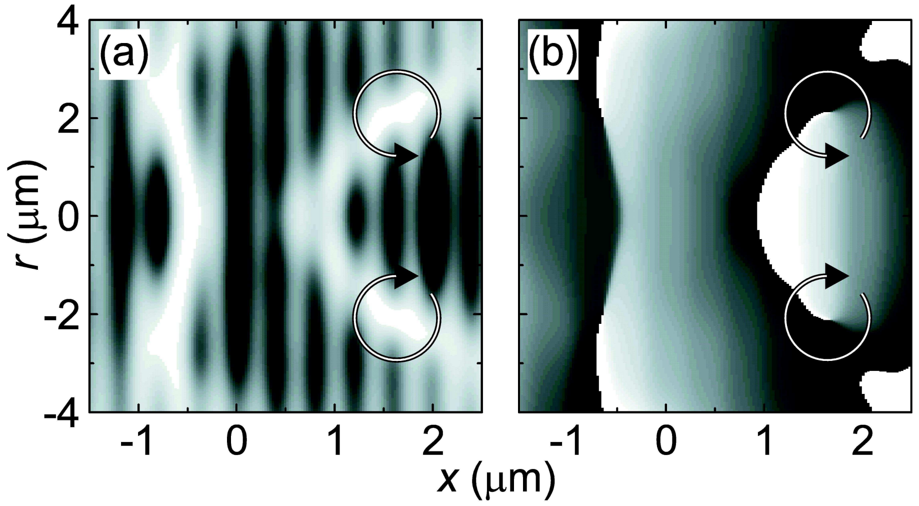

Figure 5.11: (a) Grey-scale plot of condensate density within dashed box in Fig. 5.7(b) (white = 0, black high). Arrows show direction of circulation around vortices. (b) Grey-scale plot of corresponding condensate phase (white = 0, black = 2π). $\Delta x = 25$ μm and $t = 10.9$ ms.

are produced, creating a complex interacting system (figure 5.7(c) to figure 5.8(e)). Eventually, the condensate becomes irregular and fragmented (figure 5.8), and loses all coherence in k-space (figure 5.2(d)). Consequently, the Bloch oscillations break down.

The reader should note that it is impossible for vortex rings to form in the two-dimensional simulations. In two dimensions, the solitons decay into pairs of vortices with opposite circulation. A brief representation of the two-dimensional results is shown in figures 5.12 and 5.13. The figures illustrate that the dynamics in two and three dimensions are very similar.

Figure 5.12 shows images of a two-dimensional condensate at key moments of the simulation. Firstly, figure 5.12(a) shows the ground state of the condensate in the combined potential of the optical lattice and undisplaced harmonic trap, at time $t = 0$ ms. The condensate density is modulated by the periodic potential of the optical lattice. Figure 5.12(b) shows the same condensate at time $t = 7.5$ ms, which corresponds to the point of the second

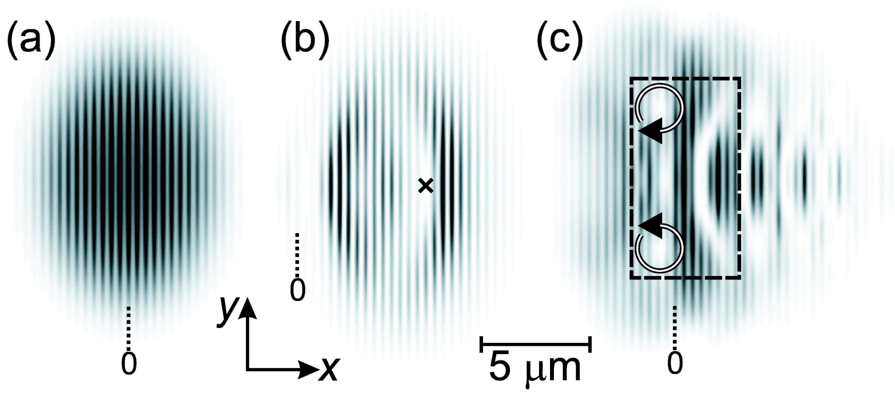

Figure 5.12: Grey-scale plot of density (white=0, black high) for system A in two dimensions with $\Delta x = 25$ μm and $t = 0$ ms (a), 7.5 ms (b), 10.7 ms (c). Vertical dotted lines indicate $x = 0$ in each case. Horizontal bar shows scale. Cross in (b) marks centre of a soliton. Region with dashed box is shown enlarged in figure 5.13. Arrows show direction of circulation around vortices.

Bragg reflection. As for the three-dimensional simulations (see figure 5.6(a)), a soliton has formed in the centre of the condensate. Figure 5.12(c) shows the condensate for $t = 10.7$ ms, by which time a pair of vortices has formed via the snake instability of a soliton. The vortices are situated inside the dashed box in figure 5.12(c), near the left-hand edge. They are enclosed by two circular arrows, which indicate the direction of the circulation. Note that the vortices have equal but opposite circulation. The dashed box also contains a soliton, near the right hand edge.

Figure 5.13 is an enlargement of both the density and phase profile of the condensate contained within the dashed box in figure 5.12(c). The topological excitations show the same features by which they are characterised in three dimensions, so figure 5.13 is qualitatively similar to the three-dimensional equivalent in figure 5.11. The vortices are zeros in the density, surrounded by circulating condensate. Around the vortices, the phase changes continuously from 0 (white) to 2π (black), indicating quan-

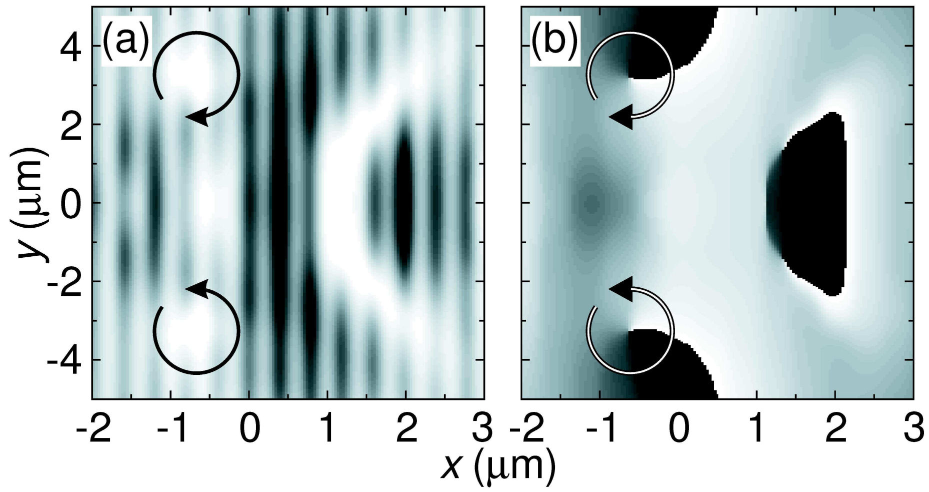

Figure 5.13: (a) Grey-scale plot of condensate density within dashed box in Fig. 5.12(c) (white = 0, black high). Arrows show direction of circulation around vortices. (b) Grey-scale plot of corresponding condensate phase (white = 0, black = 2π). $\Delta x = 25$ μm and $t = 10.7$ ms.

tised circulation in the direction of the arrows. The soliton is a line of zero condensate density, along which there is an abrupt phase change of π.

In the following chapter, Bloch oscillations and soliton and vortex production are studied for different parameter regimes, as realised in recent experiments [42, 69]. This throws more light on the mechanisms behind soliton and vortex production, and reveals the different factors which determine the behaviour of the condensate.

Chapter 6

Interpretation of experiments and explosive expansion of Bose-Einstein condensates

6.1 Introduction

In the previous chapter, a Bose-Einstein condensate was driven into Bloch oscillations, which were damped due to soliton and vortex formation. In this chapter, the same effects shall be studied for different parameter regimes, as realised in recent experiments. This reveals how the experiments can be understood, and identifies regimes in which vortices trigger explosive expansion of the condensate. Furthermore, the study of different experiments throws more light on the mechanisms behind soliton and vortex production, and the factors which determine the behaviour of the condensate.

6.2 Bloch oscillations of a Bose-Einstein condensate, as studied by Morsch et al.

Bloch oscillations of Bose-Einstein condensates have recently been observed by Morsch et al [42]. Their experiments differed from the system described in the previous chapter (system A) in that the condensates were not driven into oscillation by displacing the magnetic trap. Instead, the optical potential was accelerated in the direction of the lattice by detuning the lasers. This creates a constant force on the condensate in the rest frame of the atoms. By this method, the group successfully observed Bloch oscillations.

The method of Morsch et al. has both advantages and disadvantages compared to the method described in the previous chapter. One advantage is that the optical potential can in principle be accelerated arbitrarily fast and arbitrarily slowly. Hence there are no limits on the resulting force on the condensate, and consequently no limits on the period and amplitude of the Bloch oscillations. In contrast, for system A the condensate does not Bragg reflect below a critical trap displacement. Hence there is a lower limit on the force that may be applied to the condensate, and consequently an upper limit on the period and amplitude of the Bloch oscillations. The principal disadvantage of Morsch's method is that the accelerating optical lattice drags the condensate up one side of the magnetic trap. After sufficient time has elapsed, the magnetic trap begins to significantly distort the band structure. This ultimately leads to the breakdown of the Bloch oscillations.

Morsch's system is summarised in figure 6.1, and shall be referred to as system B. Figure 6.1(b) shows the density profile of Morsch's condensate along $\rho = 0$, which illustrates that its size and shape is very similar to the condensate in system A (see figure 5.1). As for system A, the condensate is composed of ^{87}Rb atoms, and is prepared in a one-dimensional OL and a harmonic magnetic trap. The number of atoms in the condensate has been slightly reduced to 10^4, and the trap frequencies have also dropped: $\omega_x = 2\pi \times 30$ rad s^{-1} and $\omega_y = \omega_z = 2\pi \times 32$ rad s^{-1}. As a result, the peak density of the condensate ground state is now 3.3×10^{13} cm^{-3}, compared to 4.3×10^{13} cm^{-3} for system A. Figure 6.1(a) shows the potential energy profile of the harmonic trap (dotted curve) along $\rho = 0$.

The optical lattice is also slightly different to that of system A. The depth of the optical lattice is now $V_0 = 2.32 E_R = 36.2$ peV, and its period is $d = \frac{\lambda}{2} = 390.0$ nm (see figure 6.1(a) for the potential energy profile of optical lattice along $\rho = 0$). As before, the band structure was calculated using Mathieu functions (see section 4.2). The energy range of the lowest band is indicated on figure 6.1(a) by a grey rectangle. As the figure shows, the band width of the lowest band is 0.54 E_R or 8.5 peV, slightly narrower than that of system A, which is 0.67 E_R or 10.0 peV.

The numerical techniques that were used to simulate the behaviour of system B are essentially exactly the same as those used to simulate the behaviour of system A. However, it is important to consider the frame of reference in which the Bloch oscillations are performed. In system A, the lattice is stationary, so the condensate performs Bloch oscillations in the stationary laboratory frame. However, in system B, the condensate performs Bloch oscillations in the rest frame of the lattice, which is accelerating with respect to the laboratory frame. Hence, if Bloch oscillations are to be observed, the motion of the lattice must be subtracted from the motion of the condensate.

This point has important consequences when calculating the k_x components of the condensate wavefunction in system B. A simple Fourier trans-

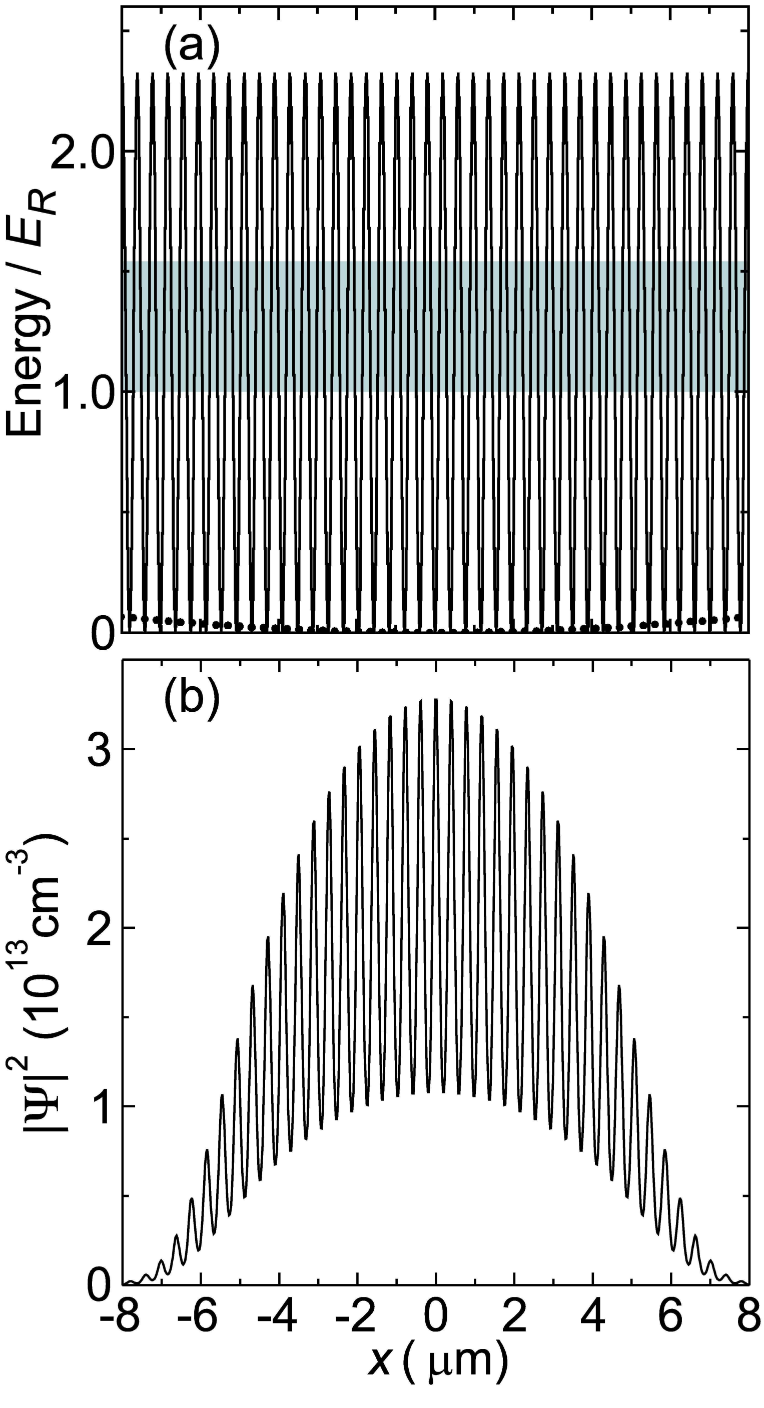

Figure 6.1: (a) Solid curve: potential energy profile of the OL in system B. Grey rectangle: energy range of the lowest energy band. Dotted curve: x-dependence of the harmonic potential energy for $\rho = 0$. (b) Initial density profile of the condensate in system B, along $\rho = 0$.

form, as done for system A (equation 5.57), will not generate the correct result. The problem is solved by considering the phase of the condensate wavefunction. Imagine a condensate which moved at the same velocity as the optical lattice. According to equation 3.49, it would have a phase gradient given by:

$$\frac{\hbar}{m}\frac{d\phi}{dx} = \text{Speed of OL} = \acute{a}t. \tag{6.1}$$

where $\acute{a}$ is the constant acceleration of the lattice. Integrating equation 6.1 with respect to x yields

$$\phi = \frac{m\acute{a}tx}{\hbar}\,. \tag{6.2}$$

This result can be used to transform the condensate wavefunction $\Psi\left(x,\rho,t\right)$ into an equivalent condensate wavefunction $\Psi'\left(x,\rho,t\right)$, whose velocity is equal to the original condensate's velocity relative to the accelerating lattice:

$$\Psi'\left(x,\rho,t\right) = \Psi\left(x,\rho,t\right)e^{-\frac{im\acute{a}tx}{\hbar}}\,. \tag{6.3}$$

Hence, the wavevector components of the condensate in the band of the OL are determined by evaluating:

$$f\left(k,t\right) = \int_{-\infty}^{\infty}\Psi\left(x,0,t\right)e^{-\frac{im\acute{a}tx}{\hbar}}e^{-ikx}dx. \tag{6.4}$$

6.2.1 Results for a lattice acceleration of 9.81 m/s^2

In order to demonstrate Bloch oscillations of a Bose-Einstein condensate experimentally Morsch et al. chose a lattice acceleration of 9.81 m/s^2. This section reproduces their results, and shows that their parameters were suitable for observing regular Bloch oscillations.

Figure 6.2 summarises the results of the simulation. Figure 6.2(a) shows the displacement of the condensate's mean position *with respect to the lattice.*

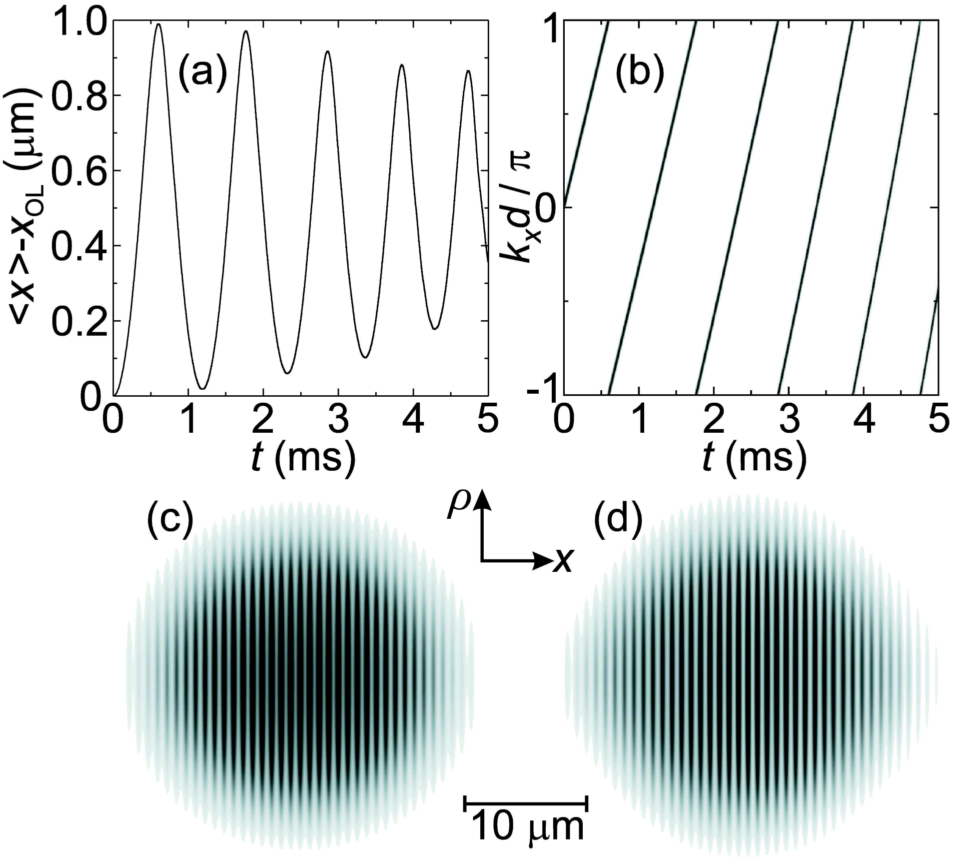

Figure 6.2: (a) $\langle x \rangle - x_{\mathrm{OL}}$ versus t for system B with $\acute{a} = 9.81$ m/s^2. (b) Corresponding grey-scale plot of $|f(k_x, t)|^2$ (white = 0, black high). (c) & (d) Corresponding grey-scale plots of density (white = 0, black high) in x-ρ plane (axes inset) for $t = 0$ ms & 5 ms respectively. Plots are symmetrical under reflection about $\rho = 0$. Horizontal bar shows scale.

To be precise, it shows the time evolution of $\langle x \rangle - x_{\mathrm{OL}}$, where x_{OL} is the displacement of the lattice, defined by

$$x_{\mathrm{OL}} = \frac{1}{2}\acute{a}t^2. \tag{6.5}$$

Figure 6.2(b) shows the corresponding time evolution of $|f(k_x, t)|^2$.

Figure 6.2(b) shows that the condensate reaches the Brillouin zone boundary at approximately 0.6 ms. As before, a standing wave is formed upon

Bragg reflection, which has a density node and associated π phase shift at each maximum in $V_{\rm OL}(x)$. But in this parameter regime, the standing wave has no obvious effect on the dynamics. After reflection, the density minima rise away from zero and the phase jumps become smaller and smoother. As this happens, the mean k_x value of the condensate continues to rise approximately linearly, and the condensate starts to move from right to left in the lattice frame. The condensate is performing Bloch oscillations.

The mean k_x value of the condensate then continues to rise approximately linearly until it reaches the Brillouin zone boundary for the second time at ~ 1.8 ms. Again the condensate undergoes Bragg reflection, and the standing wave has no apparent effect. The condensate Bragg reflects five times in total during the simulation, and yet no solitons are produced, and the k_x-distribution of the atoms remains very narrow (see figure 6.2(b)). Figures 6.2(c) and (d) show images of the condensate in the $x - \rho$ plane at the start ($t = 0$ ms) and end ($t = 5$ ms) of the simulation respectively. The images show that there has been almost no change in the internal structure of the condensate during the motion. The only discernible change is that the condensate has expanded slightly during the motion, due to the repulsive interactions.

However, even though there has been little change in the condensate wavefunction, the Bloch oscillations are not completely regular. By inspection of the $\langle x \rangle - x_{\rm OL}$ curve (figure 6.2(a)), the reader will notice that the period of the oscillations decreases during the motion. This is perhaps more obvious in figure 6.2(b), which shows that the condensate's mean k_x value rises at an increasing rate throughout the simulation. Furthermore, despite the fact that no excitations have been formed, the Bloch oscillations are clearly damped.

This behaviour is due to the magnetic trap. As an illustration of this effect, consider the example of the simulation summarised in figure 6.2. In this case, the lattice drags the condensate towards more negative values of x, hence pushing the condensate through the band in the positive k_x direction. As the condensate rides up the wall of the trap, it feels an additional force from the trap, pushing it back towards larger values of x, into the trap potential minimum. This *positive* force due to the trap *adds* to the force imparted by the accelerating lattice, so that the condensate feels an ever increasing total force driving it through k-space in the positive k_x direction. As a result, the period and amplitude of the oscillations become smaller and smaller. Eventually, this effect will cause the band to break, and the Bloch oscillations to break down. If the lattice were to be accelerated in the opposite direction, the two forces would add in the same way to drive the condensate in the negative k_x direction. Hence, in this scenario, the period and amplitude of the oscillations would also become smaller and smaller as the experiment progressed.

6.2.2 Results for a lattice acceleration of 0.25 m/s^2

Reducing the lattice acceleration reveals a new regime of condensate behaviour. At low accelerations, Bragg reflection seeds solitons which decay into vortex rings. This disrupts the condensate and damps the Bloch oscillations.

Figure 6.3 summarises the dynamics of the condensate for a lattice acceleration of 0.25 m/s^2. Figure 6.3(a) shows the time evolution of $\langle x \rangle - x_{\mathrm{OL}}$, where x_{OL} is the displacement of the lattice, and figure 6.3(b) shows the corresponding time evolution of $|f(k_x, t)|^2$. Inspection of figure 6.3(b) reveals that the condensate reaches the Brillouin zone boundary at approximately

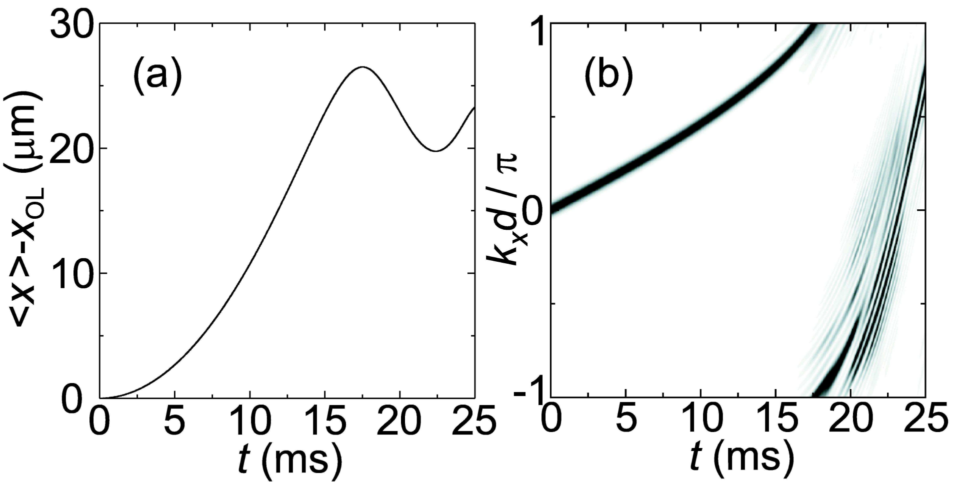

Figure 6.3: (a) $\langle x\rangle - x_{\mathrm{OL}}$ versus t for system B with $\acute{a} = 0.25$ m/s^2. (b) Corresponding grey-scale plot of $|f(k_x,t)|^2$ (white = 0, black high).

17.5 ms. As before, a standing wave is formed upon Bragg reflection, which has a density node and associated π phase shift at each maximum in $V_{\mathrm{OL}}(x)$. In this parameter regime, as for system A (see section 5.5), the standing wave seeds solitons, two examples of which are marked by crosses in figure 6.4(b). The solitons then swiftly decay via the snake instability into vortex rings. Figure 6.4(c) shows an image of the condensate containing two such vortex rings that have formed in the centre of the condensate. The core of each vortex ring cuts the x-ρ plane at two points, which are enclosed by arrows indicating the direction of circulation.

The formation of solitons and vortices disrupts the condensate, causing it to lose coherence in k-space. Figure 6.3(b) shows that the k_x−distribution of the atoms is initially very narrow, but spreads across approximately half the Brillouin zone after Bragg reflection. As a result, the Bloch oscillations are severely damped (see figure 6.3(a)).

The reader should also note that, as in section 6.2.1, the magnetic trap causes a distortion of the condensate's motion through the band. This is

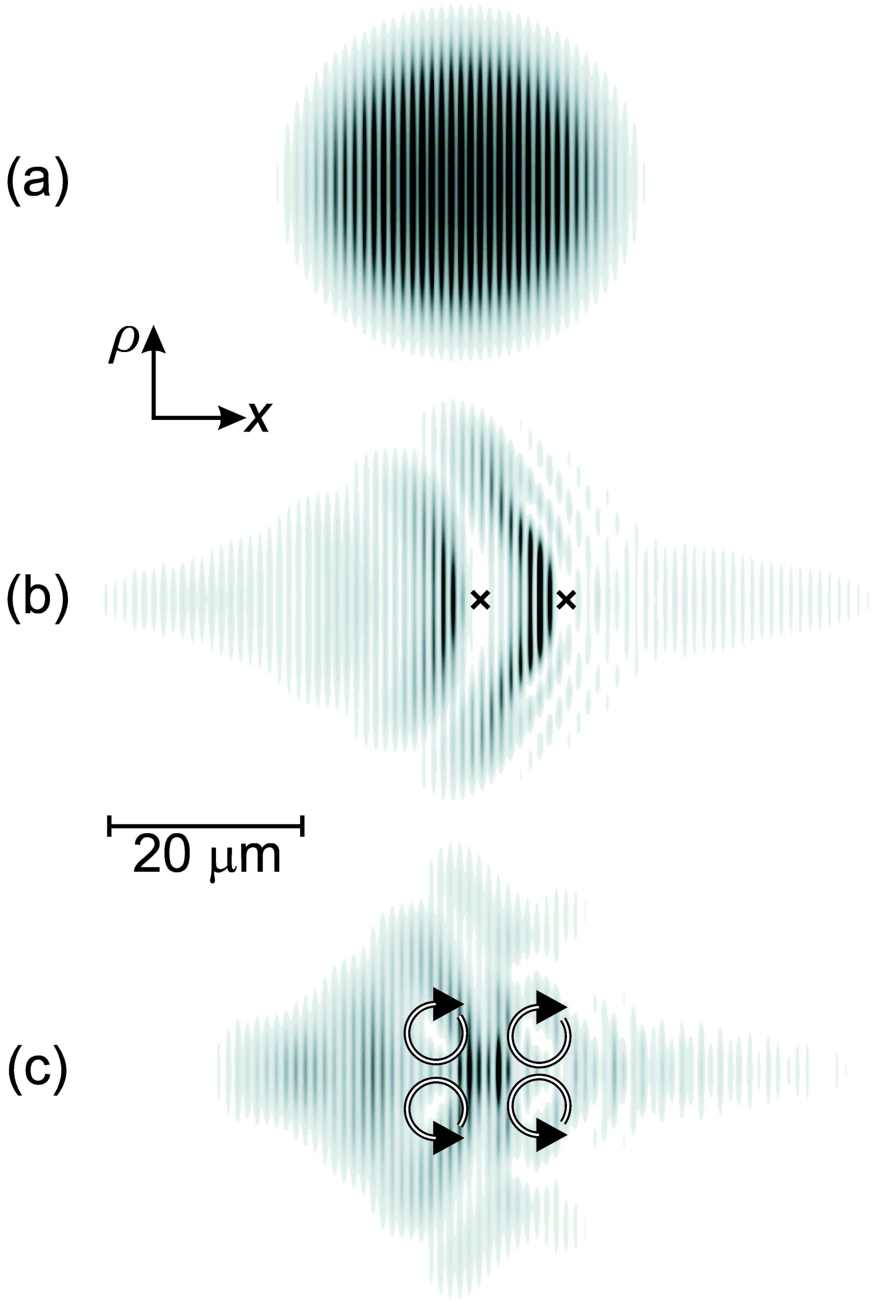

Figure 6.4: Grey-scale plots of density (white = 0, black high) in x-ρ plane (axes inset) for system B with $\acute{a} = 0.25$ m/s^2 and $t = 0$ ms (a), 19.9 ms (b), 21.9 ms (c). Plots are symmetrical under reflection about $\rho = 0$. Horizontal bar shows scale. Crosses in (b) mark centre of solitons. Arrows show direction of circulation around vortices.

reflected in figure 6.3(b), which shows that the condensate's mean k_x value rises at an increasing rate throughout the simulation.

6.3 Dynamics of a Bose-Einstein condensate in an optical lattice, as studied by Burger et al.

Burger et al. [69] studied the dynamics of a Bose-Einstein condensate in an optical lattice, using the same method as described in the previous chapter. However, the parameters that the group chose were very different. Burger et al. explained their results in terms of a Landau instability of the condensate. The theoretical work in this section disagrees with Burger's interpretation, and instead suggests that the instability of the condensate is due to rapid vortex production, leading to explosive expansion of the condensate.

The system studied in this section is qualitatively the same as the system studied in chapter 5 (system A). However, the frequencies of the harmonic trap are now adjusted to create a long thin condensate: $\omega_x = 2\pi \times 8.7$ rad s^{-1} and $\omega_y = \omega_z = 2\pi \times 90$ rad s^{-1}. Furthermore, the total number of atoms N_A is greatly increased to 3×10^5, with the result that the peak density of the ground state increases to $\sim 1.5 \times 10^{14}$cm^{-3}. The optical lattice is the same as for system A (see section 5.1 and figure 5.1(a)). Figure 6.5(a) shows the resulting ground state of the trap and optical lattice under these conditions. This set of parameters corresponds to Burger's recent experiments [69], and shall be referred to as system C.

This section examines a simulation in which the trap is displaced by 150 μm. The critical trap displacement above which Bragg reflection occurs is 86 μm (see equation 5.4), so this is well within the Bloch oscillation regime. Although the trap displacements considered here are much greater than those

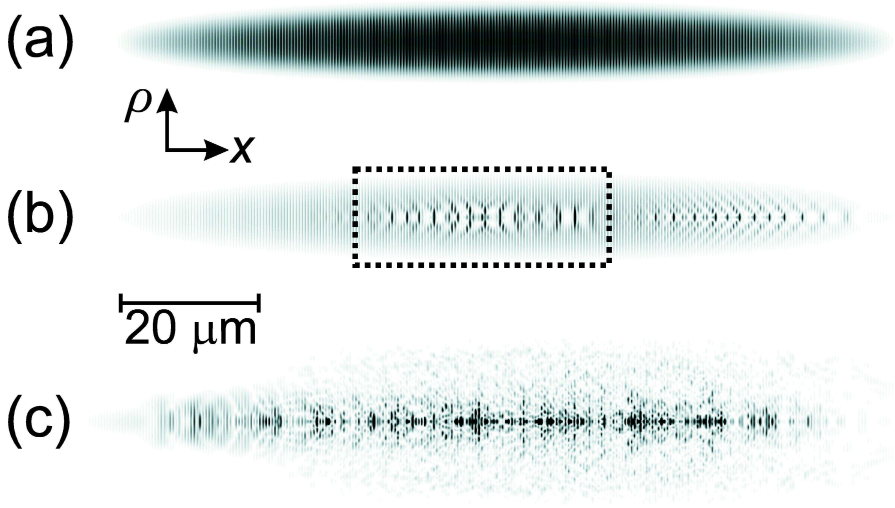

Figure 6.5: Grey-scale plots of density (white = 0, black high) in the x-ρ plane (axes inset) for system C with $\Delta x = 150$ μm and $t = 0$ ms (a), 14.0 ms (b), and 18.0 ms (c). Plots are symmetrical under reflection about $\rho = 0$. Horizontal bar shows scale. Region within dashed box in (b) is shown in figure 6.8(a).

considered for system A, the resulting Bloch oscillations have longer periods because the frequency of the trap in the x-direction is much smaller. The results of section 6.2.2 suggest that slow Bloch oscillations promote soliton and vortex production at the first Bragg reflection. Hence this parameter regime might be expected to show rapid generation of excitations and a resulting breakdown of the Bloch oscillations.

Furthermore, the higher density of the condensate in system C might *also* be expected to promote soliton and vortex production. In order to explain this, consider system A for a trap displacement of 25 μm (see section 5.5). At the point of the first Bragg reflection, the local mean atom density $\simeq 3 \times 10^{13}$ cm^{-3} near the centre of the condensate (see figure 5.9(b)). Consequently, the healing length is approximately 0.5 μm $\simeq 1.25d$, which infers that a soliton would have a width $w \simeq 2\xi \simeq 2.5d$. Since this width is greater than the separation of density minima and phase slips in the standing wave, it is awkward for solitons to form. If a soliton is to form, it must straddle several OL periods, and hence extend across several density nodes and phase slips in the standing wave.

It might be expected that solitons would form more readily if $w \lesssim d$. This can be achieved in a high density condensate, which has a small healing length and consequently a small soliton width w. In the case of system C, the density is high enough such that the soliton width closely matches the separation of density minima and phase slips in the standing wave. Hence, the system might be expected to show rapid soliton and vortex production.

Figures 6.6(a) and 6.6(b) show the time evolution of $\langle x \rangle$ and $|f(k_x,t)|^2$ for a trap displacement of 150 μm. Figure 6.6(b) shows that the condensate reaches the Brillouin zone boundary at approximately 13 ms. As for system A, a standing wave is formed upon Bragg reflection, which has a density node and associated π phase shift at each maximum in $V_{\mathrm{OL}}(x)$. But in this case, the local mean atom density at Bragg reflection is $\simeq 1.6 \times 10^{14}$ cm^{-3} near the centre of the condensate. Consequently, the healing length is approximately 0.2 μm $\simeq 0.5d$, which infers that a soliton would have a width $w \simeq 2\xi \simeq d$. Hence the condition $w \lesssim d$ is satisfied, and the theorist would expect to observe rapid soliton production.

As a result of these factors, Bragg reflection causes the self-assembly of ~ 10 stationary solitons, which form a chain across the central third of the condensate. Figure 6.5(b) shows the compact cigar-shaped density profile of the condensate just after the first Bragg reflection. The region within the box is shown enlarged in figure 6.8(a), which reveals ~ 5 stationary solitons (extended white areas).

Figures 6.7 and 6.8 show several stages in the formation of the solitons, and their subsequent decay into vortex rings. Figure 6.7 shows depressions

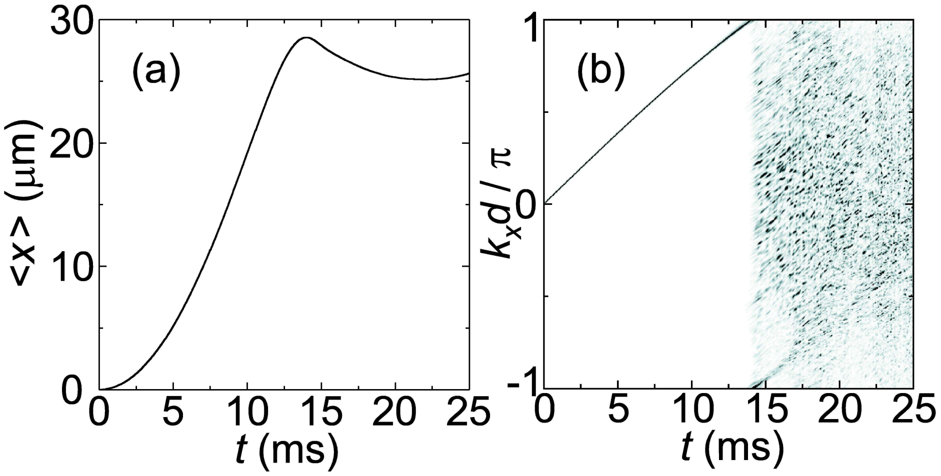

Figure 6.6: (a) $\langle x \rangle$ versus t for system C with $\Delta x = 150$ μm. (b) Corresponding grey-scale plot of $|f(k_x, t)|^2$ (white = 0, black high).

forming in the condensate, which evolve into the first solitons. Figure 6.8(a) is the best image of the soliton chain. Unfortunately, it is difficult to find a clear image of the chain of solitons because they decay so rapidly into vortex rings. In figure 6.8(a), some of the solitons have already begun to break up, whilst others are still forming. Since their decay is so rapid, the solitons create a chain of vortex rings (seen most clearly in figures 6.8(b-c)), which form a complex interacting system (see figure 6.8(c)).

The interactions now create a large internal strain, which causes the condensate to explode laterally (perpendicular to the x-axis), resulting in the diffuse and fragmented atom density profile shown in figure 6.5(c). The explosion has a dramatic effect on the k_x–distribution of the atoms (figure 6.6(b)), which is initially extremely narrow but, at the point of Bragg reflection, spreads through the whole Brillouin zone. The condensate has lost all coherence in k-space, so does not perform Bloch oscillations. Once the condensate has reached the Brillouin zone boundary and performed the first half of a Bloch oscillation, its centre-of-mass remains approximately sta-

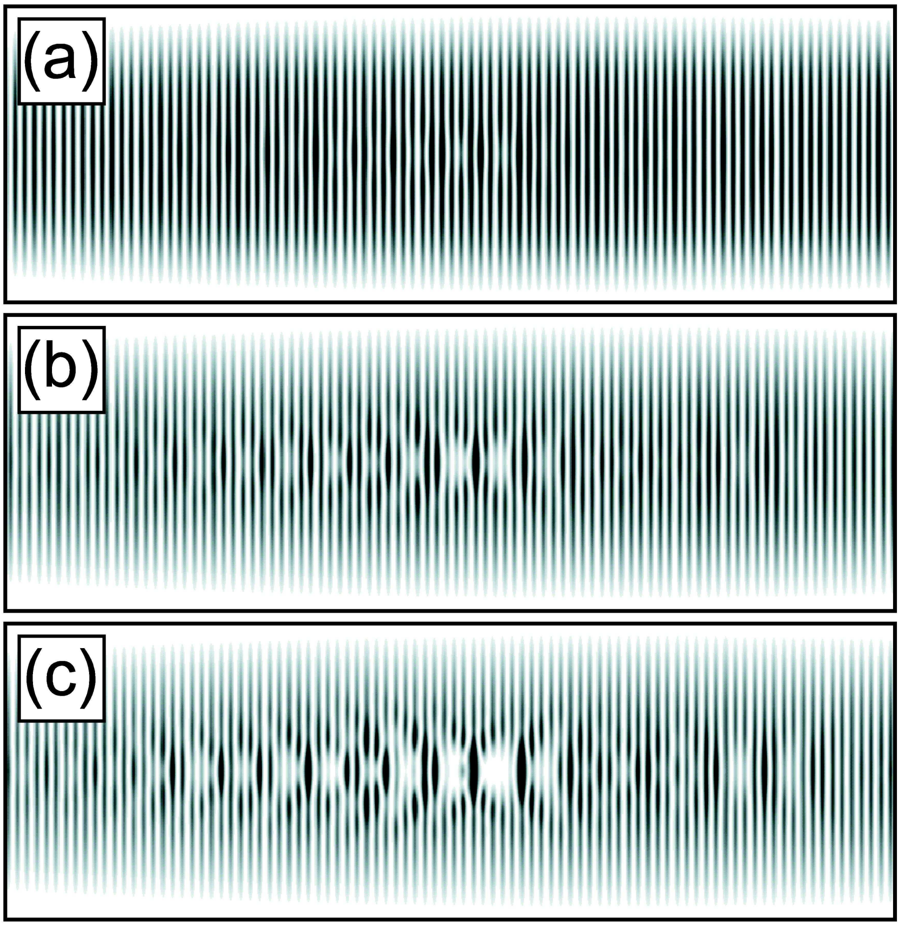

Figure 6.7: Grey-scale plots of density in central third of the condensate (white = 0, black high) in the x-ρ plane for system C with $\Delta x = 150$ μm and $t = 13.4$ ms (a), 13.6 ms (b), and 13.8 ms (c).

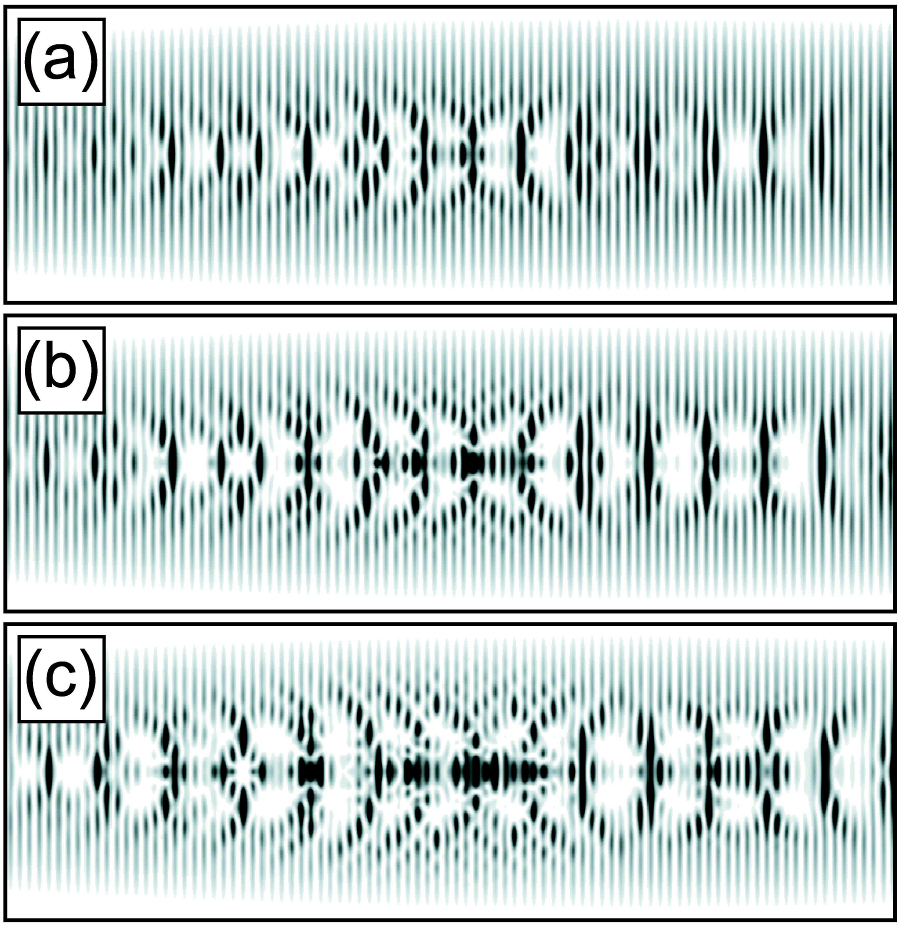

Figure 6.8: Grey-scale plots of density in central third of the condensate (white = 0, black high) in the x-ρ plane for system C with $\Delta x = 150$ μm and $t = 14.0$ ms (a), 14.2 ms (b), and 14.4 ms (c). Figure (a) corresponds to the region within the dashed box in figure 6.5(b).

tionary (see figure 6.6(a)). This provides an alternative explanation to the damping observed by Burger et al. [69], who explain it in terms of Landau instability.

Chapter 7

Conclusion

7.1 Summary and overview

This thesis has used cold atoms in optical lattices as the basis for theoretical studies of quantum chaos and Bose-Einstein condensation. The results have illustrated that optical lattices are an extremely versatile tool for probing aspects of solid state physics, atomic physics and quantum optics. Furthermore, optical lattices offer unprecedented experimental control, so they represent a unique opportunity to explore effects, such as Bloch oscillations, which have previously been detected only indirectly.

Chapter 4 studied quantum chaos in a system of atoms in the lowest energy band of an optical lattice. In this example, there were different energy-momentum dispersion relations for motion parallel and perpendicular to the axis of the optical lattice, thereby inducing mixed stable-chaotic dynamics. The system was described from a both a semi-classical and quantum-mechanical perspective, and the two theories were related via phase space analysis, wavefunction scarring, and fluctuations in the energy level spectrum. This system is unique because the chaos originates from an intrinsically quantum-mechanical effect: the energy band of the optical lattice.

Chapters 5 and 6 examined the motion of Bose-Einstein condensates in optical lattices. The results showed that Bose-Einstein condensates can demonstrate effects which are normally associated with solid state physics, such as Bragg reflection and Bloch oscillations. It was also shown how these processes may generate solitons and vortices, depending on the system parameters.

The topic of Bose-Einstein condensates in optical lattices was studied via the examples of three systems, A, B and C, of which B and C were realised in recent experiments. The results revealed how the experiments can be understood, and identified regimes in which vortices trigger explosive expansion of the condensate. The study of three different condensate systems provides a comprehensive picture of the different factors which determine the behaviour of condensates in optical lattices. The study of system B showed that soliton production is promoted by slow Bloch oscillations, and the study of system C showed that solitons are more readily formed in high density condensates. However, the results for system A showed that short period Bloch oscillations can produce solitons in condensates of low density, if the condensate becomes sufficiently disrupted by multiple Bragg reflections.

7.2 Suggestions for further study

There is considerable current interest in the possible connections between Bose-Einstein condensates and quantum chaos [71]. Since the systems discussed in chapters 4, 5 and 6 are similar, it may be possible to combine the ideas in this thesis in order to create a system suitable for exploring quantum chaos in Bose-Einstein condensates. Indeed, in chapter 4 it was demonstrated that under certain conditions the collective dynamics of a condensate in an optical lattice are very similar to those of a point-like particle obeying semi-classical laws of motion. By analogy, the onset of chaos for single atoms in an optical lattice may also be manifest in the collective time-dependent dynamics and excitations of a condensate.

Chapter 6 presented simulations of experiments performed by Morsch et al [42]. This group and the author are now in contact, and have shared their results and ideas. It is hoped that the collaboration will continue in the future, so that experimental results can confirm the predictions made in chapters 5 and 6, and stimulate further theoretical work.

Appendix A

Derivation of equations 4.60, 4.61 and 4.62

The starting point for the derivation is equation 4.59, reproduced below:

$$E = E_b\left(p_x\right) + \frac{p_z^2}{2m} + \frac{m}{2}\left(\omega_x^2 x_t^2 + \omega_z^2 z_t^2\right). \tag{A.1}$$

The quantities x_t and z_t are then replaced by terms in x and z, using the relationships given in equation 4.3:

$$\begin{aligned} E = E_b\left(0\right) + \frac{p_z^2}{2m} + \frac{m}{2}\left[\omega_x^2\left(x^2\cos^2\theta + z^2\sin^2\theta + 2xz\cos\theta\sin\theta\right) + \right. \\ \left. \omega_z^2\left(x^2\sin^2\theta + z^2\cos^2\theta + 2xz\cos\theta\sin\theta\right)\right]. \end{aligned} \tag{A.2}$$

(N.B. The term $E_b\left(p_x\right)$ has been replaced by $E_b\left(0\right)$ since p_x is set to zero when plotting the Wigner functions.) Rearranging equation A.2 yields:

$$\begin{aligned} x^2\left[\frac{m}{2}\left(\omega_x^2\cos^2\theta + \omega_z^2\sin^2\theta\right)\right] + x\left[mz\cos\theta\sin\theta\left(\omega_x^2 - \omega_z^2\right)\right] + \\ E_b\left(0\right) - E + \frac{p_z^2}{2m} + \frac{mz^2}{2}\left(\omega_x^2\sin^2\theta + \omega_z^2\cos^2\theta\right) = 0. \end{aligned} \tag{A.3}$$

This is a quadratic equation in x, which can be solved in the usual way to obtain equation 4.60, reproduced below:

$$x = \frac{mz\cos\theta\sin\theta\left(\omega_z^2-\omega_x^2\right)\pm\sqrt{\frac{m}{2}\left(\omega_x^2\cos^2\theta+\omega_z^2\sin^2\theta\right)\left(E-E_b\left(0\right)-\frac{p_z^2}{2m}\right)}}{m\left(\omega_x^2\cos^2\theta+\omega_z^2\sin^2\theta\right)}. \tag{A.4}$$

Now consider equation 4.57, shown below:

$$\hbar\frac{dk_x}{dt} = -m\omega_x^2 x_t\cos\theta + m\omega_z^2 z_t\sin\theta. \tag{A.5}$$

Again, the quantities x_t and z_t are replaced by the expressions in x and z given in equation 4.3:

$$\hbar\frac{dk_x}{dt} = -m\omega_x^2\cos\theta\left(x\cos\theta+z\sin\theta\right)+m\omega_z^2\sin\theta\left(-x\sin\theta+z\cos\theta\right). \tag{A.6}$$

Rearranging yields

$$\hbar\frac{dk_x}{dt} = -mx\left(\omega_x^2\cos^2\theta+\omega_z^2\sin^2\theta\right)+mz\cos\theta\sin\theta\left(\omega_z^2-\omega_x^2\right). \tag{A.7}$$

But, from equation A.4,

$$\begin{aligned} mx\left(\omega_x^2\cos^2\theta+\omega_z^2\sin^2\theta\right) &= mz\cos\theta\sin\theta\left(\omega_z^2-\omega_x^2\right) \\ &\pm\sqrt{\frac{m}{2}\left(\omega_x^2\cos^2\theta+\omega_z^2\sin^2\theta\right)\left(E-E_b\left(0\right)-\frac{p_z^2}{2m}\right)}. \end{aligned} \tag{A.8}$$

The entire right-hand side of equation A.8 is now substituted for the term

$mx\left(\omega_x^2\cos^2\theta+\omega_z^2\sin^2\theta\right)$ in equation A.7:

$$\hbar\frac{dk_x}{dt}=\mp\sqrt{\frac{m}{2}\left(\omega_x^2\cos^2\theta+\omega_z^2\sin^2\theta\right)\left(E-E_b\left(0\right)-\frac{p_z^2}{2m}\right)}\ . \tag{A.9}$$

Hence, for the smaller value of x

$$\hbar\frac{dk_x}{dt}=\sqrt{\frac{m}{2}\left(\omega_x^2\cos^2\theta+\omega_z^2\sin^2\theta\right)\left(E-E_b\left(0\right)-\frac{p_z^2}{2m}\right)}\ , \tag{A.10}$$

and for the larger value of x

$$\hbar\frac{dk_x}{dt}=-\sqrt{\frac{m}{2}\left(\omega_x^2\cos^2\theta+\omega_z^2\sin^2\theta\right)\left(E-E_b\left(0\right)-\frac{p_z^2}{2m}\right)}\ . \tag{A.11}$$

Hence equations 4.61 and 4.62 are obtained.

Appendix B

Derivation of equation 4.79 from equation 4.78

The starting point for the derivation is equation 4.78, reproduced below:

$$D_{AV}(E) = \frac{1}{h^2} \int_{p_z} \int_{p_x} \int_{z_t} \int_{x_t} \delta \left\{ E - E_b(p_x) - \frac{p_z^2}{2m} - \frac{1}{2} m \omega_x^2 x_t^2 - \frac{1}{2} m \omega_z^2 z_t^2 \right\} dx_t \, dz_t \, dp_x \, dp_z. \quad \text{(B.1)}$$

Firstly, the order of the integrals is changed, and the limits of the integration over p_z are set:

$$D_{AV}(E) = \frac{2}{h^2} \int_{p_x} \int_{x_t} \int_{z_t} \int_{0}^{p_{z_{\max}}} \delta \left\{ E - E_b(p_x) - \frac{p_z^2}{2m} - \frac{m \omega_x^2 x_t^2}{2} - \frac{m \omega_z^2 z_t^2}{2} \right\} dp_z \, dz_t \, dx_t \, dp_x, \quad \text{(B.2)}$$

where $p_{z_{\max}}$ is the maximum possible value of p_z at a particular energy E, i.e.

$$p_{z_{\max}} = \sqrt{2m(E - E_b(0))}. \quad \text{(B.3)}$$

Defining

$$u = -\frac{p_z^2}{2m}\,, \tag{B.4}$$

it follows that

$$du = -\frac{p_z}{m} dp_z, \tag{B.5}$$

and

$$p_z = \sqrt{-2mu}\,, \tag{B.6}$$

hence

$$dp_z = -\frac{m}{\sqrt{-2mu}} du. \tag{B.7}$$

Equation B.2 is now rewritten in terms of u:

$$\begin{aligned} D_{AV}(E) = {} & \frac{2}{h^2} \int_{p_x} \int_{x_t} \int_{z_t} \int_0^{-\frac{p_{z\max}^2}{2m}} \\ & \delta\left\{u - \left(E_b(p_x) + \frac{m\omega_x^2 x_t^2}{2} + \frac{m\omega_z^2 z_t^2}{2} - E\right)\right\} \frac{-m}{\sqrt{-2mu}} du\, dz_t\, dx_t\, dp_x. \end{aligned} \tag{B.8}$$

Rearranging equation B.8 yields

$$\begin{aligned} D_{AV}(E) = {} & \frac{2m}{h^2} \int_{p_x} \int_{x_t} \int_{z_t} \int_{-\frac{p_{z\max}^2}{2m}}^0 \\ & \delta\left\{u - \left(E_b(p_x) + \frac{m\omega_x^2 x_t^2}{2} + \frac{m\omega_z^2 z_t^2}{2} - E\right)\right\} \frac{du}{\sqrt{-2mu}} dz_t\, dx_t\, dp_x. \end{aligned} \tag{B.9}$$

The integral with respect to u can now be performed, giving

$$D_{AV}(E) = \frac{2m}{h^2} \int_{p_x} \int_{x_t} \int_{z_t} \frac{dz_t\, dx_t\, dp_x}{\sqrt{-2m\left(E_b(p_x) + \frac{m\omega_x^2 x_t^2}{2} + \frac{m\omega_z^2 z_t^2}{2} - E\right)}}\,. \tag{B.10}$$

Rearranging equation B.10 gives

$$D_{AV}\left(E\right) = \frac{2m}{h^2}\int_{p_x}\int_{x_t}\int_{z_t}$$

$$\frac{dz_t\, dx_t\, dp_x}{\sqrt{m^2\omega_z^2\left(\frac{1}{m^2\omega_z^2}\right)\left(2mE - 2mE_b\left(p_x\right) - m^2\omega_x^2 x_t^2 - m^2\omega_z^2 z_t^2\right)}}\,, \qquad \text{(B.11)}$$

and hence

$$D_{AV}\left(E\right) = \frac{2}{h^2\omega_z}\int_{p_x}\int_{x_t}\int_{z_t}\frac{dz_t\, dx_t\, dp_x}{\sqrt{\frac{1}{m^2\omega_z^2}\left(2mE - 2mE_b\left(p_x\right) - m^2\omega_x^2 x_t^2\right) - z_t^2}}\,. \qquad \text{(B.12)}$$

Now define

$$\kappa = \sqrt{\frac{1}{m^2\omega_z^2}\left(2mE - 2mE_b\left(p_x\right) - m^2\omega_x^2 x_t^2\right)}\ , \qquad \text{(B.13)}$$

so that equation B.12 can be rewritten as

$$D_{AV}\left(E\right) = \frac{2}{h^2\omega_z}\int_{p_x}\int_{x_t}\int_{z_t}\frac{dz_t\, dx_t\, dp_x}{\sqrt{\kappa^2 - z_t^2}}\ , \qquad \text{(B.14)}$$

and hence as

$$D_{AV}\left(E\right) = \frac{2}{h^2\omega_z}\int_{p_x}\int_{x_t}\int_{z_t}\frac{dz_t\, dx_t\, dp_x}{\kappa\sqrt{1 - \frac{z_t^2}{\kappa^2}}}\ . \qquad \text{(B.15)}$$

Now consider the limits of the integration with respect to z_t. The maximum and minimum values of z_t are set by conservation of energy, which requires that:

$$E = E_b\left(p_x\right) + \frac{m\omega_x^2 x_t^2}{2} + \frac{m\omega_z^2 z_t^2}{2}\ . \qquad \text{(B.16)}$$

Rearranging equation B.16 for z_t yields

$$z_t = \sqrt{\frac{1}{m^2\omega_z^2}\left(2mE - 2mE_b\left(p_x\right) - m^2\omega_x^2 x_t^2\right)}\ . \qquad \text{(B.17)}$$

Hence, the limits of the integration with respect to z_t are $\pm\kappa$:

$$D_{AV}(E) = \frac{2}{h^2\omega_z}\int_{p_x}\int_{x_t}\int_{-\kappa}^{\kappa}\frac{dz_t\,dx_t\,dp_x}{\kappa\sqrt{1-\frac{z_t^2}{\kappa^2}}}\,. \tag{B.18}$$

The integral with respect to z_t can be performed in terms of a new variable v, defined as

$$\sin v = \frac{z_t}{\kappa}\,. \tag{B.19}$$

It follows that

$$dz_t = \kappa\cos v\,dv. \tag{B.20}$$

Hence, equation B.18 can be rewritten as

$$D_{AV}(E) = \frac{2}{h^2\omega_z}\int_{p_x}\int_{x_t}\int_{-\frac{\pi}{2}}^{\frac{\pi}{2}}\frac{\kappa\cos v\,dv\,dx_t\,dp_x}{\kappa\sqrt{1-\sin^2 v}}\,, \tag{B.21}$$

which simplifies to

$$D_{AV}(E) = \frac{2}{h^2\omega_z}\int_{p_x}\int_{x_t}\int_{-\frac{\pi}{2}}^{\frac{\pi}{2}}dv\,dx_t\,dp_x. \tag{B.22}$$

The integral is now easily evaluated, giving

$$D_{AV}(E) = \frac{2}{h^2\omega_z}\int_{p_x}\int_{x_t}\pi\,dx_t\,dp_x. \tag{B.23}$$

Now consider the integration with respect to x_t. Firstly, the limits of the integration are set by considering conservation of energy, as was done in equation B.16 for the integration with respect to z_t:

$$E = E_b(p_x) + \frac{m\omega_x^2 x_t^2}{2}\,. \tag{B.24}$$

By rearranging equation B.24, the limits of the integration are obtained:

$$x_t = \pm \frac{1}{m\omega_x}\sqrt{2mE - 2mE_b\left(p_x\right)}\,. \tag{B.25}$$

Hence equation B.23 can be rewritten as

$$D_{AV}\left(E\right) = \frac{2\pi}{h^2\omega_z}\int_{p_x}\int_{-\frac{1}{m\omega_x}\sqrt{2mE-2mE_b(p_x)}}^{\frac{1}{m\omega_x}\sqrt{2mE-2mE_b(p_x)}} dx_t\, dp_x. \tag{B.26}$$

The integration with respect to x_t can now be performed:

$$D_{AV}\left(E\right) = \frac{2\pi}{h^2\omega_z}\int_{p_x}\frac{2}{m\omega_x}\sqrt{2mE - 2mE_b\left(p_x\right)}dp_x. \tag{B.27}$$

Rearrangement yields

$$D_{AV}\left(E\right) = \frac{4\pi}{h^2 m\omega_x\omega_z}\int_{p_x}\sqrt{2m}\sqrt{E - E_b\left(p_x\right)}dp_x, \tag{B.28}$$

and hence

$$D_{AV}\left(E\right) = \sqrt{\frac{2}{m}}\frac{1}{\omega_x\omega_z\hbar^2\pi}\int_{p_x}\sqrt{E - E_b\left(p_x\right)}dp_x. \tag{B.29}$$

The limits of the final integral are the boundaries of the first Brillouin zone, i.e. $p_x = \pm\frac{\pi\hbar}{d}$. Equivalently, the integral can be performed over the interval $0 \leq p_x \leq \frac{\pi\hbar}{d}$, and the result doubled:

$$D_{AV}\left(E\right) = \sqrt{\frac{2}{m}}\frac{2}{\omega_x\omega_z\hbar^2\pi}\int_0^{\frac{\pi\hbar}{d}}\sqrt{E - E_b\left(p_x\right)}dp_x. \tag{B.30}$$

Hence equation 4.79 is obtained.

References

[1] H. J. Metcalf and P. van der Straten, *Laser cooling and trapping* (Springer-Verlag, 1999).

[2] E. Peik, M. B. Dahan, I. Bouchoule, Y. Castin, and C. Salomon, Phys. Rev. A. **55**, 2989 (1997).

[3] K. Drese and M. Holthaus, Chemical Physics **217**, 201 (1997).

[4] P. L. Gould, G. A. Ruff, and D. E. Pritchard, Phys. Rev. Lett. **56**, 827 (1986).

[5] M. B. Dahan, E. Peik, J. Reichel, Y. Castin, and C. Salomon, Phys. Rev. Lett. **76**, 4508 (1996).

[6] Q. Niu, X.-G. Zhao, G. Georgakis, and M. Raizen, Phys. Rev. Lett. **76**, 4504 (1996).

[7] S. Wilkinson, C. Bharucha, K. Madison, Q. Niu, and M. Raizen, Phys. Rev. Lett. **76**, 4512 (1996).

[8] E. M. Rasel, M. K. Oberthaler, H. Batelaan, J. Schmiedmayer, and A. Zeilinger, Phys. Rev. Lett. **75**, 2633 (1995).

[9] J. Hook and H. Hall, *Solid state physics* (John Wiley and sons, 1996).

[10] N. W. Ashcroft and N. D. Mermin, *Solid state physics* (W.B. Saunders company, 1976).

[11] C. Pethick and H.Smith, *Bose-Einstein Condensation in dilute gases* (Cambridge University Press, 2002).

[12] G. Woodgate, *Elementary atomic structure* (Oxford university press, 1992).

[13] Y. Gott, M. Ioffe, and V. Tel'kovskii, Nucl. Fusion Suppl. **3**, 1045 (1962).

[14] D. Pritchard, Phys. Rev. Lett. **51**, 1336 (1983).

[15] C. Waschke, H. G. Roskos, R. Schwedler, K. Leo, and H. Kurz, Phys. Rev. Lett. **70**, 3319 (1993).

[16] I. Stewart, *Does God play dice?* (Penguin books, 1990).

[17] E. Ott, *Chaos in dynamical systems* (Cambridge University Press, 1997).

[18] R. C. Hilborn, *Chaos and nonlinear dynamics* (Oxford University Press, 2000).

[19] P. B. Wilkinson, Ph.D. thesis, University of Nottingham (1997).

[20] L. Reichl, *The transition to chaos* (Springer-Verlag, 1992).

[21] H.-J. Stöckmann, *Quantum chaos an introduction* (Cambridge University Press, 1999).

[22] M. C. Gutzwiller, *Chaos in classical and quantum mechanics* (Springer-Verlag, 1990).

[23] E. J. Heller, Phys. Rev. Lett. **53**, 1515 (1984).

[24] P. Bellomo and T. Uzer, Phys. Rev. A. **51**, 1669 (1995).

[25] M. Berry, Journal of Physics A **10**, 2083 (1977).

[26] B. Li, Phys. Rev. E **55**, 5376 (1997).

[27] P. W. O'Conner and E. J. Heller, Phys. Rev. Lett. **61**, 2288 (1988).

[28] E. Bogomolny, Physica D **31**, 169 (1988).

[29] M. Berry, Proceedings of the royal society of London A **423**, 219 (1989).

[30] E. Wigner, Physical review **40**, 749 (1932).

[31] M. Hillery, R. O'Connell, M. Scully, and E. Wigner, Physics Reports **106**, 121 (1984).

[32] M. Berry, Philosophical transactions of the Royal society of London **287**, 237 (1977).

[33] J. Hutchinson and R. Wyatt, Chemical physics letters **72**, 378 (1980).

[34] P. Dando and T. Monteiro, Journal of Physics B. **27**, 2681 (1994).

[35] F. Dalfovo, S. Giorgini, L. P. Pitaevskii, and S. Stringari, Reviews of Modern Physics **71**, 463 (1999).

[36] M. Anderson, J. Ensher, M. Matthews, C. Wieman, and E. Cornell, Science **269**, 198 (1995).

[37] C. Bradley, C. Sackett, J. Tollett, and R. Hulet, Phys. Rev. Lett. **75**, 1687 (1995).

[38] K. Davis, M.-O. Mewes, M. Andrews, N. van Druten, D. Durfee, D. Kurn, and W. Ketterle, Phys. Rev. Lett **75**, 3969 (1995).

[39] S. Bose, Z. Phys. **26**, 178 (1924).

[40] F. London, Physical Review **54**, 947 (1938).

[41] F. Mandl, *Statistical physics* (Wiley, 1988).

[42] O. Morsch, J. Müller, M. Cristiani, D. Ciampini, and E. Arimondo, Phys. Rev. Lett. **87**, 140402 (2001).

[43] L. Landau and E. Lifshitz, *Quantum mechanics* (Pergamon Press, 1977).

[44] K. Burnett, M. Edwards, and C. W. Clark, Physics today p. 37 (1999).

[45] E. P. Gross, Journal of Mathematical Physics **4**, 195 (1963).

[46] T. T. Wu, Journal of Mathematical Physics **2**, 105 (1961).

[47] S. Burger, K. Bongs, S. Dettmers, W. Ertmer, K. Sengstock, A. Sanpera, G. Shlyapnikov, and M. Lewenstein, Phys. Rev. Lett. **83**, 5198 (1999).

[48] J. Denschlag, J. Simsarian, D. Feder, C. W. Clark, L. Collins, J. Cubizolles, L. Deng, E. Hagley, K. Helmerson, W. Reinhardt, et al., Science **287**, 97 (2000).

[49] B. Anderson, P. Halijan, C. Regal, D. Feder, L. Collins, C. Clark, and E. Cornell, Phys. Rev. Lett. **86**, 2926 (2001).

[50] T. Busch and J. Anglin, Phys. Rev. Lett. **84**, 2298 (2000).

[51] Z. Dutton, M. Budde, C. Slowe, and L. V. Hau, Science **293**, 663 (2001).

[52] K. Madison, F. Chevy, W. Wohlleben, and J. Dalibard, Phys. Rev. Lett. **84**, 806 (2000).

[53] J. Abo-Schaeer, C. Raman, J. Vogels, and W. Ketterle, Science **292**, 476 (2001).

[54] T. Fromhold, C. Tench, S. Sujkiewicz, P. Wilkinson, and F. Sheard, Journal of Optics B. **2**, 628 (2000).

[55] R. Scott, S. Sujkiewicz, T. Fromhold, P. Wilkinson, and F. Sheard, Phys. Rev. A. **66**, 023407 (2002).

[56] T. Fromhold, A. Krokhin, C. Tench, S. Bujkiewicz, P. Wilkinson, F. Sheard, and L. Eaves, Phys. Rev. Lett. **87**, 046803 (2001).

[57] A. Rae, *Quantum mechanics* (IOP Publishing Ltd, 1992).

[58] A. Bouchard and M. Luban, Phys. Rev. B. **52**, 5105 (1995).

[59] M. Abramowitz and I. Stegun, *Handbook of mathematical functions* (Dover books, 1965).

[60] W. H. Press, S. A. Teukolsky, W. T. Vetterling, and B. P. Flannery, *Numerical Recipes, the art of scientific computing* (Cambridge University Press, 1994).

[61] B. Ridley, *Quantum processes in semiconductors* (Oxford university press, 1999).

[62] K. E. Strecker, G. B. Partridge, A. G. Truscott, and R. G. Hulet, Nature **417**, 150 (2002).

[63] S. Burger, L. Carr, P. Öhberg, K. Sengstock, and A. Sanpera, Phys. Rev. A. **65**, 043611 (2002).

[64] C. Raman, M. Köhl, D. Durfee, C. Kuklewicz, Z. Hadzibabic, and W. Ketterle, Phys. Rev. Lett. **83**, 2502 (1999).

[65] B. Jackson, J. McCann, and C. Adams, Phys. Rev. A. **61**, 051603 (2000).

[66] B. Anderson and M. Kasevich, Science **282**, 1686 (1998).

[67] D.-I. Choi and Q. Niu, Phys. Rev. Lett. **82**, 2022 (1999).

[68] M. Holthaus, Journal of Optics B **2**, 589 (2000).

[69] S. Burger, F. Cataliotti, C. Fort, F. Minardi, M. Inguscio, M. Chiofalo, and M. Tosi, Phys. Rev. Lett. **86**, 4447 (2001).

[70] M. Chiofalo, S. Succi, and M. Tosi, Phys. Rev. E. **62**, 7438 (2000).

[71] S. Gardiner, D. Jaksch, R. D. abd J.I. Cirac, and P. Zoller, Phys. Rev. A. **62**, 023612 (2000).

Publications

Journal Publications

- *"Creation of solitons and vortices by Bragg reflection of Bose Einstein condensates in an optical lattice"* (cond-matt/0206543), R.G. Scott, A.M. Martin, T.M. Fromhold, S. Bujkiewicz, F.W. Sheard, and M. Leadbeater. Phys. Rev. Lett. **90**, 110404 (2003).
- *"Effects of chaotic energy-band transport on the quantized states of ultra-cold sodium atoms in an optical lattice with a tilted harmonic trap"*, R.G. Scott, S. Bujkiewicz, T.M. Fromhold, P.B. Wilkinson, and F.W. Sheard. Phys. Rev. A. **66**, 023407 (2002).

Conference Publications

- *"Effects of chaotic energy band transport on the quantum properties of cold atoms and condensates in an optical lattice with a tilted harmonic trap."* T.M. Fromhold, R.G. Scott, S. Bujkiewicz, P.B. Wilkinson and F.W. Sheard. Optical Society of America Trends in Optics and Photonics (TOPS), vol. 74, Quantum Electronics and Laser Science Conference, OSA Technical Digest, Postconference Edition, (Optical Society of America, Washington DC, 2002) pp. 89-90.

- *"Creation of solitons and vortices by Bragg reflection of a Bose-Einstein condensate in an optical lattice."* R.G. Scott, S. Bujkiewicz, A.M. Martin, F.W. Sheard, and T.M. Fromhold. Optical Society of America Trends in Optics and Photonics (TOPS), vol. 74, Quantum Electronics and Laser Science Conference, OSA Technical Digest, Postconference Edition, (Optical Society of America, Washington DC, 2002) pp. 155-156.

Conference Presentations

- *"Stochastic carrier dynamics for electron in semiconductor superlattices and ultra-cold atoms in optical lattices"* (Poster presentation) Institute of physics semiconductor microstructures and atom traps conference 2003, London, England.
- *"Effects of chaotic energy-band transport on the quantized states of ultra-cold sodium atoms in an optical lattice with a tilted harmonic trap."* (Poster presentation) Quantum electronics and laser science conference 2002, Long Beach, California, U.S.A.
- *"Creation of solitons and vortices by Bragg reflection of Bose Einstein condensates in an optical lattice."* (Oral presentation) Quantum electronics and laser science conference 2002, Long Beach, California, U.S.A. (Talk delivered by Dr. T.M. Fromhold.)
- *"Creation of solitons and vortices by Bragg reflection of Bose Einstein condensates in an optical lattice."* (Poster presentation) Institute of physics condensed matter and materials physics conference 2002, Brighton, England.